The Dissertation Committee for Siddhant Wahal
certifies that this is the approved version of the following dissertation:

Novel Algorithms for Uncertainty Quantification in Large Scale Systems

Committee:

George Biros, Supervisor

Omar Ghattas

Youssef Marzouk

Robert Moser

Peter Mueller

Novel Algorithms for Uncertainty Quantification in Large Scale Systems

by

Siddhant Wahal

DISSERTATION

Presented to the Faculty of the Graduate School of

The University of Texas at Austin

in Partial Fulfillment

of the Requirements

for the Degree of

DOCTOR OF PHILOSOPHY

THE UNIVERSITY OF TEXAS AT AUSTIN

May 2020

Acknowledgments

This thesis isn't the fruit of individual labor, but the result of collective effort of many hearts and minds.

From my advisor, Prof. George Biros, I learned how to write better papers, give better talks, and how to improve myself as a researcher. I'm grateful for his support. I'm also thankful to my committee members, especially, Prof. Omar Ghattas for leading the Exxon-UT collaboration, and Prof. Marzouk for useful discussions. Prof. Umberto Villa has always been incredibly helpful and approachable, and was an invaluable resource during my early years as a graduate student.

I'm also grateful to Donna Taylor, Melissa Manifold, Lauren Constant, Stephanie Rodriguez, and UT's International Office for helping me jump through all the administrative and bureaucratic hoops.

I'm indebted to my parents and my friends for their unyielding support. This thesis wouldn't be possible without you.

Novel Algorithms for Uncertainty Quantification in Large Scale Systems

Siddhant Wahal, Ph.D.
The University of Texas at Austin, 2020

Supervisor: George Biros

Uncertainty Quantification (UQ) algorithms are of increasing significance in science and engineering. The process of modeling physical reality on computers is rife with uncertainties. These uncertainties get propagated through the computer model, leading to uncertain outputs. As decision-makers from every facet of society come to increasingly rely on computer predictions, the need to characterize this uncertainty has never been greater. However, doing so efficiently remains challenging. This is primarily because computer models are often time consuming to run and because their inputs live in high-dimensional spaces that are difficult to explore. In this thesis, we seek to address this challenge in the context of two UQ problems.

In the first UQ problem, we study rare-event simulation: given a smooth non-linear map with uncertain inputs, what is the probability that the output evaluates inside a specified interval? Standard statistical approaches for computing this probability, such as the Monte Carlo method, become computationally inefficient as the event under consideration becomes rare. To address this inefficiency, we present two Importance Sampling (IS) algorithms.

Our first algorithm, called the Bayesian Inverse Monte Carlo (BIMC) method, relies on solving a fictitious Bayesian inverse problem. The solution of the inverse problem yields a posterior PDF, a local Gaussian approximation to which serves as the importance sampling density. We subject BIMC to rigorous theoretical and experimental analysis, which

establishes that BIMC can lead to speedups of several orders-of-magnitude (over the Monte Carlo method) when the forward map is nearly affine, or weakly non-linear. When these conditions are violated, that is, when the forward map is significantly nonlinear, BIMC leads to a poor-quality IS distribution.

Motivated by these limitations, we propose modifications to BIMC. The modified algorithm, which we term Adaptive-BIMC (A-BIMC), proceeds in two stages. The first stage roughly identifies those regions in input space that trigger a rare event. The second stage then refines the approximation from the first stage of the algorithm. We study A-BIMC's performance on synthetic problems and demonstrate that its performance doesn't depend on how small the target probability is. Rather it depends on the nonlinearity of the input-output map. Through these experiments, we also find that A-BIMC's performance deteriorates with increasing ambient dimensionality of the problem. To address this issue, we lay the foundation for a general dimension reduction strategy for rare-event probability estimation.

The second UQ problem concerns the statistical calibration of model inputs from observed data, with the ultimate aim of issuing uncertainty-equipped predictions of a Quantity-of-Interest (QoI). The physical system that we study here is a hydrocarbon reservoir containing geological faults. Operational decisions concerning the reservoir rely on predictions of financial summaries of the reservoir, such as its Net Present Value. These summaries depend on the nature of fluid flow within the reservoir, which is itself controlled by the extent to which an individual fault inhibits or facilitates flow. This fault property, known as the fault transmissibility, isn't directly measurable and must be calibrated using production data. Here, we design and analyze a complete data-to-prediction workflow to quantify post-calibration uncertainties. We also discuss how these uncertainties change under different reservoir conditions.

Table of Contents

List of Tables

List of Figures

Chapter 1

Introduction

1.1 Motivation

Predictions from computer models of physical reality are used in nearly every facet of society. Capturing physical reality computationally, however, introduces a "cascade of uncertainties" [60] at every stage of the process. For instance, inputs to such computer models, quantities such as initial and boundary conditions, material properties, and coefficients, are rarely known with infinite precision, if at all. Moreover, the mathematical description being used to model reality is usually an imperfect, simplified representation which can fail to capture every detail of the physical process it represents. Finally, discretizing these mathematical models to make them numerically tractable introduces additional errors, further increasing the discrepancy between the model output and reality. As a result, predictions from computer models come tainted with uncertainty. Given the fact that these predictions find applications in areas where either human life, significant monetary investment, or both, are at risk, quantifying the uncertainty in their predictions is critical.

A starting point for this task, known broadly as Uncertainty Quantification (UQ), is to find a tool to mathematically describe uncertainties. In this thesis, we use probabilities to describe uncertainties[1]. This means that each possible realization (or a set of realizations) of an uncertain parameter is assigned a probability that is proportional to the confidence that the true value of the parameter is that value (or within that set). Within this framework, we

[1] Alternative viewpoints of uncertainty include the Dempster-Schafer theory, interval analysis, and worst-case analysis.

study two UQ processes where the uncertainties arise predominantly from the model inputs (ignoring the other sources listed above):

- The first problem concerns rare events. Specifically, let $y = f(\boldsymbol{m})$ be the input-output map, where f is the map, $y \in \mathbb{R}$ is the output, and $\boldsymbol{m} \in \mathbb{R}^d$ is the input. Then, given the probability density function $p(\boldsymbol{m})$ and a set $\mathbb{Y} \subset \mathbb{R}$, we seek to compute $\mu = \mathbb{P}(y \in \mathbb{Y})$. The function f can be thought to represent the map from the uncertain parameters to a decision-relevant Quantity-of-Interest (QoI) y. Here, we focus on the case when this probability is much less than one, or in other words the event $y \in \mathbb{Y}$ is rare.

- In the second problem, we consider the problem of statistically calibrating model inputs from observed data, with the ultimate aim of issuing uncertainty-equipped predictions of QoIs. The physical system that we study here is a hydrocarbon reservoir containing faults. Operational decisions concerning the reservoir rely on predictions of financial summaries of the reservoir, such as its Net Present Value. These summaries depend on the nature of fluid flow within the reservoir, which is itself controlled by the extent to which an individual fault inhibits or facilitates flow. This fault property, known as the its transmissibility, isn't directly measurable and must be calibrated using production data. Here, we not only quantify the post-calibration uncertainties, but also ask how these uncertainties change under different reservoir conditions.

Although seemingly disparate, these UQ problems pose similar algorithmic challenges. The task in both cases relies on exploring conditional probability distributions of the uncertain model inputs. In rare-event simulation, the model inputs are conditioned to the occurrence of the rare-event, that is, they follow the distribution $p(\boldsymbol{m}|f(\boldsymbol{m}) \in \mathbb{Y})$. This distribution is also, in a sense that will be made precise later in the thesis, the optimal distribution for simulating the rare-event. The uncertainties in the fault transmissibilities are conditioned to

the observed production data, $p(\boldsymbol{m}|\boldsymbol{y})$, for observed data $\boldsymbol{y}$. Within the Bayesian framework, this conditional distribution is termed the posterior. These conditional probability distributions are characterized by complicated geometries and reside in high-dimensional spaces, which makes their exploration difficult. The overarching goal of this thesis is to design algorithms and workflows which can overcome these challenges in the context of smooth, finite-dimensional parameter spaces.

1.2 Overview of Methods and Thesis Roadmap

Here, we briefly summarize our algorithms and how they relate to existing approaches in literature. The progression of ideas presented here also acts as a roadmap for this thesis.

1.2.1 Rare-event probability estimation.

Perhaps the simplest way to compute the probability $\mathbb{P}(f(\boldsymbol{m}) \in \mathbb{Y})$, denoted μ, is to use a Monte Carlo method - sample $\boldsymbol{m}$ from $p(\boldsymbol{m})$ and then check whether $f(\boldsymbol{m}) \in \mathbb{Y}$. Such an approach requires an increasing number of evaluations of f as the event $f(\boldsymbol{m}) \in \mathbb{Y}$ becomes rare (or equivalently, μ becomes smaller). Put another way, for a fixed number of evaluations of f, the variance (or error) in the rare-event probability estimate increases as the event becomes rare. In Chapter 2, we begin by proposing a *variance reduction* scheme that is based on Importance Sampling (IS). To construct our importance sampling distribution, we set up an auxiliary, *"fictitious"* Bayesian inverse problem. The solution of the inverse problem yields a posterior PDF, a local Gaussian approximation to which serves as the importance sampling density. We subject this preliminary algorithm, which we call the Bayesian Inverse Monte Carlo (BIMC) method, to a thorough theoretical analysis. This analysis establishes that BIMC leads to an optimal importance sampling distribution when f is affine and p is Gaussian, and also guides the tuning of various algorithmic knobs. Numerical experiments on several real and synthetic test problems reveal that in practical applications, BIMC performs

best when applied to maps f that appear nearly affine at the scale of the covariance of p. We also show that when this is not the case, that is, when f is significantly nonlinear, BIMC leads to a poor-quality IS distribution. This in turn can lead to inaccurate estimates of the rare-event probability.

Motivated by these limitations, we propose modifications to BIMC. The modified algorithm, which we christen Adaptive-BIMC (A-BIMC) and describe in detail in Chapter 3, proceeds in two stages. Stage-1 of A-BIMC solves a sequence of optimization problems in order to adaptively explore the input parameter space where $f(\boldsymbol{m}) \in \mathbb{Y}$ (more precisely, this region is the pre-image of $\mathbb{Y}$, defined as the set $\{\boldsymbol{m} \in \mathbb{R}^d : f(\boldsymbol{m}) \in \mathbb{Y}\}$ and denoted $f^{-1}(\mathbb{Y})$). This stage utilizes bespoke algorithmic components that allow the exploration of $f^{-1}(\mathbb{Y})$ on a global scale, as opposed to a local exploration achieved by BIMC. Then, the local minima obtained by solving the optimization problems are collected into a Gaussian mixture that roughly approximates the conditional distribution $p(\boldsymbol{m}|f(\boldsymbol{m}) \in \mathbb{Y}) \propto \mathbf{1}_{\mathbb{Y}}(f(\boldsymbol{m}))p(\boldsymbol{m})$, which is also the ideal (zero-error) importance sampling density q^* in this case. In Stage-2 of A-BIMC, the Gaussian mixture which crudely approximates q^* is refined using the Mixture Population Monte Carlo Algorithm [18]. The MPMC algorithm modifies the mixture weights, means, and covariances of this Gaussian mixture so that it closely approximates the ideal IS density q^*. This, however, requires further evaluations of f, raising the computational cost of the algorithm. In order to circumvent this problem, we replace evaluations of f in q^* with that of a heuristically constructed surrogate of f. We study A-BIMC's performance on synthetic problems and demonstrate that its performance doesn't depend on how small the target probability is. Rather, it depends on the non-linearity of the input-output map. Through these experiments, we also learn that A-BIMC's performance deteriorates with increasing ambient dimensionality of the problem. To address this issue, we lay the foundation for a general dimension reduction strategy for rare-event probability estimation.

Our work differs significantly from existing approaches in rare-event simulation literature.

Works most relevant to ours are [11, 15, 57, 70, 80], all of which employ a so-called "design-point" which is similar, but not exactly identical, to the MAP point in BIMC. The design point, say $\boldsymbol{m}^*$, is heuristically constrained to lie at the edge of the pre-image $f^{-1}(\mathbb{Y})$. On the other hand, the MAP point lies in the interior of the region $f^{-1}(\mathbb{Y})$; a placement which is provably optimal when f is affine and p is Gaussian. Another common feature of existing algorithms is that they only use pointwise evaluations of the forward model f (or its low-fidelity surrogates) to arrive at the IS distribution. Hence, these methods are "non-intrusive". On the other hand, the manner in which we construct our IS density naturally endows it with information from derivatives of f. To our knowledge, the only other algorithms that utilize derivative information to construct IS densities are IMIS and LIMIS [33, 71]. However, these aren't tailored for rare-event simulation. Directly substituting the zero-variance (zero-error) IS density q^* for the target distribution in these algorithms wouldn't work, since the zero-variance density is non-differentiable, owing to the presence of the characteristic function.

The work in these chapters has been submitted as a two-part paper; preprints can be found at [91, 92].

1.2.2 Inferring fault transmissibilities.

In Chapter 4, we switch gears and address the problem of inferring fault transmissibilities from production data. To do so, we consider synthetic two-dimensional reservoirs containing multiple faults, and prescribe a constant, but unknown, transmissibility to each fault. We assume that production data is available in the form of noisy pressure measurements recorded at the wells at regular time intervals. To model fluid flow within the reservoir, we use a compressible two-phase flow model, coupled with a reduced model for fault behavior.

We are especially interested in quantifying uncertainty in our inferred estimate of the fault transmissibilities. This is so that any operational decisions that rely on the inferred transmissibilities are made with full awareness of the confidence (or lack thereof) in that estimate.

For this reason, we adopt the Bayesian perspective to pose our inference problem. The end result of Bayesian inference is a *posterior* description of uncertainty, expressed as a probability distribution, which is consistent with *prior* knowledge as well as production data, while being cognizant of measurement and/or model errors. If $\boldsymbol{m}$ denotes the unknown fault transmissibilities, $\boldsymbol{y}$ the production data, and $p(\boldsymbol{m})$ the probability distribution that encodes prior knowledge, we're interested in exploring the *conditional* distribution $p(\boldsymbol{m}|\boldsymbol{y})$.

To do so, we combine advances in fault modeling [4,7,56] with state-of-the-art algorithms for Bayesian inference [25,46] to solve the problem of inferring fault transmissibilities from production data. We not only quantify uncertainties in the fault transmissibilities themselves, but also propagate them to decision-relevant quantities-of-interest. Beyond just providing a description of our Bayesian approach, we go further and explore how the Bayesian posterior changes under different scenarios. We do so using two numerical experiments. First, we consider a reservoir with two faults and investigate the effect of varying their relative arrangement on posterior uncertainties. Next, we consider a more realistic situation where the location of only a few major faults is known with certainty. The presence of smaller faults is suspected, but their location and number are unknown. Such a situation can arise, for instance, when seismic data doesn't have enough resolution to capture these smaller faults. We explore whether production data can help pinpoint the location of the smaller faults and the nature of the uncertainties that result.

While faults have been the subject of several UQ studies [30–32,82], all of these studies have used the Ensemble Kalman Filter (EnKF) to estimate uncertainties. A major drawback of these algorithms is that they only keep track of the first two moments of the ensemble, thereby ignoring non-Gaussian effects. As a result, the ensemble uncertainty may not be consistent with the true posterior uncertainty for non-linear problems. In addition, none of the previous studies have investigated how posterior uncertainties in the fault transmissibilities change under different reservoir conditions. Our work is an attempt to fill this gap.

A manuscript based on this chapter is under preparation.

1.3 Contributions

Our contributions to the three CSEM concentration areas are:

Applicable Mathematics (Area A).

- We describe two novel importance sampling algorithms to efficiently simulate rare-events: BIMC, and its sequel A-BIMC. In both algorithms, we leverage derivatives of the forward map f to achieve parsimonious sampling. We subject BIMC to a thorough theoretical investigation revealing conditions necessary for its optimality. BIMC also links forward uncertainty propagation with Bayesian statistical inference, a hitherto unknown connection. With A-BIMC, we extend BIMC to more non-linear maps. A-BIMC uses specially designed algorithmic components (parameter continuation, modified penalty algorithm) that allow it to explore the pre-image of the target interval on a global scale. In addition, we also lay the foundation for a general dimension reduction strategy for rare-event probability estimation.

- For inferring fault transmissibilities, we formulate a mixed method coupled to a discontinuous Galerkin scheme to discretize the two-phase compressible flow equations. We've also derived adjoints of resulting discretized system of equations.

Numerical Analysis and Scientific Computation (Area B)

- We've implemented BIMC and A-BIMC as standalone classes in `MATLAB`. In addition, BIMC has been incorporated within `hIPPYlib` [89,90], a python based inverse problems library. The class interface is extensible – the user just needs to define a QoI and

its derivatives with respect to the parameter in order to use it. In addition, we've attempted to keep the tunable "knobs" in our algorithm to a minimum so that it remains easy to use.

- The forward and adjoint solvers for our two-phase compressible flow discretization are written in `python`, and use `FEniCS` to assemble the finite element weak forms, and `PETSc` for efficient linear and non-linear solvers. The discrete adjoints conform to the `hIPPYlib` Application Programming Interface (API) and are not specific to the two-phase flow problem considered here. Instead, they generalize to arbitrary non-linear time-dependent PDEs, thereby extending `hIPPYlib`'s capabilities to time-dependent problems[2].

Mathematical Modeling and Applications (Area C)

- We've applied BIMC to compute rare-event probabilities in several application areas, including heat conduction and combustion.

- We've designed a complete data-to-prediction workflow for inferring fault transmissibilities from production data and then issuing predictions of decision-relevant QoIs. The QoIs we work with are designed to mimic realistic decision-making scenarios, such as whether or not drilling an additional well is a feasible investment. Using this data-to-prediction workflow, we comment on the nature of posterior uncertainties under different reservoir conditions.

[2]Inverse problems with time-dependent forward PDEs have been implemented using `hIPPYlib`. However, these implementations were problem specific - they exploited specific problem features such as linearity or the structure of the observation operators. A general framework for non-linear time-dependent PDEs was missing in `hIPPYlib`

1.4 Limitations and Future Work

Our work has the following limitations:

- In rare-events, the performance of the A-BIMC algorithm deteriorates with increasing ambient dimensionality of the problem. Noting that for most natural problems, the ideal importance sampling distribution is expected to differ from the nominal distribution only over a small subspace of the parameter space, we outline a general dimension reduction strategy in Chapter 3. However, designing algorithms to discover the subspace in question still remains an open research challenge. In the future, we aim to apply techniques developed for dimension reduction in Bayesian inverse problems [24, 96] to discover this subspace and reduce the dimension of the rare-event probability estimation problem.

- A major limitation of our work on inferring fault transmissibilities is that it's two-dimensional. In the future, we aim to extend this study using three-dimensional models. This will necessitate the use of more efficient linear and non-linear solvers in order to execute a forward solve in reasonable time. We were also unable to efficiently explore the posterior distribution using the Markov Chain Monte Carlo algorithm (MCMC) for the unknown fault location experiment in Chapter 4. In our future work, we wish to address this shortcoming. A major challenge here will be designing an MCMC algorithm that can navigate the rapidly changing local relationships in the posterior. Recent work on MCMC algorithms that leverage gradients [43] and non-linear transport maps [64] provides a promising avenue to overcome this challenge.

1.5 Organization of the Thesis

We devote Chapters 2 and 3 to describe our algorithms for rare-event probability estimation. In Chapter 2, we review the necessary theoretical background and literature before describ-

ing the BIMC method in detail. In Chapter 3, we extend BIMC into an adaptive procedure called A-BIMC, and also lay the foundation for dimension reduction in rare-event probability estimation. In Chapter 4, we switch gears and address the problem of inferring fault transmissibilities from production data. We start Chapter 4 with brief reviews of literature and mathematical models for simulating flows in faulted porous media, before describing our methodology and results. We summarize our conclusions and identify avenues for future research in Chapter 5. The necessary notation is introduced individually in each chapter.

Chapter 2

The Bayesian Inverse Monte Carlo Method

In this chapter, we state the rare-event probability estimation problem and review prevalent approaches to estimate these probabilities efficiently. We demonstrate that traditional sampling algorithms, such as the Monte Carlo method, may require infeasible running times to accurately evaluate these probabilities. To address this drawback, we devise an importance sampling scheme (which we call BIMC: Bayesian Inverse Monte Carlo method) that relies on solving an auxiliary, fictitious Bayesian inverse problem. The solution of the inverse problem yields a posterior PDF, a local Gaussian approximation to which serves as the importance sampling density. We apply BIMC to several problems and demonstrate that it can lead to computational savings of several orders of magnitude over the Monte Carlo method. We also delineate conditions under which BIMC is optimal, as well as conditions when it can fail to yield an effective IS density.

2.1 Introduction

We're interesting in the following rare-event probability estimation problem. Let $f(\boldsymbol{m}) : \mathbb{R}^d \to \mathbb{R}$ be a *smooth nonlinear operator*, and $p(\boldsymbol{m})$ a probability density function (PDF) for $\boldsymbol{m}$. Given a *target interval* $\mathbb{Y} \subset \mathbb{R}$, what is the probability $\mu = \mathbb{P}(f(\boldsymbol{m}) \in \mathbb{Y})$? Equivalently, μ is the expectation under $p(\boldsymbol{m})$ of the *indicator function* $\mathbf{1}_{\mathbb{Y}}(f(\boldsymbol{m}))$. [1] We focus on the case when $\mu \ll 1$, *i.e.,* the event $f(\boldsymbol{m}) \in \mathbb{Y}$ is rare.

[1] The indicator function, $\mathbf{1}_{\mathbb{Y}}(y)$ assumes the value 1 if $y \in \mathbb{Y}$, and 0 otherwise.

In our context, $f(\boldsymbol{m})$ is a map from some random finite dimensional parameter space to a quantity-of-interest (QoI). Such parameter-to-QoI maps are often a composition of the solution of a differential equation for a state variable, and an operator that extracts the QoI from the state. The parameters $\boldsymbol{m}$ represent uncertain parameters in the physical model. This uncertainty can arise from a variety of sources, such as lack of knowledge, measurement errors, or noise. Here, we assume that the uncertainty is described by a known PDF, $p(\boldsymbol{m})$. A *Monte Carlo* (MC) method can be used to compute μ by sampling $\boldsymbol{m}$ from $p(\boldsymbol{m})$ and then checking whether $f(\boldsymbol{m}) \in \mathbb{Y}$. But such an approach can be prohibitively expensive if the operator f is expensive to evaluate, especially when $\mu \ll 1$.

Summary of the methodology We propose a variance reduction scheme based on importance sampling (IS). In IS, samples are drawn from a new distribution, say $q(\boldsymbol{m})$, in order to increase the occurrences of the rare event. We construct our IS density as follows. We begin by setting up an auxiliary *inverse problem*. First we select a $y \in \mathbb{Y}$, and then we find $\boldsymbol{m}$ such that $f(\boldsymbol{m}) \approx y$. This is an ill-posed or inverse problem since given a scalar y we want to reconstruct the vector $\boldsymbol{m}$. A simple counting argument shows that this is impossible unless we use some kind of regularization. To address this ill-posedness we adopt a Bayesian perspective, that is, the solution of the inverse problem is not a specific point estimate $\boldsymbol{m}$ but a "posterior distribution", $p(\boldsymbol{m}|y)$, a PDF on the parameters $\boldsymbol{m}$ conditioned on y. We will use a Gaussian approximation of this posterior around the *Maximum A Posteriori* (MAP) point as the importance sampling distribution. The mean of the approximating Gaussian is the MAP point itself, and its covariance is the inverse of the Gauss-Newton Hessian, $\mathbf{H}_{\mathrm{GN}}^{-1}$, of $-\log(p(\boldsymbol{m}|y))$ at the MAP point.

Contributions In summary, our contributions are the following.

- We introduce the concept of solving *inverse* problems for *forward* uncertainty quantification.
- To our knowledge, this is the first algorithm that exploits derivatives of the forward operator f to arrive at an IS density for simulating rare events.
- We offer a thorough theoretical analysis of the affine-Gaussian inverse problem. This analysis establishes conditions for optimality of our algorithm, as well as guides the tuning of various algorithmic "knobs".
- We apply our methodology to several real and synthetic problems and demonstrate orders-of-magnitude speedup over a vanilla MC implementation.

Limitations

- The success of our algorithms depends strongly upon the quality (both in terms of accuracy and speed) of the inverse problem solution. When the operator f involves differential equations, efficiently solving the inverse problem requires adjoint operators and perhaps sophisticated PDE-constrained optimization solvers and preconditioners.
- Our methodology has several failure mechanisms. These are described in detail in Section 2.4. In light of these failure mechanisms, the question of *a priori* assessing the applicability of BIMC to a given problem (*i.e.*, a given combination of $f(\boldsymbol{m})$, $p(\boldsymbol{m})$, and $\mathbb{Y}$) has also been left unexplored.

Related work The literature on goal-oriented techniques, importance sampling, rare-event probability estimation, and Bayesian inference is quite extensive. Here, we review work that is most relevant.

Goal-oriented methods BIMC can be viewed as a goal-oriented technique for forward UQ. The idea of goal-oriented techniques isn't new (see [52, 53, 85]). However, most of these works focus on dimensionality reduction, and not rare events. Also pertinent is the measure-theoretic approach to inverse problems [14, 17].

Rare-event probability estimation A large body of work on rare events has been motivated by the problem of assessing the reliability of systems. In such problems, the task is to compute the probability of failure of a system, which occurs when $f(\boldsymbol{m}) < 0$ (or in our framework, when $\mathbb{Y} = (-\infty, 0)$).

Analytical approaches to approximate this failure probability include the First and Second Order Reliability Methods (see [70] for a review). These methods are based on approximating f with a truncated Taylor series expansion around a "design" point. A drawback of these methods is that they have no means of estimating the error in the computed failure probability. We would like to note that the concept of "design" points here is similar to the MAP point in our algorithm, but they are not exactly identical. The design point, say $\boldsymbol{m}^*$, is always constrained to satisfy $f(\boldsymbol{m}^*) = 0$. That is, it lies at the edge of the pre-image $f^{-1}(\mathbb{Y})$. The MAP point, on the other hand, is expected to lie in the interior of the region $f^{-1}(\mathbb{Y})$. Moreover, the fact that $\boldsymbol{m}_{\text{MAP}}$ lies in the interior of $f^{-1}(\mathbb{Y})$ is accounted for, and in fact, exploited, when we choose tunable parameters of our algorithm.

Statistical approaches to evaluate the failure probability have received considerable attention (see [77] for a review). As opposed to analytical methods, these methods have well-understood convergence properties, and they come with a natural error estimate. In this context, a simple Monte Carlo method is usually inefficient, and some form of variance reduction is usually required. Several importance sampling methods have been proposed to this effect. We refer the reader to [63] for a general introduction to importance sampling. Several IS algorithms ([11, 15, 57, 80]) reuse the concept of design points by placing normal

distributions centered there. In [15, 80], the covariance of the IS distribution is either set equal to that of $p(\boldsymbol{m})$, or evaluated heuristically, for example, from samples. In our method, approximating the posterior via a Gaussian yields a natural covariance for the IS density.

Within reliability analysis, another class of algorithms uses surrogate models to reduce the computational effort required to build an IS density [49, 65, 66]. A different approach involves simulating a sequence of relatively higher frequency events to arrive at the rare event probability. This idea is used in the Cross Entropy algorithm [27] to arrive at an optimal IS distribution within a parametric family. It has also been coupled with Markov Chain Monte Carlo methods for high-dimensional reliability problems [9, 10, 48].

A common feature of all these algorithms is that they only use pointwise evaluations of the forward model f (or its low-fidelity surrogates) to arrive at the IS distribution. Hence, these methods are "non-intrusive". On the other hand, the manner in which we construct our IS density naturally endows it with information from derivatives of f. To our knowledge, the only other algorithms that utilize derivative information to construct IS densities are IMIS and LIMIS [33, 71]. However, these aren't tailored for rare-event simulation. Directly substituting the zero-variance (zero-error) IS density (see Section 2.2.2) for the target distribution in these algorithms wouldn't work, since the zero-variance density is non-differentiable, owing to the presence of the characteristic function.

PDE-constrained optimization and Bayesian inverse problems In BIMC, we rely on adjoints to compute gradients and Hessians of $-\log p(\boldsymbol{m}|y)$. We refer to [41] for an introduction to the method of adjoints. Computing the MAP point is a PDE-constrained optimization problem which can require sophisticated algorithms [5]. Scalable algorithms for characterizing the Hessian of $-\log(p(\boldsymbol{m}|y))$ are described in [46]. Because we construct our IS density through the solution of an inverse problem, our approach can be easily built on top of existing scalable frameworks for solving Bayesian inverse problems, such as [89, 90].

Organization of the Chapter The rest of this chapter is organized as follows – Table 2.1 introduces the notation adopted in this chapter. Section 2.2 provides introductions to the Monte Carlo method, importance sampling, as well as Bayesian inference. In Section 2.3, we describe our algorithm, including analysis that governs the choice of tunable parameters that arise in the algorithm. Section 2.4 contains numerical experiments and their results, as well as a description of the failure mechanisms of our method. Finally, we summarize our conclusions in Section 2.5. A description how the various forward models used in our numerical experiments were implemented is provided in Appendix A.

Symbol	Meaning
f	The input-output, or the forward, map
$\boldsymbol{m}$	Vector of input parameters to f
$p(\boldsymbol{m})$	Input probability density for $\boldsymbol{m}$
$\mathbb{Y}$	Target interval for $f(\boldsymbol{m})$
$\mathbb{P}(f(\boldsymbol{m}) \in \mathbb{Y})$	Probability of the event $f(\boldsymbol{m}) \in \mathbb{Y}$
μ	$\mathbb{P}\left(f(\boldsymbol{m}) \in \mathbb{Y}\right)$
$\mathcal{N}\left(\boldsymbol{m}_0, \boldsymbol{\Sigma}_0\right)$	Normal distribution with mean $\boldsymbol{m}_0$ and covariance $\boldsymbol{\Sigma}_0$
N	Number of Monte Carlo (MC) or Importance Sampling (IS) samples
$\hat{\mu}^N$	MC estimate for μ computed using N samples
$\tilde{\mu}^N$	IS estimate for μ computed using N samples
$\hat{e}_{\text{RMS}}$	Root Mean Square (RMS) error in $\hat{\mu}^N$
$\tilde{e}_{\text{RMS}}$	RMS error in $\tilde{\mu}^N$
$p(y\|\boldsymbol{m})$	The likelihood density
$p(\boldsymbol{m}\|y)$	The posterior density
$\boldsymbol{m}_{\text{MAP}}$	The Maximum *A Posteriori* (MAP) point of $p(\boldsymbol{m}\|y)$
$\mathbf{H}_{\text{GN}}$	The Gauss-Newton Hessian of $-\log p(\boldsymbol{m}\|y)$
$D_{\text{KL}}(p\|\|q)$	The Kullback-Leibler divergence between densities p and q

Table 2.1: *Summary of key notation used in this chapter.*

2.2 Background

2.2.1 The Monte Carlo Method

One way to compute the rare-event probability, μ, is using the Monte Carlo method. The forward operator is applied on N independent, identically distributed (i.i.d.) samples from $p(\boldsymbol{m})$, $\{\boldsymbol{m}_i\}_{i=1}^N$. Then, an unbiased estimate of μ is:

$$\hat{\mu}^N = \frac{\sum_{i=1}^N \mathbf{1}_{\mathbb{Y}}(f(\boldsymbol{m}_i))}{N}. \tag{2.1}$$

The law of large numbers guarantees that in the limit $N \to \infty$, $\hat{\mu}$ converges to μ [74]. The relative Root Mean Square Error (RMSE) in $\hat{\mu}$ is:

$$\hat{e}_{\text{RMS}} = \frac{1}{\mu}\sqrt{\mathbb{E}_p\Big((\hat{\mu}^N - \mu)^2\Big)} = \frac{1}{\mu}\sqrt{\frac{\mathbb{V}_p\Big(\mathbf{1}_{\mathbb{Y}}(f(\boldsymbol{m}))\Big)}{N}} = \sqrt{\frac{\sigma_p^2}{\mu^2 N}}. \tag{2.2}$$

Since $\mathbf{1}_{\mathbb{Y}}(f(\boldsymbol{m}))$ is a binary random variable, its variance is $\sigma_p^2 = \mu(1-\mu)$. This implies that the relative RMSE is approximately $\sqrt{1/\mu N}$ when $\mu \ll 1$. In order to achieve a specified relative accuracy threshold, the number of samples must then scale as $N \sim 1/\mu$. This is problematic since it can render evaluating extremely rare probabilities virtually impossible if $f(\boldsymbol{m})$ is expensive to evaluate. The evaluation of rare probabilities can be made tractable by reducing the variance of the MC estimate. In BIMC, we aim to achieve variance reduction through importance sampling, which is briefly introduced in the next section.

2.2.2 Importance Sampling

Importance sampling biases samples towards regions which trigger the rare event (or in our context, where $f(\boldsymbol{m}) \in \mathbb{Y}$) with the help of a new probability density q. The contribution

from each sample, however, must be weighed to account for the fact that one is no longer sampling from the original distribution p. Thus,

$$\mu = \int_{\mathbb{R}^d} \mathbf{1}_{\mathbb{Y}}\left(f(\boldsymbol{m})\right) p(\boldsymbol{m}) \mathrm{d}\boldsymbol{m} = \int_{\mathbb{R}^d} \mathbf{1}_{\mathbb{Y}}\left(f(\boldsymbol{m})\right) \frac{p(\boldsymbol{m})}{q(\boldsymbol{m})} q(\boldsymbol{m}) \mathrm{d}\boldsymbol{m} = \mathbb{E}_q\left(\mathbf{1}_{\mathbb{Y}}\left(f(\boldsymbol{m})\right) \frac{p(\boldsymbol{m})}{q(\boldsymbol{m})}\right). \tag{2.3}$$

Then, q is called the importance distribution and $p(\boldsymbol{m})/q(\boldsymbol{m})$ is the likelihood ratio. The importance sampling estimate for μ is:

$$\tilde{\mu}^N = \frac{1}{N} \sum_{i=1}^{N} \frac{\mathbf{1}_{\mathbb{Y}}\big(f(\boldsymbol{m}_i)\big) p(\boldsymbol{m}_i)}{q(\boldsymbol{m}_i)}, \quad \boldsymbol{m}_i \sim q(\boldsymbol{m}). \tag{2.4}$$

The relative RMSE in estimating μ using importance sampling is:

$$\begin{aligned} \tilde{e}_{\mathrm{RMS}} &= \frac{1}{\mu} \sqrt{\mathbb{E}_q\big((\tilde{\mu}^N - \mu)^2\big)} = \sqrt{\frac{\sigma_q^2}{\mu^2 N}}, \text{ where,} \\ \sigma_q^2 &= \mathbb{V}_q\left(\mathbf{1}_{\mathbb{Y}}\big(f(\boldsymbol{m})\big) \frac{p(\boldsymbol{m})}{q(\boldsymbol{m})}\right). \end{aligned} \tag{2.5}$$

If σ_q^2 is smaller than σ_p^2, the importance sampling estimate of μ is more accurate than the one obtained using simple MC. The main challenge in importance sampling is selecting an importance density q such that $\sigma_q < \sigma_p$. The IS density that minimizes σ_q is known to be $q^* = \mathbf{1}_{\mathbb{Y}}(f(\boldsymbol{m}))p(\boldsymbol{m})/\mu$ (see [47]). That is, the optimal density for importance sampling is just $p(\boldsymbol{m})$ truncated over regions where $f(\boldsymbol{m}) \in \mathbb{Y}$, and then appropriately renormalized. Another interpretation of q^* is that it's the conditional distribution of the parameter m given that they evaulate inside $\mathbb{Y}$. Hence, q^* is equivalent to $p(\boldsymbol{m}|f(\boldsymbol{m}) \in \mathbb{Y})$. However, q^* cannot be sampled from, since the renormalization constant μ is exactly the probability we

set out to compute in the first place. Nevertheless, it defines characteristics desirable of a good importance density – it must have most of its mass concentrated over regions where $f(\boldsymbol{m}) \in \mathbb{Y}$ and resemble $p(\boldsymbol{m})$ in those regions.

So the first step in constructing an effective IS density is identifying regions where $f(\boldsymbol{m}) \in \mathbb{Y}$. As mentioned in Section 2.1, this is done by solving a Bayesian inverse problem. Before describing the BIMC methodology in detail, we first provide a brief introduction to Bayesian inference in a generalized setting.

2.2.3 Bayesian inference

In a general setting where inference must be performed, the problem is slightly different. Here the goal is to infer input parameters $\boldsymbol{m}$ from a (possibly noisy) real-world observation of the output, say y. In the Bayesian approach, this problem is solved in the statistical sense. The solution of a Bayesian inference problem is a probability density over the space of parameters that takes into account any prior knowledge about the parameters as well as uncertainties in measurement and/or modeling. This probability density, known as the posterior, expresses how likely it is for a particular estimate to be the true parameter corresponding to the observation.

In addition to the observation y, assume the following quantities have been specified – *i)* a suitable probability density $p(\boldsymbol{m})$ that captures prior knowledge about the parameters $\boldsymbol{m}$, and *ii)* the conditional probability density of observing the data y given the parameters $\boldsymbol{m}$, $p(y|\boldsymbol{m})$. Then, from Bayes' theorem, the posterior is given by:

$$p(\boldsymbol{m}|y) \propto p(y|\boldsymbol{m})p(\boldsymbol{m}). \tag{2.6}$$

The posterior can also be interpreted to be updated beliefs once the data and errors have been assimilated. We would like to emphasize here that in an actual inverse problem, the

observation y, as well as the likelihood density $p(y|\boldsymbol{m})$ are physically meaningful. The former corresponds to real-world measurements of the output of the forward model. The latter describes a model for errors arising out due to modeling inadequacy or measurement.

The posterior by itself is of little use. Often, the task is to evaluate integrals involving the posterior. This might be the case, for example, when trying to characterize uncertainty in the inferred parameters by evaluating moments (mean, covariance) of the posterior. Analytical evaluation of these integrals is often out of the question and a sample based estimate must be used. Except in certain cases, the posterior is an arbitrary PDF in $\mathbb{R}^d$ and generating samples from it requires sophisticated methods such as Markov Chain Monte Carlo. For easy sample generation, the posterior can be locally approximated by a Gaussian around its mode (also known as the Maximum *A Posteriori* point). By linearizing f around the MAP point, it can be shown that the mean of the approximating Gaussian is the MAP point, and its covariance is the inverse of the Gauss-Newton Hessian matrix of $-\log p(\boldsymbol{m}|y)$ at the MAP point [46].

As a concrete example, consider the case when the likelihood density represents Gaussian additive error of magnitude σ, $p(y|\boldsymbol{m}) = \mathcal{N}(f(\boldsymbol{m}), \sigma^2)$. Then, $p(\boldsymbol{m}|y) \propto \exp\left(-\frac{(y-f(\boldsymbol{m}))^2}{2\sigma^2}\right) p(\boldsymbol{m})$, and we have (up to an additive constant),

$$-\log p(\boldsymbol{m}|y) = \frac{1}{2\sigma^2}\left(y - f(\boldsymbol{m})\right)^2 - \log p(\boldsymbol{m}), \tag{2.7}$$

and, $\boldsymbol{m}_{\text{MAP}}$ can be found as:

$$\boldsymbol{m}_{\text{MAP}} = \underset{\boldsymbol{m}\in\mathbb{R}^d}{\arg\min} \frac{1}{2\sigma^2}\left(y - f(\boldsymbol{m})\right)^2 - \log p(\boldsymbol{m}). \tag{2.8}$$

Then, the Gauss-Newton Hessian matrix of $-\log(p(\boldsymbol{m}|y))$ can be written as

$$\begin{aligned}\mathbf{H}_{\mathrm{GN}} &= -\nabla^2_{\boldsymbol{m}} \log p(\boldsymbol{m}|y) \\ &= \frac{1}{\sigma^2}(\nabla_{\boldsymbol{m}} f)(\nabla_{\boldsymbol{m}} f)^T - \nabla^2_{\boldsymbol{m}} \log p(\boldsymbol{m}).\end{aligned} \tag{2.9}$$

Note that, the Gauss-Newton Hessian has the attractive property of being positive-definite. These expressions show that $\boldsymbol{m}_{\mathrm{MAP}}$ can be interpreted as that point in parameter space that minimizes mismatch with the observation but is also highly likely under the prior. So sampling from a Gaussian approximation of the posterior can be thought of as drawing samples in the vicinity of a point that is consistent with the data as well as the prior. In addition, the covariance or spread of the samples is informed by the derivatives of the forward model. While constructing the IS density in BIMC, this feature of the Gaussian approximation of the posterior in a general, real-world setting will be used in conjunction with the knowledge of the shape of the ideal IS density. This completes the presentation of the necessary theoretical background and we are ready to describe the BIMC methodology.

2.3 Methodology

Recall that the forward UQ problem is to compute $\mathbb{P}\left(f(\boldsymbol{m}) \in \mathbb{Y}\right)$ when $\boldsymbol{m} \sim p(\boldsymbol{m})$. In BIMC, we use the ingredients of the forward UQ problem to construct a *fictitious* Bayesian inverse problem as follows. We

1. select some $y \in \mathbb{Y}$ as a surrogate for real-world observation,
2. use $p(\boldsymbol{m})$ as the prior, and,
3. concoct a likelihood density $p(\boldsymbol{m}|y)$.

This enables us to define a pseudo-posterior $p(\boldsymbol{m}|y)$, and subsequently, a Gaussian approximation to it. We call this inverse problem fictitious because both the observation y and the

likelihood density $p(\boldsymbol{m}|y)$ are arbitrarily chosen by us. Neither is y a real-world measurement of a physical quantity, nor does $p(\boldsymbol{m}|y)$ correspond to an actual error model. From here on, we will refer to these artificial quantities as the pseudo-data and the pseudo-likelihood respectively.

We propose using the Gaussian approximation to the posterior as an IS density. As outlined in the previous section, in the real-world setting, the mean of the Gaussian approximation of the posterior (the MAP point) is that point in parameter space that is consistent with the data as well as the prior. So by solving the fictitious Bayesian inverse problem defined earlier, we expect the mean of the IS density to be a point that is consistent with some $y \in \mathbb{Y}$ as well as the nominal PDF $p(\boldsymbol{m})$. This ensures the IS density is centered around regions where $f(\boldsymbol{m}) \in \mathbb{Y}$. Further, the covariance matrix of the Gaussian approximation, and hence the IS density, contains first-order derivative information. This approach is illustrated in Figure 2.1.

Since a Gaussian likelihood model has been assumed, the pseudo-posterior is proportional to $\exp\left(-(y - f(\boldsymbol{m}))^2/2\sigma^2\right) p(\boldsymbol{m})$. Thus, an alternative interpretation of the pseudo-posterior in this case is as a "mollified" approximation of the ideal IS density, $\mathbf{1}_{\mathbb{Y}}\left(f(\boldsymbol{m})\right) p(\boldsymbol{m})$, where the mollification has been achieved by smudging the sharply defined characteristic function $\mathbf{1}_{\mathbb{Y}}(f(\boldsymbol{m}))$ into a Gaussian, $\exp\left(-(y - f(\boldsymbol{m}))^2/2\sigma^2\right)$ The advantage of doing this lies in the fact that the mollified ideal IS density has well-defined derivatives and can be explored via derivative-aware methods, unlike the true ideal IS density, which isn't differentiable. Algorithms like IMIS [71], and LIMIS [33] can now be employed for rare-event probability estimation by plugging in the pseudo-posterior as the target.

Irrespective of the interpretation, this methodology introduces two tunable parameters—the pseudo-data $y \in \mathbb{Y}$ and variance of the pseudo-likelihood density, σ^2. These parameters can have a profound effect on the accuracy of the importance sampler and must be tuned with care. The tuning strategy depends on the nature of $f(\boldsymbol{m})$ as well as $p(\boldsymbol{m})$. Next, we discuss

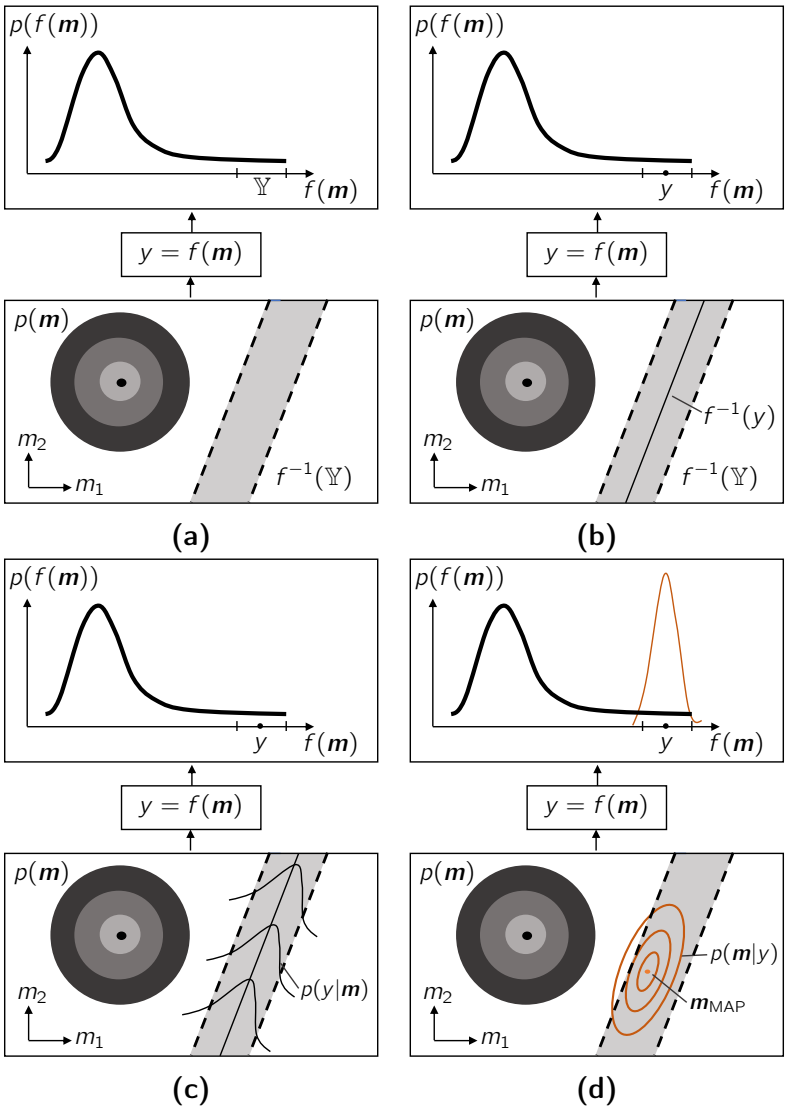

Figure 2.1: *Summary of the BIMC methodology. In (a), the problem statement is summarized – we need to compute the measure of the pre-image of the target interval, $f^{-1}(\mathbb{Y})$. In (b), we introduce the pseudo-data point $y \in \mathbb{Y}$ and redefine $p(\boldsymbol{m})$ to be the pseudo-prior in a fictitious Bayesian inverse problem. The true inverse of the pseudo-data point y is a straight line in $\mathbb{R}^2$. Next, in (c), we select a pseudo-likelihood density, $p(y|\boldsymbol{m})$. The pseudo-likelihood density can also be viewed as a mollified approximation of the characteristic function. Part (d) shows the contours of the posterior, $p(\boldsymbol{m}|y)$, which is proportional to $p(y|\boldsymbol{m})p(\boldsymbol{m})$. We use a Gaussian approximation to this posterior as an IS density.*

possible cases as well as the corresponding tuning strategy.

2.3.1 Affine f, Gaussian p

Although for a affine $f(\boldsymbol{m})$ and Gaussian $p(\boldsymbol{m})$, the probability $\mu = \mathbb{P}(f(\boldsymbol{m}) \in \mathbb{Y})$ may be analytically computed, the availability of analytical expressions for $\boldsymbol{m}_{\text{MAP}}$ and $\mathbf{H}_{\text{GN}}$ in this case illustrates how our importance sampler achieves variance reduction. Let $f(\boldsymbol{m}) = \boldsymbol{v}^\top \boldsymbol{m} + \beta$, $p(\boldsymbol{m}) = \mathcal{N}(\boldsymbol{m}_0, \boldsymbol{\Sigma}_0)$ for some $\boldsymbol{v}$, $\boldsymbol{m}_0 \in \mathbb{R}^d$, $\beta \in \mathbb{R}$ and $\boldsymbol{\Sigma}_0 \in \mathbb{R}^{d\times d}$. Then, μ is given analytically as

$$\mu = \Phi\left(\frac{y_{\max} - \nu}{\gamma}\right) - \Phi\left(\frac{y_{\min} - \nu}{\gamma}\right), \tag{2.10}$$

where $\nu = \boldsymbol{v}^\top \boldsymbol{m}_0 + \beta$, $\gamma^2 = \boldsymbol{v}^\top \boldsymbol{\Sigma}_0 \boldsymbol{v}$, and Φ is the standard Normal CDF.

Now, suppose the pseudo-data is some $y \in \mathbb{Y}$ and the variance of the pseudo-likelihood is some $\sigma^2 \in \mathbb{R}$. Then the pseudo-posterior $p(\boldsymbol{m}|y)$ is also a Gaussian and no approximations are necessary. Hence, the IS density is given by $q(\boldsymbol{m}) = \mathcal{N}(\boldsymbol{m}_{\text{MAP}}, \mathbf{H}_{\text{GN}}^{-1})$, where,

$$\boldsymbol{m}_{\text{MAP}} = \boldsymbol{m}_0 + \frac{y - f(\boldsymbol{m}_0)}{\sigma^2 + \boldsymbol{v}^\top \boldsymbol{\Sigma}_0 \boldsymbol{v}} \boldsymbol{\Sigma}_0 \boldsymbol{v}, \quad \mathbf{H}_{\text{GN}}^{-1} = \boldsymbol{\Sigma}_0 - \frac{1}{\sigma^2 + \boldsymbol{v}^\top \boldsymbol{\Sigma}_0 \boldsymbol{v}} \big(\boldsymbol{\Sigma}_0 \boldsymbol{v}\big)\big(\boldsymbol{\Sigma}_0 \boldsymbol{v}\big)^T. \tag{2.11}$$

The expressions for $\boldsymbol{m}_{\text{MAP}}$ and $\mathbf{H}_{\text{GN}}^{-1}$ expose how our importance sampler achieves variance reduction. The MAP point identifies the region in parameter space where $f(\boldsymbol{m}) \approx y$. The spread of the importance sampler, as encapsulated in its covariance, is reduced over its nominal value $\boldsymbol{\Sigma}_0$ in a direction informed by $\boldsymbol{v}$, the gradient of $f(\boldsymbol{m})$. Note that the reduction in variance occurs in just one direction, $\boldsymbol{\Sigma}_0 \boldsymbol{v}$; the variance of $p(\boldsymbol{m})$ is retained in all other directions. The parameter σ^2 controls how much $q(\boldsymbol{m})$ is updated over $p(\boldsymbol{m})$- a small value for σ results in a larger shift from $\boldsymbol{m}_0$ and a larger reduction in its spread. These claims become

more transparent by noticing that the pushforward of $q(\boldsymbol{m})$ under f is another Gaussian distribution in $\mathbb{R}$ (the pushforward density represents how $f(\boldsymbol{m})$ will be distributed if $\boldsymbol{m}$ is distributed according to $q(\boldsymbol{m})$). The mean χ and variance ξ^2 of this pushforward density are-

$$\chi = (1-\rho^2)y + \rho^2 f(\boldsymbol{m}_0),\ \xi^2 = \rho^2 \boldsymbol{v}^\top \boldsymbol{\Sigma}_0 \boldsymbol{v},\ \text{where},\rho^2 = \frac{\sigma^2}{\sigma^2 + \boldsymbol{v}^\top \boldsymbol{\Sigma}_0 \boldsymbol{v}} < 1. \tag{2.12}$$

A small σ implies small ρ, which means χ is closer y and ξ^2 is small.

Since our goal is importance sampling, we wish to select those values for the tunable parameters that deliver just the right amount of update over p. We do this by minimizing the Kullback-Leibler (KL) divergence between $q(\boldsymbol{m})$ and the ideal IS distribution $q^*(\boldsymbol{m})$. Although not a true metric, the KL divergence between two probability densities is a measure of the distance between them. It is defined as:

$$D_{\mathrm{KL}}(p||q) = \int p(\boldsymbol{m}) \log \frac{p(\boldsymbol{m})}{q(\boldsymbol{m})} \mathrm{d}\boldsymbol{m}. \tag{2.13}$$

Then, the optimal pseudo-data point and the optimal variance of the pseudo-likelihood density can be obtained as:

$$\begin{pmatrix} \sigma^* \\ y^* \end{pmatrix} = \arg\min_{\sigma, y} D_{\mathrm{KL}}(q^*||q; \sigma, y). \tag{2.14}$$

Equation (2.14) uses the so-called forward mode of KL divergence – the distribution to be approximated (q^*) is the first argument, and the approximating distribution (q) is the second. KL divergence isn't symmetric, so the order of arguments matter. The forward mode of KL divergence forces q to cover up q^* [58]. However, the forward mode is difficult to

compute, as it involves an expectation with respect to q^*, which is as hard as the probability estimation problem we initially set out to solve. Estimating the reverse mode of KL divergence ($D_{\mathrm{KL}}(q||q^*)$) is easier, as expectations with respect to q can be easily computed. But this mode forces q to have a smaller support than q^*, or else it blows up. We use the forward mode in our algorithm as it ensures that q always encompasses $q*$, so that no regions that trigger the rare event are excluded. The computational intractability of the forward mode doesn't affect our approach, as analytical expressions for D_{KL}, y^*, and σ^* exist. We derive these expressions next.

By definition of the KL divergence, we have,

$$\begin{aligned} D_{\mathrm{KL}}\left(q^*||q\right) &= \int_{\mathbb{R}^d} \frac{\mathbf{1}_{\mathbb{Y}}(f(\boldsymbol{m}))p(\boldsymbol{m})}{\mu} \log \frac{\mathbf{1}_{\mathbb{Y}}\left(f(\boldsymbol{m})\right)p(\boldsymbol{m})}{\mu q(\boldsymbol{m})} \mathrm{d}\boldsymbol{m} \\ &= \frac{1}{\mu}\int_{f^{-1}(\mathbb{Y})} p(\boldsymbol{m})\Big(\log\frac{p(\boldsymbol{m})}{q(\boldsymbol{m})} - \log\mu\Big)\mathrm{d}\boldsymbol{m} \\ &= \frac{1}{\mu}\int_{f^{-1}(\mathbb{Y})} p(\boldsymbol{m})\log\frac{p(\boldsymbol{m})}{q(\boldsymbol{m})}\mathrm{d}\boldsymbol{m} - \log\mu. \end{aligned} \tag{2.15}$$

where $f^{-1}(\mathbb{Y}) = \{\boldsymbol{m} \in \mathbb{R}^d : \boldsymbol{v}^\top\boldsymbol{m} + \beta \in \mathbb{Y}\}$.

Note that the pushforward density of $p(\boldsymbol{m})$ under $f(\boldsymbol{m})$ is also a Gaussian with mean $\nu = \boldsymbol{v}^\top\boldsymbol{m}_0 + \beta$, and variance $\gamma^2 = \boldsymbol{v}^\top\boldsymbol{\Sigma}_0\boldsymbol{v}$. Let $\rho^2 = \sigma^2/(\sigma^2+\gamma^2)$. It can be shown that

$$\log\frac{p(\boldsymbol{m})}{q(\boldsymbol{m})} = \frac{\left(y - f(\boldsymbol{m})\right)^2}{2\sigma^2} + \log\rho - \frac{(y-\nu)^2}{2(\sigma^2+\gamma^2)}. \tag{2.16}$$

Therefore,

$$\begin{aligned} \int_{f^{-1}(\mathbb{Y})} p(\boldsymbol{m})\log\frac{p(\boldsymbol{m})}{q(\boldsymbol{m})}\mathrm{d}\boldsymbol{m} &= \int_{f^{-1}(\mathbb{Y})}\left(\frac{\left(y-f(\boldsymbol{m})\right)^2}{2\sigma^2} + \log\rho - \frac{(y-\nu)^2}{2(\sigma^2+\gamma^2)}\right)p(\boldsymbol{m})\mathrm{d}\boldsymbol{m} \\ &= \int_{f^{-1}(\mathbb{Y})}\frac{\left(y-f(\boldsymbol{m})\right)^2}{2\sigma^2}p(\boldsymbol{m})\mathrm{d}\boldsymbol{m} + \left(\log\rho - \frac{(y-\nu)^2}{2(\sigma^2+\gamma^2)}\right)\mu. \end{aligned} \tag{2.17}$$

To continue further, we change variables to $z = f(\boldsymbol{m})$ and take advantage of our knowledge of the probability density for z, p_Z. This probability density is nothing but the push forward of $p(\boldsymbol{m})$ under f. Thus, $p_Z = \mathcal{N}(\nu, \gamma^2)$.

$$\begin{aligned}\int_{f^{-1}(\mathbb{Y})} p(\boldsymbol{m}) \log \frac{p(\boldsymbol{m})}{q(\boldsymbol{m})} \mathrm{d}\boldsymbol{m} &= \int_{\mathbb{Y}} \frac{(y-z)^2}{2\sigma^2} p_Z(z) \mathrm{d}z + \left(\log \rho - \frac{(y-\nu)^2}{2(\sigma^2+\gamma^2)} \right) \mu \\ &= \frac{y^2}{2\sigma^2}\mu + \frac{1}{2\sigma^2} \int_{\mathbb{Y}} z^2 p_Z(z) \mathrm{d}z - \frac{y}{\sigma^2} \int_{\mathbb{Y}} z p_Z(z) \mathrm{d}z \\ &+ \left(\log \rho - \frac{(y-\nu)^2}{2(\sigma^2+\gamma^2)} \right) \mu. \end{aligned} \tag{2.18}$$

Note that the two integrals in the final equation can be related to the mean and variance of a truncated normal distribution. Let $p_T(z)$ be the truncated distribution when p_Z only has support on the interval $\mathbb{Y}$. This truncated distribution is in fact the push forward under $f(\boldsymbol{m})$ of $q^*(\boldsymbol{m})$. Thus, $p_T = \mathbf{1}_{\mathbb{Y}}(z) p_Z / \mu$. We denote the mean and variance of p_T by ν_T and ${\gamma_T}^2$ respectively.

Finally,

$$\int_{f^{-1}(\mathbb{Y})} p(\boldsymbol{m}) \log \frac{p(\boldsymbol{m})}{q(\boldsymbol{m})} \mathrm{d}\boldsymbol{m} = \left(\frac{(y-\nu_T)^2 + {\gamma_T}^2}{2\sigma^2} + \log \rho - \frac{(y-\nu)^2}{2(\sigma^2+\gamma^2)} \right) \mu. \tag{2.19}$$

The final expression for the KL divergence is,

$$D_{\mathrm{KL}}(q^* || q) = \frac{(y-\nu_T)^2 + {\gamma_T}^2}{2\sigma^2} - \frac{(y-\nu)^2}{2(\sigma^2+\gamma^2)} + \log \rho - \log \mu. \tag{2.20}$$

This expression is minimized when

$$
\begin{aligned}
y^* &= \frac{\nu_T \gamma^2 - \nu \gamma_T^2}{\gamma^2 - \gamma_T^2} \\
\sigma^{*2} &= \frac{\gamma_T^2 \gamma^2}{\gamma^2 - \gamma_T^2}
\end{aligned}
\tag{2.21}
$$

Selecting the tunable parameters in this way, in fact, allows us to make the following claim regarding the resulting IS distribution:

Claim 1 (BIMC optimality). *In the affine-Gaussian case, the importance sampling density that results from the BIMC procedure is equivalent to the Gaussian distribution closest in KL divergence to* $q^*(\boldsymbol{m})$.

We devote the next subsection to proving Claim 1.

2.3.1.1 Establishing BIMC optimality

In this sub-section, we provide proof of Claim 1. We assume without loss of generality that $\boldsymbol{m}_0 = \mathbf{0}$ and $\boldsymbol{\Sigma}_0 = \mathbf{I}$. Further, denote by $\hat{\boldsymbol{v}} = \boldsymbol{v}/\|\boldsymbol{v}\|$. Now, select $\hat{\mathbf{V}}$ so that it's columns form an orthonormal basis for $\mathbb{R}^d \backslash \operatorname{span}(\hat{\boldsymbol{v}})$. Then, we have, for any $\boldsymbol{m}$:

$$
\boldsymbol{m} = \hat{\boldsymbol{v}}\hat{\boldsymbol{v}}^\top \boldsymbol{m} + \hat{\mathbf{V}}\hat{\mathbf{V}}^\top \boldsymbol{m} = \hat{\boldsymbol{v}} m_1 + \hat{\mathbf{V}} \boldsymbol{m}_\perp. \tag{2.22}
$$

where $m_1 := \hat{\boldsymbol{v}}^\top \boldsymbol{m} \in \mathbb{R}$ and $\boldsymbol{m}_\perp := \hat{\mathbf{V}}^\top \boldsymbol{m} \in \mathbb{R}^{d-1}$.

Using this decomposition of the parameter space, notice that

$$
f(\boldsymbol{m}) = \boldsymbol{v}^\top \boldsymbol{m} + \beta = \|\boldsymbol{v}\| m_1 + \beta = \hat{f}(m_1),
$$

and $p(\boldsymbol{m}) = p_1(m_1) p_\perp(\boldsymbol{m}_\perp)$,

where, $p_1(m_1) = \mathcal{N}(0,1)$ and $p_\perp = \mathcal{N}(\mathbf{0}_\perp, \mathbf{I}_\perp)$. By $\mathbf{0}_\perp$ and $\mathbf{I}_\perp$, we refer to the $m-1$ dimensional zero vector and identity matrix respectively. Hence, such a decomposition of the parameter space enables one to express ideal IS density, q^*, as

$$q^*(\boldsymbol{m}) = \frac{\mathbf{1}_{\mathbb{Y}}(f(\boldsymbol{m}))p(\boldsymbol{m})}{\mu} = \frac{\mathbf{1}_{\mathbb{Y}}(f(m_1))p_1(m_1)}{\mu} p_\perp(\boldsymbol{m}_\perp) = q_1^*(m_1)p_\perp(\boldsymbol{m}_\perp). \tag{2.23}$$

Before we establish the optimality of the BIMC algorithm, we will require the following result on the structure of the optimal Gaussian approximation of $q^*(\boldsymbol{m}_1, \boldsymbol{m}_\perp)$.

Proposition 1. *The Gaussian distribution closest in KL divergence to* $q^*(m_1, \boldsymbol{m}_\perp) = \mathbf{1}_{\mathbb{Y}}(\hat{f}(m_1))p_1(m_1)p_\perp(\boldsymbol{m}_\perp)/\mu$ *must be of the form* $q_{1,\text{opt}}(m_1)p_\perp(\boldsymbol{m}_\perp)$*, where* $q_{1,\text{opt}}(m_1)$ *is the closest Gaussian approximation of* $\mathbf{1}_{\mathbb{Y}}(\hat{f}(m_1))p_1(m_1)/\mu$*.*

Proof. Let $\mathcal{G}^d$ denote the set of all Gaussian distributions over $\mathbb{R}^d$. Any Gaussian distribution in $\mathbb{R}^d$ can be expressed as a joint density over the variables $m_1, \boldsymbol{m}_\perp$, $q(m_1, \boldsymbol{m}_\perp)$. Then, the closest Gaussian approximation of $q^*(m_1, \boldsymbol{m}_\perp)$ is given by:

$$q_{\text{opt}}(m_1, \boldsymbol{m}_\perp) = \underset{q \in \mathcal{G}^d}{\arg\min}\, D_{\text{KL}}\left(q^*(m_1, \boldsymbol{m}_\perp) || q(m_1, \boldsymbol{m}_\perp)\right).$$

Using the definition of KL divergence, we have,

$$D_{\text{KL}}\left(q^*(m_1, \boldsymbol{m}_\perp) || q(m_1, \boldsymbol{m}_\perp)\right) = \int q^*(m_1, \boldsymbol{m}_\perp) \log \frac{q^*(m_1, \boldsymbol{m}_\perp)}{q(m_1, \boldsymbol{m}_\perp)} \mathrm{d}m_1 \mathrm{d}\boldsymbol{m}_\perp. \tag{2.24}$$

To simplify notation, denote $\mathbf{1}_{\mathbb{Y}}(\hat{f}(m_1))p_1(m_1)/\mu$ with $q_1^*(\boldsymbol{m}_1)$. Now, using the fact that $q(m_1, \boldsymbol{m}_\perp) = q_1(m_1)q_\perp(\boldsymbol{m}_\perp|m_1)$, the chain rule of KL divergence gives:

$$D_{\mathrm{KL}}(q^*(m_1, \boldsymbol{m}_\perp)||q(m_1, \boldsymbol{m}_\perp)) \\ = D_{\mathrm{KL}}(q_1^*(m_1)||q_1(m_1)) + \mathbb{E}_{q_1^*}\left[D_{\mathrm{KL}}(p_\perp(\boldsymbol{m}_\perp)||q_\perp(\boldsymbol{m}_\perp|m_1))\right].$$

Then, because both terms are positive,

$$\min_{q\in\mathcal{G}^d} D_{\mathrm{KL}}(q^*(m_1, \boldsymbol{m}_\perp)||q(m_1, \boldsymbol{m}_\perp)) = \min_{q_1(m_1)q_\perp(\boldsymbol{m}_\perp|m_1)\in\mathcal{G}^d} D_{\mathrm{KL}}(q_1^*(m_1)||q_1(m_1)) \\ + \min_{q_1(m_1)q_\perp(\boldsymbol{m}_\perp|m_1)\in\mathcal{G}^d} \mathbb{E}_{q_1^*}\left[D_{\mathrm{KL}}(p_\perp(\boldsymbol{m}_\perp)||q_\perp(\boldsymbol{m}_\perp|m_1))\right].$$

Since the KL divergence is a positive quantity, $\mathbb{E}_{q_1^*}\left[D_{\mathrm{KL}}(p_\perp(\boldsymbol{m}_\perp)||q_\perp(\boldsymbol{m}_\perp|m_1))\right] \geq 0$. The equality is achieved iff $q_\perp(\boldsymbol{m}_\perp|m_1) = p_\perp(\boldsymbol{m}_\perp)$. Hence, $D_{\mathrm{KL}}(p_\perp(\boldsymbol{m}_\perp)||q_\perp(\boldsymbol{m}_\perp|m_1))$ is minimized when $q_\perp(\boldsymbol{m}_\perp|m_1) = p_\perp(\boldsymbol{m}_\perp)$. By inspection, the first term is minimized by $q_{1,\mathrm{opt}}(m_1)$, the closest Gaussian approximation of $q_1^*(m_1)$. Thus, $q_{\mathrm{opt}} = q_{1,\mathrm{opt}}(m_1)p_\perp(\boldsymbol{m}_\perp)$. □

Proposition 1 states that for the affine-Gaussian case, q_{opt} must marginalize to the corresponding marginal of $p(\boldsymbol{m})$ in all directions in parameter space to which $f(\boldsymbol{m})$ is insensitive. Note that in the proof, the affine property of $f(\boldsymbol{m})$ was never explicitly used. Hence, this result can be easily extended to arbitrary non-linear $f(\boldsymbol{m})$ in the following sense. If there are *global* directions in parameter space to which $f(\boldsymbol{m})$ is insensitive, an optimal Gaussian or Gaussian mixture approximation of q^* must marginalize to the corresponding marginal of $p(\boldsymbol{m})$ in those directions. We will formalize this intuition and discuss its implications on dimension reduction for rare-event probability estimation in Section 3.6

Next, we recall and prove Claim 1.

Claim 1 (BIMC optimality). *In the affine-Gaussian case, the importance sampling density that results from the BIMC procedure is equivalent to the Gaussian distribution closest in KL divergence to* $q^*(\boldsymbol{m})$.

Proof. We begin by showing that BIMC produces a Gaussian distribution that indeed satisfies the form prescribed by proposition 1. Let the IS distribution produced by BIMC be denoted $q_{\text{BIMC}}(x)$. Because q_{BIMC} is a Bayesian posterior distribution, it has the following form:

$$q_{\text{BIMC}}(\boldsymbol{m}) = \frac{p(y|\boldsymbol{m})p(\boldsymbol{m})}{p(y)}, \tag{2.25}$$

where,

$$\begin{aligned} p(y|\boldsymbol{m}) &\propto \exp\left(-\frac{1}{2\sigma^2}(y - f(\boldsymbol{m}))^2\right) \\ &\propto \exp\left(-\frac{1}{2\sigma^2}(y - \hat{f}(m_1))^2\right) \\ &\propto p(y|m_1). \end{aligned}$$

Also, since $p(\boldsymbol{m})$ is a standard Gaussian, it can be expressed as $p(\boldsymbol{m}) = p_1(\boldsymbol{m}_1)p_\perp(\boldsymbol{m}_\perp)$.

Therefore,

$$q_{\text{BIMC}}(\boldsymbol{m}) \propto p(y|m_1)p_1(m_1)p_\perp(\boldsymbol{m}_\perp). \tag{2.26}$$

Hence, the marginal distribution of $\boldsymbol{m}_\perp$ when $x \sim q_{\text{BIMC}}(\boldsymbol{m})$ is $p_\perp(\boldsymbol{m}_\perp)$, as required by proposition 1. Additionally, since $\hat{f}(m_1)$ is affine, $p(y|m_1)p_1(m_1)$ is Gaussian. All that remains to be shown is that eq. (2.14) results in parameters such that $p(y|m_1)p_1(m_1)$ is the optimal Gaussian approximation of $q_1^*(m_1) = \mathbf{1}_{\mathbb{Y}}(\hat{f})(\boldsymbol{m}_1)p_1(m_1)/\mu$.

Now, notice that $q_1^*(m_1) = \mathbf{1}_{\mathbb{Y}}(\hat{f}(m_1))p_1(m_1)/\mu$ is a truncated normal distribution. That is because

$$
\begin{aligned}
q_1^*(m_1) &= \mathbf{1}_{\mathbb{Y}}(\hat{f}(m_1))p_1(m_1)/\mu \\
&= \mathbf{1}_{[y_{\min}, y_{\max}]}(\|\boldsymbol{v}\|m_1 + \beta)p_1(m_1)/\mu \\
&= \mathbf{1}_{[\frac{y_{\min}-\beta}{\|\boldsymbol{v}\|}, \frac{y_{\max}-\beta}{\|\boldsymbol{v}\|}]}(m_1)p_1(m_1)/\mu.
\end{aligned}
$$

Thus, q_1^* is a standard normal distribution truncated over $\left[\frac{y_{\min}-\beta}{\|\boldsymbol{v}\|}, \frac{y_{\max}-\beta}{\|\boldsymbol{v}\|}\right]$. Denote the mean and variance of q_1^* by ν_T and γ_T^2. Then the optimal Gaussian approximation of q_1^* is $\mathcal{N}(\phi_T, \omega_T^2)$. Hence, we have to demonstrate that the minimizer of eq. (2.14) are such that $p(y|m_1)p_1(m_1)$ is the same as $\mathcal{N}(\phi_T, \omega_T^2)$.

The expression for $D_{\mathrm{KL}}(q^*(m_1, \boldsymbol{m}_\perp)||q(m_1, \boldsymbol{m}_\perp)$ in this case is:

$$
\begin{aligned}
D_{\mathrm{KL}}(q^*(m_1, \boldsymbol{m}_\perp)||q(m_1, \boldsymbol{m}_\perp)) = \text{const.} \; &+ \frac{\|\boldsymbol{v}\|^2}{2\sigma^2}\left(\omega_T^2 + \left(\frac{y-\beta}{\|\boldsymbol{v}\|} - \phi_T\right)^2\right) \\
&- \frac{1}{2}\frac{(y-\beta)^2}{\sigma^2 + \|\boldsymbol{v}\|^2} + \frac{1}{2}\log\frac{\sigma^2}{\sigma^2 + \|\boldsymbol{v}\|^2}.
\end{aligned}
$$

This expression is minimized in the BIMC algorithm. The minimum occurs at

$$
\begin{aligned}
y^* &= \frac{\|\boldsymbol{v}\|}{1-\omega_T^2}\phi_T + \beta \\
\sigma^{*2} &= \frac{\|\boldsymbol{v}\|^2\omega_T^2}{1-\omega_T^2}.
\end{aligned}
\tag{2.27}
$$

Since $\omega_T^2 < 1$ (Remark 2.1 in [98]), σ^{*2} is a valid variance for the likelihood distribution.

Now, it can be shown that,

$$
\frac{p(y^*|m_1)p_1(m_1)}{p(y^*)} = \mathcal{N}\left(\frac{\|\boldsymbol{v}\|}{\|\boldsymbol{v}\|^2 + \sigma^{*2}}(y^* - \beta), \frac{\sigma^{*2}}{\sigma^{*2} + \|\boldsymbol{v}\|^2}\right).
$$

Plugging in expressions for y^* and σ^{*2} from eq. (2.27), we obtain,

$$\frac{p(y^*|m_1)p_1(m_1)}{p(y^*)} = \mathcal{N}(\phi_T, \omega_T^2).$$

Therefore, $p(y^*|m_1)p_1(m_1)/p(y^*)$ is the Gaussian closest in KL divergence to $\mathbf{1}_{\mathbb{Y}}(\hat{f}(\boldsymbol{m}_1)p_1(\boldsymbol{m}_1)/\mu$. Hence, by proposition 1, $q_{\text{BIMC}}(\boldsymbol{m}) = p(y^*|m_1)p_1(m_1)p_\perp(\boldsymbol{m}_\perp)/p(y^*)$ must be the closest Gaussian distribution to $q^*(\boldsymbol{m}_r, \boldsymbol{m}_\perp)$ □

Hence, BIMC is implicitly searching for the best Gaussian approximation of $q^*(\boldsymbol{m})$. A Gaussian distribution in m dimensions has $m(m+1)/2$ free variables, so a naive search for the best Gaussian approximation of $q^*(\boldsymbol{m})$ will optimize over all $\mathcal{O}(m^2)$ free variables. However, BIMC accomplishes this task be optimizing just two free variables. This can be attributed to the similar structure of the pseudo-posterior $p(y|\boldsymbol{m})p(\boldsymbol{m})/p(y)$, and the ideal IS density, $\mathbf{1}_{\mathbb{Y}}(f(\boldsymbol{m}))p(\boldsymbol{m})/\mu$.

To verify whether minimizing D_{KL} to obtain parameters actually translates to improved performance of our IS density, we synthesized a affine map from $\mathbb{R}^{100}$ to $\mathbb{R}$ (implementation details are provided in the appendix in Section A.1). We measure performance by the relative RMSE in the probability estimate, $\tilde{e}_{\text{RMS}}$, and we expect $\tilde{e}_{\text{RMS}}$ to be small when $y = y^*$ and $\sigma = \sigma^*$. In addition, in this case, μ is available to us analytically. This provides yet another indicator of performance- the absolute difference between the analytical value and the IS estimate must be small when the optimal parameters are being used.

Figure 2.2 shows the variation of D_{KL} with σ^2 at various y in addition to the optimal (σ, y) combination that results from numerical optimization. We conclude the following from the figure:

- The optimal pseudo-data point lies almost exactly at the mid-point of $\mathbb{Y}$.

- D_{KL} is extremely sensitive to the spread of the pseudo-likelihood probability density σ, much more so than the pseudo-data y. Intuitively, a large value for σ emphasizes the pseudo-prior over the data so that sampling from $q(\boldsymbol{m})$ is akin to sampling from $p(\boldsymbol{m})$. On the other hand, too small a value for σ^2 results in $q(\boldsymbol{m})$ not having enough spread to cover the region where $f(\boldsymbol{m}) \in \mathbb{Y}$, which could result in significant bias when the number of samples is small.

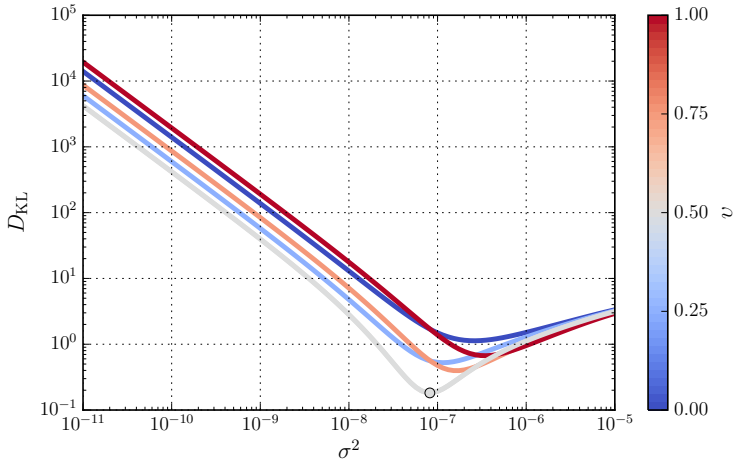

Figure 2.2: *This figure shows the variation of D_{KL} at various values of the data point y and pseudo-likelihood variance σ^2. Here, the data point y has been normalized to $\upsilon = (y - y_{\min})/(y_{\max} - y_{\min})$ and $f(\boldsymbol{m})$ is an affine transformation from $\mathbb{R}^{100}$ to $\mathbb{R}$. The marker shows the (σ, υ) combination that resulted from numerical minimization of D_{KL}.*

In Figure 2.3, we fix $y = y^*$ and plot the variation of the probability estimate, $\tilde{\mu}$, and the relative RMSE, $\tilde{e}_{\mathrm{RMS}}$, with σ^2. For each value of σ^2, we performed several independent runs. Figure 2.3a plots $\tilde{\mu}$ obtained from each run. In Figure 2.3b, we plot the ensemble average of $\tilde{e}_{\mathrm{RMS}}$ over all simulations at fixed σ^2. Both figures demonstrate that when σ^2 is small, both the probability estimate and the associated RMSE have significant bias (shaded region in the figures). When σ^2 is large, error increases with σ^2 since the emphasis on pseudo-data decreases. There lies an optimal σ^2 somewhere in between, and indeed, minimizing D_{KL}

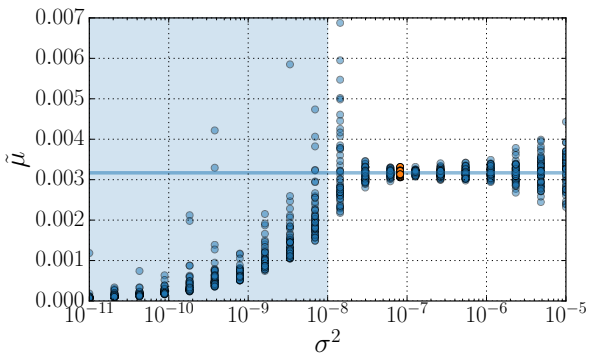

(a) *The IS probability estimate $\tilde{\mu}$ against σ^2 at $y = y^*$. Each marker indicates $\tilde{\mu}$ from an individual run. The solid line indicates the true value of μ. The markers in orange denote runs at $\sigma = \sigma^*$.*

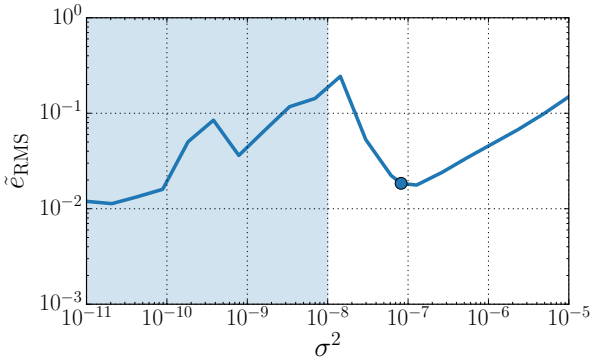

(b) *The relative RMSE $\tilde{e}_{\mathrm{RMS}}$ against σ^2 at $y = y^*$. Only the average $\tilde{e}_{\mathrm{RMS}}$ over all runs at fixed σ^2 is plotted. The marker is at $\sigma = \sigma^*$.*

Figure 2.3: *This figure shows the variation of the probability estimate $\tilde{\mu}$ and the relative RMSE $\tilde{e}_{\mathrm{RMS}}$ with the likelihood variance σ^2. At fixed σ^2, we performed 50 independent runs using $N = 1000$ samples. For $\tilde{\mu}$, we plot the probability estimate obtained from each run, whereas for $\tilde{e}_{\mathrm{RMS}}$, we plot the ensemble average at each σ.*

helps identify it. So far we've been using just one pseudo-data point $y \in \mathbb{Y}$. However, it is also possible to use multiple pseudo-data points, $\{y_i\}_{i=1}^n, y_i \in \mathbb{Y}$. In this case, using the same pseudo-likelihood density for all y_i, a posterior $p(\boldsymbol{m}|y_i)$ and its corresponding Gaussian approximation can be obtained for each y_i. These Gaussians can then be collected into a mixture distribution to form the IS density. So, a possibility is to use the following IS density:

$$q(\boldsymbol{m}) = \frac{1}{n}\sum_{i=1}^{n} \mathcal{N}\left(\boldsymbol{m}_{\text{MAP}}^{(i)}, \left(\mathbf{H}_{\text{GN}}^{(i)}\right)^{-1}\right). \tag{2.28}$$

where $\boldsymbol{m}_{\text{MAP}}^{(i)}$ is the MAP point corresponding to y_i and $\mathbf{H}_{\text{GN}}^{(i)}$ is the Hessian matrix of $-\log p(\boldsymbol{m}|y_i)$ at $\boldsymbol{m}_{\text{MAP}}^{(i)}$. Next, we investigate whether using $n > 1$ pseudo-data points in $\mathbb{Y}$ leads to better performance than using just one pseudo-data point, i.e., $n = 1$.

To ensure a fair comparison between the two cases, they must each be run using their respective optimal parameters. When $n > 1$, the tunable parameters are the number of pseudo-data points, n, their values, $\{y_i\}_{i=1}^n$, and the variance of the common pseudo-likelihood density, σ^2. However, minimizing the Kullback-Leibler distance between q and q^* to obtain parameters is no longer possible. This is because the Kullback-Leibler distance between two Gaussian mixtures doesn't have a closed form expression [42]. To proceed, given $n > 1$, we fix $\{y_i\}$ to be n evenly spaced points in $\mathbb{Y}$. We then sweep over several values of n and σ^2 to investigate whether increasing n has any advantages.

Empirical evidence seems to suggest no. In Figure 2.4, we plot the variation of the ensemble averaged $\tilde{e}_{\text{RMS}}$ with σ^2 at various values of n and using various forward models, both linear and non-linear (details of the forward models are provided in the appendix in Section A.1). While the error decreases with increasing n for some cases, we believe the decrease isn't large enough to justify the increased computational cost of solving additional inverse problems.

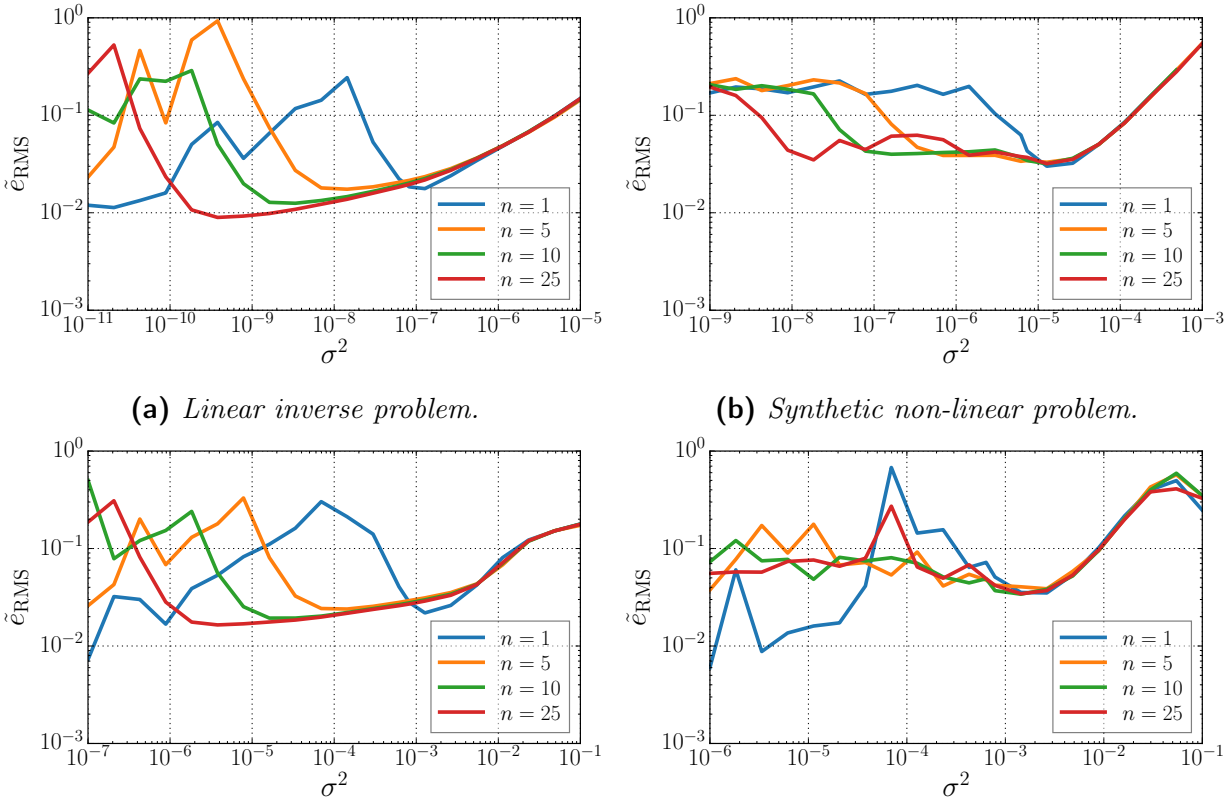

(a) *Linear inverse problem.*

(b) *Synthetic non-linear problem.*

(c) *Single step reaction.*

(d) *Elliptic PDE.*

Figure 2.4: *This figure shows how* $\tilde{e}_{\mathrm{RMS}}$ *varies with* σ^2 *at different values of* n *for various forward models. At fixed* σ^2*, we perform 50 independent simulations and report the ensemble averaged* $\tilde{e}_{\mathrm{RMS}}$*. When* $n = 1$*, we use the optimal data point obtained employing the appropriate tuning strategy described in the text. When* $n > 1$*, we select* n *evenly spaced points in* $\mathbb{Y}$*. Similar to Figure 2.3, IS estimates are biased when* σ^2 *is small. The extent of the biased regions depends on* n *and appears to decrease as* n *increases.*

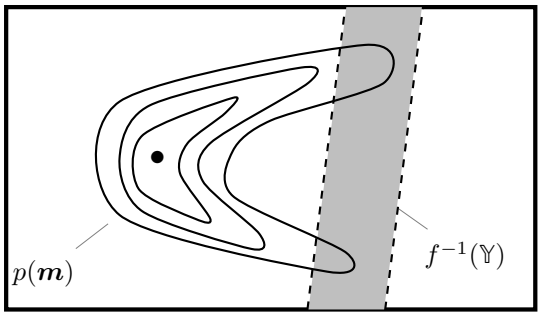

Figure 2.5: *Arbitrary unimodal p. In this case, the true posterior and the ideal IS density are multimodal. The optimizer used for computing $\boldsymbol{m}_{\text{MAP}}$ will only find one of these modes. Our IS density will then only sample around that mode, leading to incorrect estimates.*

2.3.2 Affine f, mixture-of-Gaussians p

If $p(\boldsymbol{m})$ is a mixture of Gaussians, $p(\boldsymbol{m}) = \sum_{i=1}^{k} w_i p_i(\boldsymbol{m})$, then, notice that,

$$\mu = \int \mathbf{1}_{\mathbb{Y}}\left(f(\boldsymbol{m})\right) p(\boldsymbol{m}) \mathrm{d}\boldsymbol{m} = \sum_{i=1}^{k} w_i \int \mathbf{1}_{\mathbb{Y}}\left(f(\boldsymbol{m})\right) p_i(\boldsymbol{m}) \mathrm{d}\boldsymbol{m} = \sum_{i=1}^{k} w_i \mu_i \tag{2.29}$$

The contribution to μ from each component $p_i(\boldsymbol{m})$, μ_i, can then be calculated using BIMC as described above. If $\tilde{\mu}_i$ is the estimate from each component, μ can be estimated as $\tilde{\mu} = \sum_{i=1}^{k} w_i \tilde{\mu}_i$.

2.3.3 Affine f, arbitrary unimodal p

In this case, even though p is unimodal, q^*, and the pseudo-posterior $p(\boldsymbol{m}|y)$, can be multimodal (see Figure 2.5). Then, depending on the initial guess provided, the optimizer used for computing the MAPs may converge to only one of the modes. A local Gaussian characterization of the pseudo-posterior will only sample near this mode and all the other modes will be ignored. This will cause μ to be underestimated. To avoid this, we propose approximating p with a mixture of Gaussians and then proceeding with the methodology outlined in the

previous section. This will lead to an estimate whose accuracy is as good as the accuracy in approximating p with a mixture of Gaussians.

2.3.4 Non-linear f, Gaussian p

When $f(\boldsymbol{m})$ is non-linear, the KL divergence may not have a tractable closed-form expression even when only one pseudo-data point is used. Although a sample based estimate of the KL divergence can be obtained, it would require evaluating $f(\boldsymbol{m})$ for each sample, increasing the cost of constructing the IS density. To compute the optimal parameters in this case, we instead propose linearizing $f(\boldsymbol{m})$ around the MAP point corresponding to an initial pseudo-data point, $y^{\text{mid}} = \text{mid}\,\mathbb{Y}$, which we denote $\boldsymbol{m}^{\text{mid}}_{\text{MAP}}$. This necessitates solving another optimization problem (as in Equation (2.8)), for which we require σ^2, a quantity we set out to tune in the first place. However, this σ^2 is only used to construct the linearization and has little bearing on subsequent sampling. We recommend setting $\sigma = 0.1(y_{\max} - y_{\min})$. Once we have $\boldsymbol{m}^{\text{mid}}_{\text{MAP}}$, we linearize $f(\boldsymbol{m})$ as follows:

$$f(\boldsymbol{m}) \approx f(\boldsymbol{m}^{\text{mid}}_{\text{MAP}}) + \mathbf{J}^{\text{mid}}(\boldsymbol{m} - \boldsymbol{m}^{\text{mid}}_{\text{MAP}}) \tag{2.30}$$

Here, $\mathbf{J}^{\text{mid}} \in \mathbb{R}^{1\times m}$ is the Jacobian matrix of the $f(\boldsymbol{m})$ evaluated at $\boldsymbol{m}^{\text{mid}}_{\text{MAP}}$. From here on, we can proceed to obtain the optimal parameters as in the affine case by identifying $\boldsymbol{v}^\top \equiv \mathbf{J}^{\text{mid}}$ and $\beta \equiv f(\boldsymbol{m}^{\text{mid}}_{\text{MAP}}) - \mathbf{J}^{\text{mid}}\boldsymbol{m}^{\text{mid}}_{\text{MAP}}$. Note that such a procedure will not reveal the true optimal parameters that correspond to the non-linear forward model. It only provides an estimate, but allows us to use analytically derived expressions and keep computational costs low. Another consequence of linearizing $f(\boldsymbol{m})$ is that it allows for the analytical computation of the rare event probability associated with the linearized map (Equation (2.10)). We will refer to this estimate of μ as the linearized probability estimate, μ_{lin}.

2.3.5 Non-linear f, mixture-of-Gaussian p

This case is similar to Section 2.3.2. Recall that μ is just the weighted sum of probability corresponding to each component mixtures, μ_i. Each μ_i can be estimated by the method outlined above, and then weighed and summed to obtain an estimate for μ.

Procedure 1 BIMC

Input: $f(\boldsymbol{m})$, $p(\boldsymbol{m})$, $\mathbb{Y}$, N
Output: $\tilde{\mu}$

% Select optimal parameters, y^*, σ^*
$y^{\max} \leftarrow \max \mathbb{Y}$, $y^{\min} \leftarrow \min \mathbb{Y}$, $y^{\text{mid}} \leftarrow 0.5(y^{\min} + y^{\max})$
$\sigma_0 \leftarrow 0.1(y^{\max} - y^{\min})$
$\boldsymbol{m}_{\text{MAP}}^{\text{mid}} \leftarrow \texttt{getMAP}(y_{\text{mid}}, \sigma_0)$ % Minimize Equation (2.7) using $y = y^{\text{mid}}, \sigma = \sigma_0$
$\boldsymbol{v}^\top \leftarrow \left.\frac{\partial f(\boldsymbol{m})}{\partial \boldsymbol{m}}\right|_{\boldsymbol{m}=\boldsymbol{m}_{\text{MAP}}}$
$\beta \leftarrow f(\boldsymbol{m}_{\text{MAP}}^{\text{mid}}) - \boldsymbol{v}^T \boldsymbol{m}_{\text{MAP}}^{\text{mid}}$
$(y^*, \sigma^*) \leftarrow \texttt{minimizeKLDiv}(\boldsymbol{v}, \beta, p)$ % Minimize $D_{\text{KL}}(q^* || q)$ as in Equation (2.20)

% Build IS density using optimal parameters
$\boldsymbol{m}_{\text{MAP}} \leftarrow \texttt{getMAP}(y^*, \sigma^*)$ % Minimize Equation (2.7) using $y = y^*, \sigma = \sigma^*$
$\mathbf{H}_{\text{GN}} \leftarrow \texttt{getHessian}(\boldsymbol{m}_{\text{MAP}}, y^*, \sigma^*)$ % Compute Hessian of Equation (2.7) at $\boldsymbol{m}_{\text{MAP}}$ using $y = y^*, \sigma = \sigma^*$
$q(\boldsymbol{m}) \leftarrow \mathcal{N}(\boldsymbol{m}_{\text{MAP}}, \mathbf{H}_{\text{GN}}^{-1})$

% Sample from q to estimate μ
for $i = 1, \ldots, N$ **do**
    $\boldsymbol{m}_i \sim q(\boldsymbol{m})$
    $w_i \leftarrow \mathbf{1}_{\mathbb{Y}}(f(\boldsymbol{m}_i)) p(\boldsymbol{m}_i) / q(\boldsymbol{m}_i)$
end for
$\tilde{\mu} \leftarrow \sum_{i=1}^{N} w_i / N$
return $\tilde{\mu}$

2.3.6 Summary

To summarize, in this section we described how a fictitious Bayesian inverse problem can be constructed from the components of the forward UQ problem. The solution of this fictitious inverse problem yields a posterior whose Gaussian approximation is our IS density. The parameters on which the IS density depends can be tuned by minimizing an analytical expression for its Kullback-Leibler divergence with respect to the ideal IS density. A drawback of our method is that we're restricted to nominal densities that are Gaussian mixtures or easily approximated by one. The overall algorithm for arbitrary, non-linear f is given in Algorithm 1. Next, we present and discuss results of our numerical experiments.

2.4 Experiments

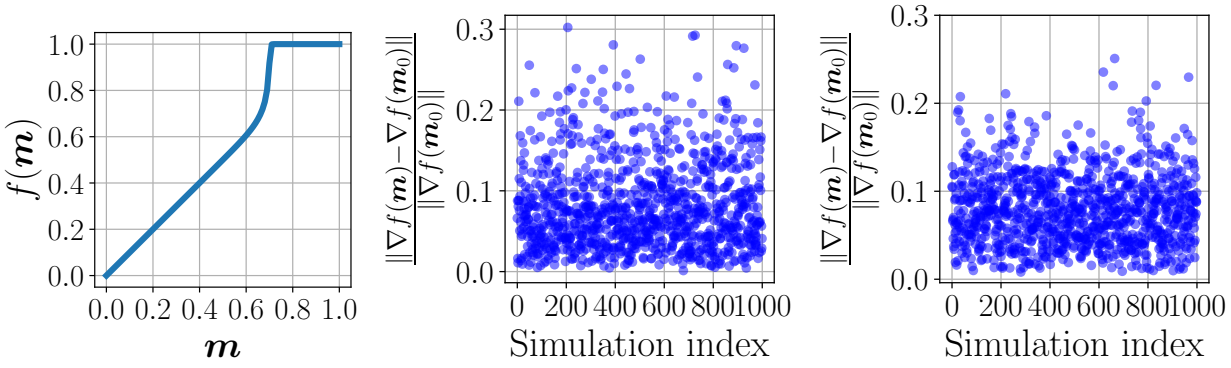

(a) *Single step reaction* **(b)** *Autoignition* **(c)** *Synthetic non-linear*

Figure 2.6: *Non-linearity of f. For the single step reaction problem, we plot the full forward map f for all possible values of the input $\boldsymbol{m}$. For the autoignition and synthetic non-linear problems, we demonstrate how $\nabla f(\boldsymbol{m})$ varies. We draw samples, $\boldsymbol{m}_i$, from $p(\boldsymbol{m})$, and evaluate $\|\nabla f(\boldsymbol{m}) - \nabla f(\boldsymbol{m}_0)\|/\|\nabla f(\boldsymbol{m}_0)\|$, where $\boldsymbol{m}_0$ is the prior mean. Departure from 0 of this quantity signifies the degree of non-linearity.*

In this section, we present results that demonstrate the efficacy of our method. We also report cases where our method fails (detailed discussion about failure mechanisms of BIMC

is postponed to the end of this section). The forward models we used in our experiments are briefly summarized below. A detailed description of the models and the problem setup is given in the supplement in Section A.1. Figure 2.6 shows the variation of f for select models and demonstrates that it is indeed non-linear.

- Affine case: In this case $f(\boldsymbol{m})$ is a affine map from $\mathbb{R}^d$ to $\mathbb{R}$. We choose $m = 2$ for illustration, and $m = 100$ for comparison with MC.

- Synthetic non-linear problem: In this case, $f(\boldsymbol{m})$ is defined to be the following map from $\mathbb{R}^m$ to $\mathbb{R}$.

$$f(\boldsymbol{m}) = \boldsymbol{o}^\top \boldsymbol{u}, \text{ where } \left(\mathbf{S} + \varepsilon \boldsymbol{m}\boldsymbol{m}^\top\right) \boldsymbol{u} = \boldsymbol{b}. \tag{2.31}$$

  Here, $\varepsilon \in \mathbb{R}$, $\boldsymbol{o}, \boldsymbol{u}, \boldsymbol{b} \in \mathbb{R}^m$, and $\mathbf{S} \in \mathbb{R}^{d\times d}$. Again, $m = 2$ was chosen for illustration and $m = 10$ for comparison with MC.

- Single step reaction: The forward model here describes a single step chemical reaction using an Arrhenius type rate equation. A progress variable $u \in [0, 1]$ is used to describe the reaction. The parameter $\boldsymbol{m}$ is the initial value of progress variable $u(0)$ and the observable $f(\boldsymbol{m})$ is the value of the progress variable at some final time $t_f, u(t_f)$. Thus $f(\boldsymbol{m})$ is a map from $\mathbb{R}$ to $\mathbb{R}$.

- Autoignition: Here, we allow a mixture of hydrogen and air to undergo autoignition in a constant pressure reactor. A simplified mechanism with 5 elementary involving 8 chemical species is used to describe the chemistry. The parameter $\boldsymbol{m}$ is the vector of the initial equivalence ratio, initial temperature and the initial pressure in the reactor and the observable is the amount of heat released so that $f(\boldsymbol{m})$ is a map from from $\mathbb{R}^3$ to $\mathbb{R}$.

- Elliptic PDE: In this system, we invert for the discretized log-permeability field in some spatial domain given an observation of the pressure at some point. The forward problem, that is, obtaining the pressure from the log-permeability field, is governed by an elliptic PDE. A finite element discretization results in $f(\boldsymbol{m})$ being a map from $\mathbb{R}^{4225}$ to $\mathbb{R}$.

- The Lorenz system: Here, the forward problem is governed by the chaotic Lorenz equations [54]. The parameter $\boldsymbol{m}$ is the initial condition of the system while the observable is value of the first component of the state vector at some final time t_f. We simulate the Lorenz system over three time horizons, $t_f = 0.1$s, $t_f = 5$s, and $t_f = 15$s. BIMC fails over longer time horizons, i.e., when $t_f = 5$s and $t_f = 15$s.

- Periodic case: Here, $f(\boldsymbol{m})$ is a periodic function in $\mathbb{R}^2$, $f(\boldsymbol{m}) = \sin(x_1)\cos(x_2)$. This is another case when BIMC fails.

Sampling illustration We begin by presenting examples in low-dimensions that illustrate the quality of samples from BIMC. In Figure 2.7, we compare samples generated using MC and BIMC. We also depict the ideal IS density q^* in the figures, either using contours, or through samples. As expected, the variance of the IS density in our method is only decreased in one data-informed direction. The extent of this decrease depends on the variance of the pseudo-likelihood density, $p(y|\boldsymbol{m})$, and a tuning algorithm based on minimizing the Kullback-Leibler distance leads to a good fit between the spread of $q^*(\boldsymbol{m})$ and $q(\boldsymbol{m})$ in this direction. In all other directions, the spread of $q(\boldsymbol{m})$ is same as that of $p(\boldsymbol{m})$. This is because the pseudo-data y does not inform these directions.

As a quantitative estimate of the quality of samples, we report the acceptance ratio, defined as the fraction of samples that evaluate inside $\mathbb{Y}$. The acceptance ratio resulting from BIMC is plotted in Figure 2.8 (the acceptance ratio from MC on the other hand is $\hat{\mu}$ by definition).

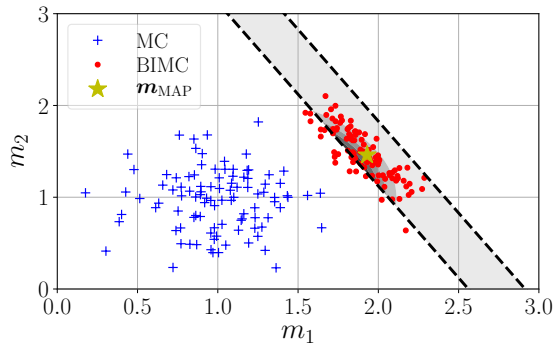

(a) *The affine case.*

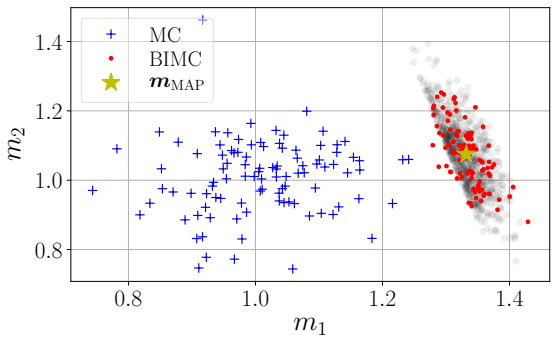

(b) *The synthetic non-linear case.*

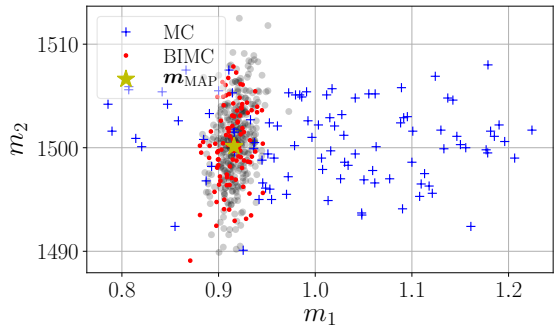

(c) *Autoignition,* m_1 *-* m_2 *plane.*

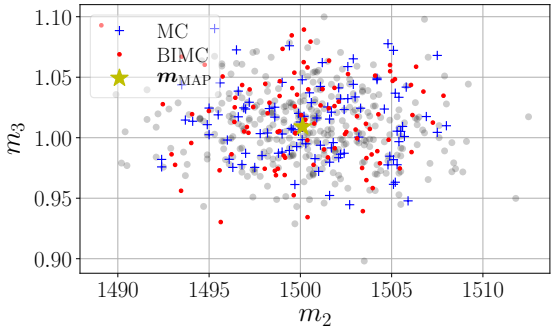

(d) *Autoignition,* m_2 *-* m_3 *plane.*

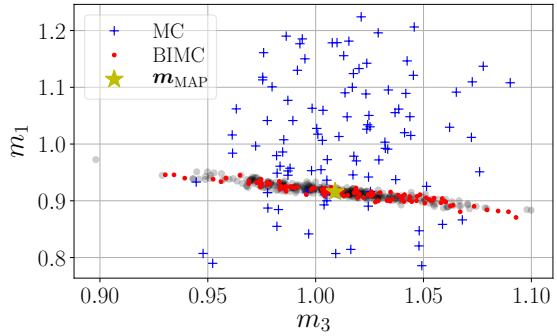

(e) *Autoignition,* m_3 *-* m_1 *plane.*

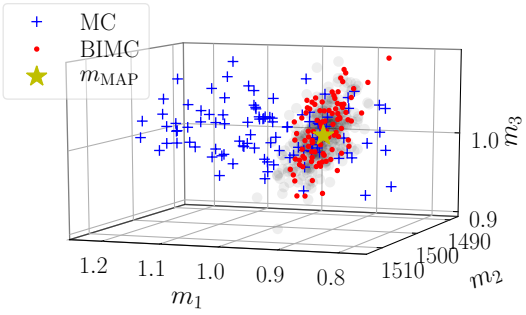

(f) *Autoignition, 3D view.*

Figure 2.7: *Sampling illustration. In this figure, we plot 100 samples from* $p(\boldsymbol{m})$ *(which corresponds to vanilla MC) as well as* $q(\boldsymbol{m})$ *(which corresponds to BIMC) with* $n = 1$ *for the affine, synthetic non-linear, and the autoignition problems. For the affine case (a), the region in* $\mathbb{R}^2$ *that evaluates inside* $\mathbb{Y}$ *is analytically available and is plotted between the thick, dashed lines. Also analytically available is the ideal IS density* q^* *whose contours are plotted. For all other forward models, a scatter plot of samples drawn from* q^* *is used to represent its magnitude.*

We observe that $n = 1$ consistently leads to an acceptance ratio of around 90% irrespective of μ (except in the Periodic and Lorenz, $t_f = 5$s cases; these are failure cases and will be discussed at the end of this section). The slight dip in the acceptance ratio when $n > 1$ can be attributed to the effect of always having $y_{\min}$ and $y_{\max}$ as data points. Because these points lie at the edge of the interval $\mathbb{Y}$, they lead to an increased number of samples that are close to these limit points, but don't actually evaluate inside $\mathbb{Y}$. As n increases however, the number of samples drawn from mixture components corresponding to these two points decreases and the acceptance ratio shows an upward trend.

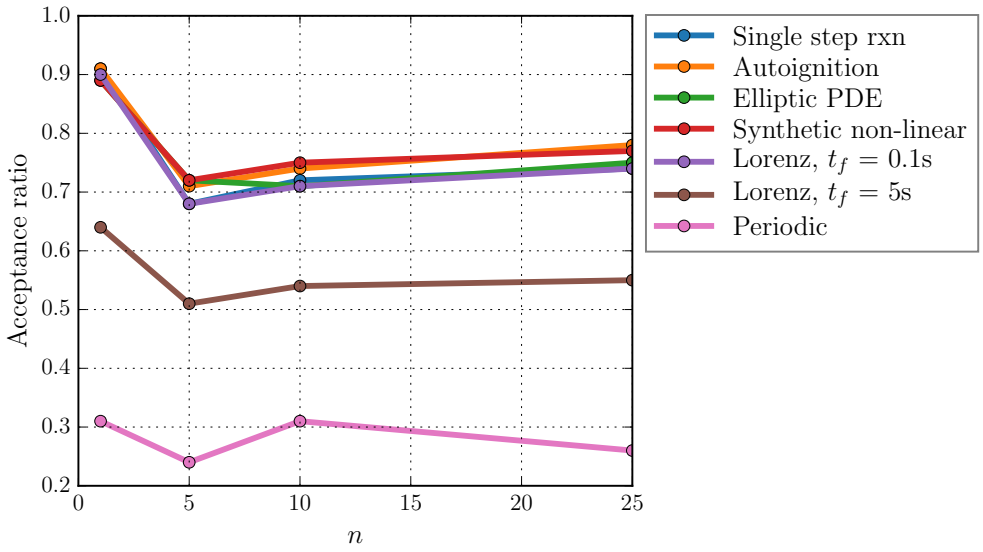

Figure 2.8: *Fraction of samples that evaluate inside $\mathbb{Y}$ for the different forward models at various values of n. In this experiment $N = 1000$ and μ spans two orders of magnitude, from $\mathcal{O}(10^{-2})$ to $\mathcal{O}(10^{-4})$. The BIMC methodology fails for the periodic and Lorenz, $t_f = 5s$ cases, hence the lower acceptance ratio.*

Convergence with number of samples Next, we compare the relative RMS error, e_{RMS}, from MC and BIMC in Figure 2.9. BIMC offers the same accuracy using far fewer number of samples and results in an order of magnitude or more of speedup. The exact speedup

achieved depends on the magnitude of the probability. In addition, there is little asymptotic effect of using $n > 1$.

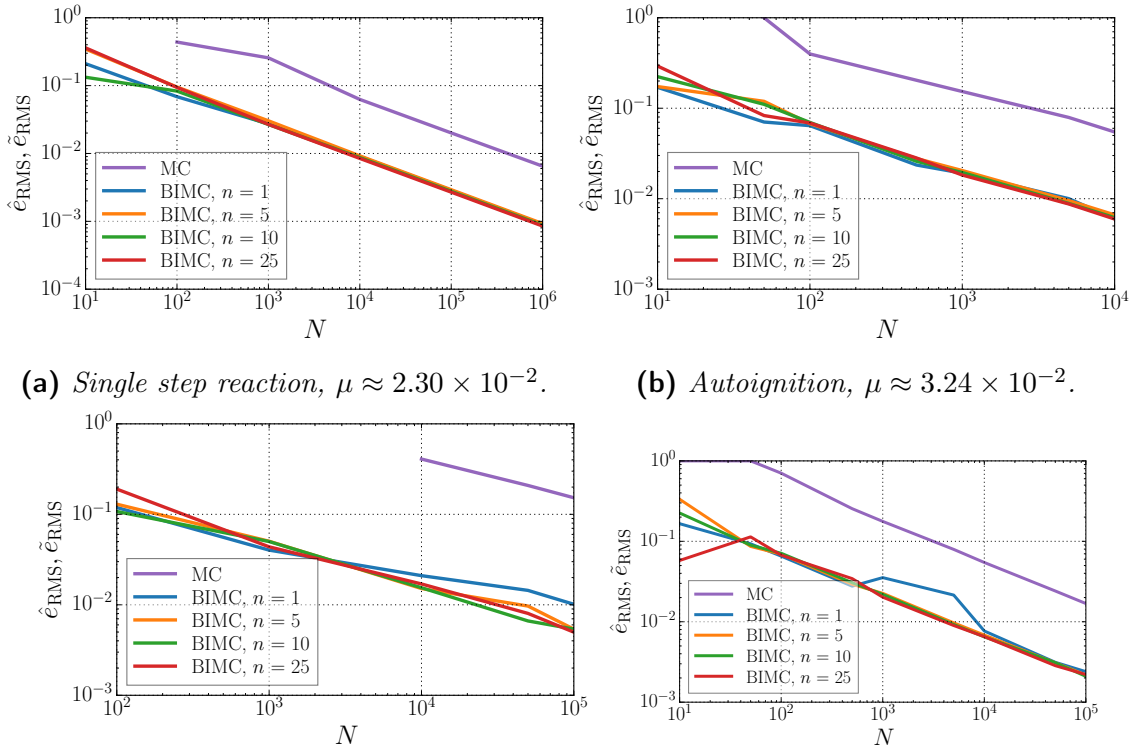

(a) *Single step reaction,* $\mu \approx 2.30 \times 10^{-2}$. **(b)** *Autoignition,* $\mu \approx 3.24 \times 10^{-2}$.

(c) *Elliptic PDE,* $\mu \approx 3.91 \times 10^{-4}$. **(d)** *Lorenz,* $t_f = 0.1s.$, $\mu \approx 3.28 \times 10^{-2}$.

Figure 2.9: *Comparison of performance of MC and BIMC. The variation of the relative RMSE,* e_{RMS}*, is plotted against the number of samples* N*. For reference, the most accurate probability estimate is also reported.*

Effect of probability magnitude In Figure 2.10, we study the effect of the probability magnitude on the relative RMSE, $\tilde{e}_{\mathrm{RMS}}$. We notice that BIMC is only weakly dependent on the probability magnitude. This is because selecting parameters by minimizing D_{KL} leads to an IS density that is optimally adapted for sampling around $\mathbb{Y}$.

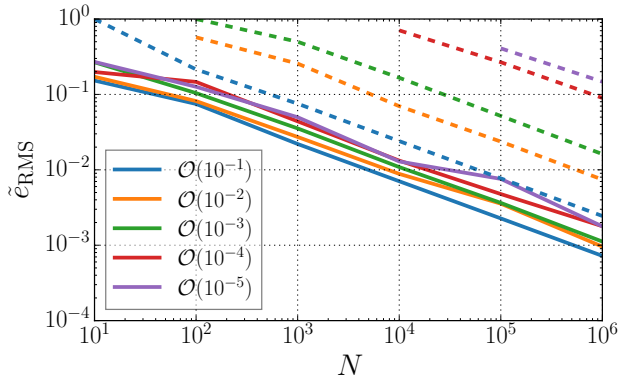

(a) *Synthetic non-linear problem*

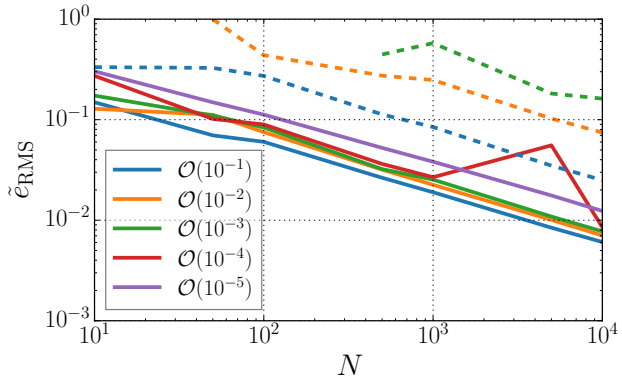

(b) *Autoignition*

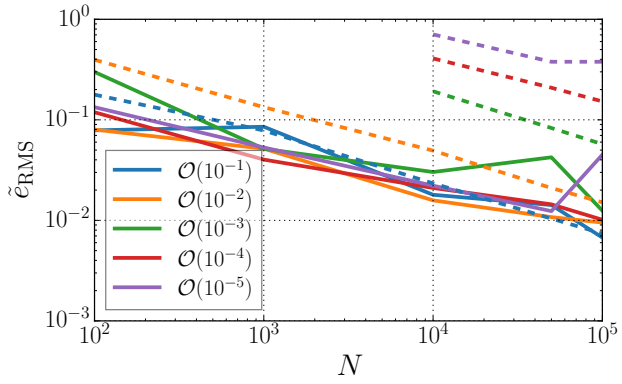

(c) *Elliptic PDE*

Figure 2.10: *Effect of varying probability levels. In this figure, we plot the variation of ensemble averaged relative* $\tilde{e}_{\mathrm{RMS}}$ *with the number of samples* N *for various forward models with varying levels of probability. The varying probability levels are selected by moving* $\mathbb{Y}$ *to the tail regions of* $p(\boldsymbol{m})$*. The dashed lines indicate errors associated with MC while the solid lines indicate errors in BIMC.*

Extremely rare events In our final experiment, we push BIMC to compute probabilities of extremely rare events. The rare events were constructed by shifting $\mathbb{Y}$ further and further into the tail region of the push forward of $p(\boldsymbol{m})$ under f. BIMC is able to compute extremely small probabilities using a modest number of samples. This experiment also corroborates our claim that the accuracy of our method is only weakly dependent on the probability magnitude μ. We also report the probability estimate resulting from linearizing $f(\boldsymbol{m})$ around $\boldsymbol{m}^{\text{mid}}$ and conclude that the linearized probability estimate is a good indicator of the order of magnitude of the true probability.

Table 2.2: *Extremely rare events, $N = 1000$.*

BIMC, $n = 1$		BIMC, $n = 5$		Linearized
$\tilde{\mu}^N$	$\tilde{e}^N_{\text{RMS}}$	$\tilde{\mu}^N$	$\tilde{e}^N_{\text{RMS}}$	μ_{lin}
3.6214×10^{-3}	3.24×10^{-2}	3.7892×10^{-3}	3.87×10^{-2}	5.9770×10^{-3}
2.3938×10^{-6}	6.00×10^{-2}	2.1421×10^{-6}	6.10×10^{-2}	1.8252×10^{-6}
5.4224×10^{-8}	6.64×10^{-2}	5.4310×10^{-8}	7.08×10^{-2}	4.2072×10^{-8}
5.7578×10^{-10}	1.04×10^{-1}	5.6271×10^{-10}	6.79×10^{-2}	3.8026×10^{-10}

(a) *Synthetic non-linear problem*

$n = 1$		$n = 5$		Linearized
$\tilde{\mu}^N$	$\tilde{e}^N_{\text{RMS}}$	$\tilde{\mu}^N$	$\tilde{e}^N_{\text{RMS}}$	μ_{lin}
4.3626×10^{-3}	2.47×10^{-2}	4.3688×10^{-3}	3.52×10^{-2}	4.5667×10^{-3}
1.1158×10^{-5}	3.91×10^{-2}	1.1278×10^{-5}	4.52×10^{-2}	8.4646×10^{-5}
7.6348×10^{-7}	5.86×10^{-2}	8.0428×10^{-7}	7.76×10^{-2}	3.8022×10^{-6}
3.5977×10^{-10}	9.69×10^{-2}	3.8106×10^{-10}	1.54×10^{-1}	2.6634×10^{-10}

(b) *Autoignition*

$n = 1$		$n = 5$		Linearized
$\tilde{\mu}^N$	$\tilde{e}^N_{\text{RMS}}$	$\tilde{\mu}^N$	$\tilde{e}^N_{\text{RMS}}$	μ_{lin}
2.6422×10^{-3}	5.05×10^{-2}	2.7045×10^{-3}	3.90×10^{-2}	2.2526×10^{-3}
5.6726×10^{-6}	9.44×10^{-2}	5.1764×10^{-6}	4.76×10^{-2}	4.1409×10^{-6}
8.4630×10^{-9}	4.94×10^{-2}	8.6889×10^{-9}	5.58×10^{-2}	8.7048×10^{-9}
8.2730×10^{-10}	4.99×10^{-2}	8.0669×10^{-10}	7.36×10^{-2}	9.1534×10^{-10}

(c) *Elliptic PDE*

Failure cases Here, we report cases which caused BIMC to fail. Figure 2.11 shows MC and BIMC samples for the periodic forward problem. Because $f(\boldsymbol{m})$ has circular contours, the ideal IS density q^* has support over a circular region in $\mathbb{R}^2$. This is also evident from how the samples from q^* are spread. Using a single Gaussian distribution to approximate this complicated density results in a poor fit, and hence, failure of the BIMC method. The nature of the poor fit is noteworthy. The IS density approximates $q^*(\boldsymbol{m})$ well in the direction that is informed by the data. In the directions orthogonal to this data-informed direction, it inherits the covariance of $p(\boldsymbol{m})$, and as such, cannot approximate q^* as it curves around.

Also, notice that the pre-image $f^{-1}(\mathbb{Y})$ is the union of two disconnected regions in parameter space. As a result, the ideal IS density, q^*, has two modes, one near $[1, 1]^\top$, and a weaker one near $[-1, 2.5]^\top$. Which mode is discovered depends on the initial guess provided to the numerical optimization routine. Currently, there exists no robust mechanism in BIMC to discover all the modes of q^*. This is also the cause of failure when the Lorenz system is inverted over $t_f = 5$s.

Another route to failure occurs if the optimal parameters based on an analysis of the linearized inverse problem aren't appropriate for the full non-linear problem. While we don't expect the two to be exactly equal, we implicitly assume that they will be close enough, and serious problems may occur if they're not. For instance, if the pseudo-likelihood variance from the linearized analysis is much smaller than the (unknown) optimal pseudo-likelihood variance for the full non-linear problem, then large IS weights may be observed, leading to biased estimates of the failure probability.

Finally, BIMC can also fail when the solution of the inverse problem cannot be computed. This happens when the Lorenz problem is simulated over a much longer time horizon, $t_f = 15$s. In this case, the optimizer failed to identify a descent direction and converge to a minimum. Physically, this happens because of the chaotic nature of the problem. Since all trajectories of the Lorenz system eventually settle on the attractor, going from a point on

the attractor back in time is a highly ill-conditioned problem.

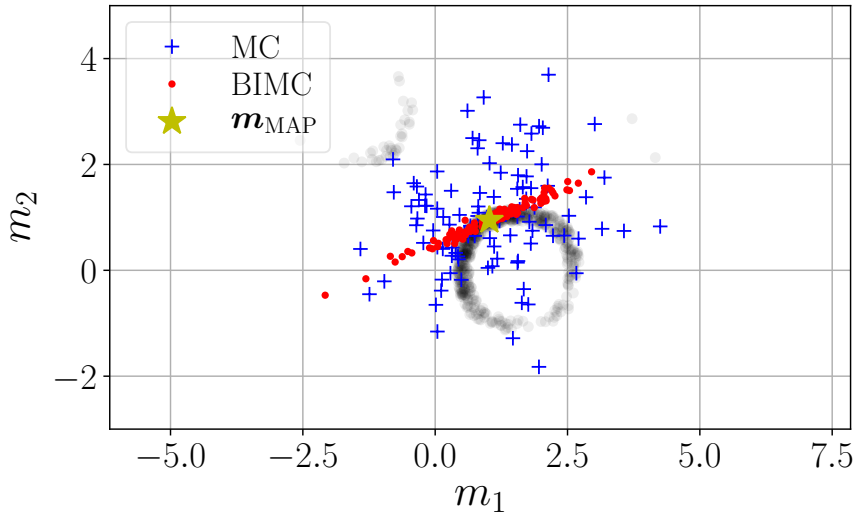

Figure 2.11: *A failure case. Here,* $f(\boldsymbol{m}) = \sin(m_1)\cos(m_2)$ *is a periodic function in* $\mathbb{R}^2$*. Gray markers depict samples from the ideal IS density* q^* *in this case.*

Summary In summary, the effectiveness of BIMC depends on the interplay between the directions *not* informed by the pseudo-data point, and the variation of the forward map in these directions. If, at the scale of the covariance of the nominal density p, $f(\boldsymbol{m})$ varies too quickly in these directions (like the Periodic example), the PDF constructed in BIMC will make for a poor IS density. On the other hand, if $f(\boldsymbol{m})$ varies slowly enough (as in the synthetic non-linear, and autoignition examples) or not at all (the affine case), then BIMC is effective. Thus, we conclude that BIMC is best suited to forward maps that are weakly non-linear at the scale of the covariance of the nominal density p. Physically, this means that the uncertainties in the input parameters must small enough that f appears almost linear. Note that f can still be highly non-linear at larger scales.

Apart from the forward map being only weakly non-linear, there are two additional requirements. The regions in parameter space that evaluate inside $\mathbb{Y}$ should not be disjoint. The

final and perhaps the most important requirement is that the solution of the inverse problem must be computable.

2.5 Conclusion

In this chapter, we addressed the problem of efficiently computing rare-event probabilities in systems with uncertain input parameters. Our approach, called BIMC, employs importance sampling in order to achieve efficiency. Noting the structural similarity between the (theoretical) ideal importance sampling density and the posterior distribution of a fictitious inference problem, our importance sampling distribution is constructed by approximating such a fictitious posterior via a Gaussian distribution. The approximation process allows the incorporation of the derivatives of the input-output map into the importance sampling distribution, which is how our scheme achieves parsimonious sampling. Our theoretical analysis establishes that this procedure is optimal in the setting where the input-output map is affine and the nominal density is Gaussian. Hence, BIMC is best applied to maps that appear nearly affine at the scale of the covariance of the nominal distribution. Our numerical experiments support this conclusion and demonstrate that when this is the case, BIMC can lead to speedups of several orders-of-magnitude. Experiments also reveal several drawbacks in BIMC. We will concern ourselves with fixing these drawbacks in Chapter 3.

Chapter 3

The Adaptive Bayesian Inverse Monte Carlo Method

In Chapter 2 we proposed an importance sampling algorithm to compute rare-event probabilities in forward uncertainty quantification problems. The algorithm, which we termed the *"Bayesian Inverse Monte Carlo (BIMC) method"*, was shown to be optimal for problems in which the input-output operator is nearly affine. But applying the original BIMC to highly nonlinear systems can lead to several different failure modes. In this chapter, we modify the BIMC method to extend its applicability to a wider class of systems. The modified algorithm, which we call *"Adaptive-BIMC (A-BIMC)"*, has two stages. In the first stage, we solve a sequence of optimization problems to roughly identify those regions of parameter space which trigger the rare-event. In the second stage, we use the stage one results to construct a mixture of Gaussians that can be then used in an importance sampling algorithm to estimate rare event probability. We propose using a local surrogate that minimizes costly forward solves. The effectiveness of A-BIMC is demonstrated via several synthetic examples. Yet again, the modified algorithm is prone to failure. We systematically identify conditions under which it fails to lead to an effective importance sampling distribution. One of these conditions is the high ambient dimensionality of the parameter space. To arrest this deterioration in performance, we lay the foundation for a general dimension reduction strategy for rare-event probability estimation.

3.1 Introduction

In Chapter 2, we presented an importance sampling algorithm to address the following goal-oriented uncertainty quantification (UQ) question. Given

- a smooth nonlinear function $f(\boldsymbol{m}) : \mathbb{R}^d \to \mathbb{R}$,
- a probability distribution for its inputs $p(\boldsymbol{m})$, and,
- a target interval $\mathbb{Y} \subset \mathbb{R}$,

what is the probability of the event $f(\boldsymbol{m}) \in \mathbb{Y}$? Our interest was in computing this probability efficiently, i.e., with as few evaluations of f as possible, especially when the event $f(\boldsymbol{m}) \in \mathbb{Y}$ is rare.

The algorithm, called the Bayesian Inverse Monte Carlo (BIMC) method, employed a fictitious Bayesian inverse problem to identify regions of parameter space that evaluate inside $\mathbb{Y}$. BIMC was proven to lead to an optimal IS density for affine f and Gaussian p. As such, when applied to maps f that appear nearly affine at the scale of the covariance of p, BIMC outperformed a simple Monte Carlo method by several orders of magnitude.

We also showed that when this is not the case, that is, when f is significantly nonlinear, BIMC leads to a poor-quality IS distribution. This in turn can lead to inaccurate estimates of the rare-event probability. In this chapter, we propose modifications to BIMC in order to address this major limitation.

Summary of the methodology The modifications result in a two-stage algorithm, which we christen Adaptive-BIMC (A-BIMC). Stage-1 of A-BIMC solves a sequence of optimization problems in order to adaptively explore the input parameter space where $f(\boldsymbol{m}) \in \mathbb{Y}$ (more precisely, this region is the pre-image of $\mathbb{Y}$, defined as the set $\{\boldsymbol{m} \in \mathbb{R}^d : f(\boldsymbol{m}) \in \mathbb{Y}\}$ and

denoted $f^{-1}(\mathbb{Y})$). While BIMC also relies on the solution of an auxiliary, *"fictitious"*, inverse problem, the formulation and interpretation of the optimization problems in Stage-1 of A-BIMC is quite different.

BIMC solves a single optimization problem to arrive at a pseudo-MAP point and then samples around this point to explore the pre-image $f^{-1}(\mathbb{Y})$. By sampling around a single point, BIMC only achieves local exploration of $f^{-1}(\mathbb{Y})$. While this may work for nearly affine maps, such limited exploration is insufficient for more nonlinear problems.

On the other hand, Stage-1 of A-BIMC solves optimization problems in an iterative fashion; the optimization problem in some iteration, aided by specially designed algorithmic components, explores the pre-image $f^{-1}(\mathbb{Y})$ away from regions explored in the preceding iterations. This allows global exploration of $f^{-1}(\mathbb{Y})$. Stage-1 keeps iterating till a termination condition based on user-specified tolerances is met. Then, the local minima so obtained are collected into a Gaussian mixture that roughly approximates the theoretically ideal (zero-error) importance sampling density $q^* \propto \mathbf{1}_{\mathbb{Y}}(f(\boldsymbol{m}))p(\boldsymbol{m})$.

The Gaussian mixture which crudely approximates q^* is refined using the Mixture Population Monte Carlo Algorithm [18]. The MPMC algorithm modifies the mixture weights, means, and covariances of this Gaussian mixture so that it closely approximates the ideal IS density q^*. This, however, requires further evaluations of f, raising the computational cost of the algorithm. In order to circumvent this problem, we replace evaluations of f in q^* with that of a heuristically constructed surrogate of f. Next, we list the contributions and limitations of our approach.

Contributions

- We extend our work in Chapter 2 and propose a novel scheme which adaptively explores the pre-image $f^{-1}(\mathbb{Y})$ on a global scale. In particular, we describe algorithmic

strategies, such as parameter continuation, and a modified penalty algorithm required to achieve this exploration.

- Our scheme employs the derivatives of f to accelerate exploration of the pre-image $f^{-1}(\mathbb{Y})$, as opposed to only pointwise evaluations of f.
- We have attempted to keep tunable algorithmic parameters to a minimum, and as a result, A-BIMC possesses just one user-defined parameter.
- A-BIMC's performance is studied on synthetic problems. Experiments demonstrate that the performance of our method doesn't depend significantly on how small the target probability is. Rather it depends on the nonlinearity of the input-output map.
- We lay the theoretical foundation for dimension reduction in the context of rare-event probability estimation.

Limitations

- A-BIMC is a purely heuristic algorithm. In particular, the algorithmic components chosen preclude its theoretical analysis. Hence, unlike BIMC, it is difficult to *a priori* predict its performance.
- A-BIMC is not without its own failure mechanisms. These are described in Section 3.5, along with strategies for diagnosing and mitigating them.
- While our algorithm possesses only one tunable parameter, we don't have an *a priori* prescription for choosing it. We recommend a default value in Section 3.4 but cannot provide guarantees on whether this value will work or not.
- A-BIMC relies crucially on the MPMC method, which doesn't scale to high-dimensional problems (say, for instance, greater than 64). As a result, A-BIMC is not suitable for

problems with high intrinsic dimension, unless steps are taken to reduce the ambient dimensionality of the problem.

Notation Key notation used in this chapter is summarized in Table 3.1.

Outline of the Chapter In Section 3.2, we briefly review the failure mechanisms of the BIMC method. We describe A-BIMC in detail in Section 3.3. A-BIMC's performance is studied via several numerical experiments in Section 3.4. In Section 3.5, we discuss how A-BIMC can fail, and provide strategies for diagnosing and mitigating failure. Section 3.6 outlines a general strategy for dimension reduction for rare-event probability estimation. We conclude in Section 3.7 and discuss several avenues for future research. Supporting theory and additional results accompanying our numerical experiments are presented in Chapter B.

3.2 Failure of BIMC

To provide context and motivation for developing A-BIMC, we briefly revisit the many failure mechanisms of the BIMC method. The failure modes of BIMC can be categorized broadly into four cases:

- *Curvature of* $f^{-1}(\mathbb{Y})$: Since BIMC results in an optimal approximation of $q^*(\boldsymbol{m})$ in the affine-Gaussian case, it is expected to perform well for input-output maps that are nearly affine. Using BIMC when this is not the case is susceptible to failure, an unsurprising fact; using a single Gaussian distribution, with convex, elliptical contours may prove to be insufficient to cover arbitrary $f^{-1}(\mathbb{Y})$. This phenomenon is captured in Figure 3.1 where $f : \mathbb{R}^2 \to \mathbb{R}$ is defined as $f(\boldsymbol{m}) = \sin(x_1)\cos(x_2)$ and the pre-image $f^{-1}(\mathbb{Y})$ is a circular region in space. In conclusion, this mode of failure occurs when $f(\boldsymbol{m})$ is strongly nonlinear at the scale of the covariance of $p(\boldsymbol{m})$.

Symbols/Acronyms	Meaning
MC	Monte Carlo
IS	Importance Sampling
BIMC	Bayesian Inverse Monte Carlo
A-BIMC	Adaptive Bayesian Inverse Monte Carlo
ESS	Effective Sample Size
MPMC	Mixture Population Monte Carlo
RMS	Root Mean Square
MAP	Maximum *A Posteriori*
f	input-output, or the forward, map
$\boldsymbol{m}$	vector of input parameters to f
$p(\boldsymbol{m})$	input or nominal probability density for $\boldsymbol{m}$
$\mathbb{Y}$	target interval for $f(\boldsymbol{m})$
$\mathbf{1}_{\mathbb{Y}}$	indicator function, $\mathbf{1}_{\mathbb{Y}}(z)$ is 1 if $z \in \mathbb{Y}$, 0 otherwise
$f^{-1}(\mathbb{Y})$	pre-image of the interval $\mathbb{Y}$, $\{\boldsymbol{m} \in \mathbb{R}^d : f(\boldsymbol{m}) \in \mathbb{Y}\}$
d	dimension of $\boldsymbol{m}$
$\mathcal{N}(\boldsymbol{m}_0, \boldsymbol{\Sigma}_0)$	normal distribution with mean $\boldsymbol{m}_0$ and covariance $\boldsymbol{\Sigma}_0$
$\mathbb{P}$	probability of an event
$\mathbb{E}_p$	expectation of a random variable with respect to some density p
$\mathbb{V}_p$	variance of a random variable with respect to some density p
μ	$\mathbb{P}(f(\boldsymbol{m}) \in \mathbb{Y})$, equivalently, $\mathbb{E}_p(\mathbf{1}_{\mathbb{Y}}(f(\boldsymbol{m})))$.
q^*	ideal importance sampling density
Q_k	importance sampling mixture density at the k-th iteration of Stage-1
Q	final importance sampling mixture density
N	number of samples
$\hat{\mu}^N$	MC estimate for μ computed using N samples
$\tilde{\mu}^N$	IS estimate for μ computed using N samples
$\hat{e}^N_{\mathrm{RMS}}$	RMS error in $\hat{\mu}^N$
$\tilde{e}^N_{\mathrm{RMS}}$	RMS error in $\tilde{\mu}^N$
y	pseudo-data
$p(y\|\boldsymbol{m})$	pseudo-likelihood density
$p(\boldsymbol{m}\|y)$	pseudo-posterior density
$\boldsymbol{m}_{\mathrm{MAP}}$	MAP point of $p(\boldsymbol{m}\|y)$
$\mathbf{H}_{\mathrm{MAP}}$	Hessian of $-\log p(\boldsymbol{m}\|y)$ at $\boldsymbol{m}_{\mathrm{MAP}}$
$\mathbf{H}_{\mathrm{GN}}$	Gauss-Newton Hessian of $-\log p(\boldsymbol{m}\|y)$ at some $\boldsymbol{m}$
ϵ_{rel}	relative tolerance for perplexity change across A-BIMC iterations
ϵ_{abs}	absolute tolerance for perplexity change across A-BIMC iterations
$f_{\mathrm{surrogate}}$	cheap-to-evaluate surrogate for f
N_{MPMC}	number of samples used by MPMC
m_{int}	intrinsic dimension of the rare-event problem
$D_{\mathrm{KL}}(p\|\|q)$	Kullback-Leibler (KL) divergence between densities p and q

Table 3.1: *Summary of key notation used in this chapter.*

- *Multiply-connected* $f^{-1}(\mathbb{Y})$: BIMC can also fail if $f^{-1}(\mathbb{Y})$ is the union of disjoint regions in space, which is also evident in Figure 3.1. In this case, q^* has multiple modes whereas a single Gaussian can only capture one. Because the mean of $q(\boldsymbol{m})$ is found using numerical optimization, which mode is found depends on the initial guess provided to the numerical optimization routine.

- *Poor selection of tunable parameters*: Yet another failure mode occurs when the optimal tunable parameters that result from linearizing f aren't appropriate for the full nonlinear problem. As Equation (2.11) reveals, the covariance of $q(\boldsymbol{m})$ is a rank-1 non-positive definite update of the covariance of $p(\boldsymbol{m})$. The degree of this update is inversely proportional to σ^2. If the optimal likelihood variance, σ^2, for the linearized problem is much smaller than the optimal likelihood variance for the full nonlinear problem, the covariance update will be needlessly large, and consequently, $q(\boldsymbol{m})$ will not have enough support to cover $f^{-1}(\mathbb{Y})$. This can cause large IS ratios, and at small to moderate sample sizes, biased estimates for the rare event probability.

- *Intractable inverse problem*: It may be the case that the optimization problem formulated to compute $\boldsymbol{m}_{\text{MAP}}$ is highly ill-conditioned and non-convex, making $\boldsymbol{m}_{\text{MAP}}$ inaccessible via standard numerical optimization routines. Since the BIMC methodology is crucially dependent on successfully computing $\boldsymbol{m}_{\text{MAP}}$, we declare failure if the numerical optimization routine employed fails at its task.

This concludes our recap of the limitations of the BIMC method. The next section develops the Adaptive-BIMC (A-BIMC) methodology in detail.

3.3 Methodology

A-BIMC is a heuristic algorithm designed to address the drawbacks in BIMC. Perhaps the most crippling drawback of BIMC is its inability to conform to disconnected or curved $f^{-1}(\mathbb{Y})$.

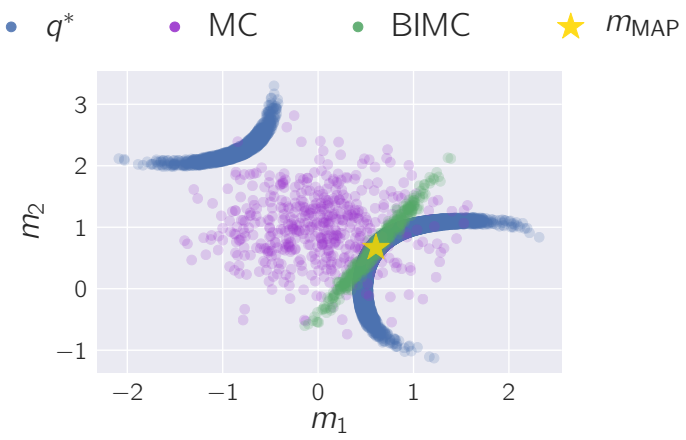

Figure 3.1: *A single Gaussian distribution fails to cover curved and/or disjoint* $f^{-1}(\mathbb{Y})$ *when* $f(\boldsymbol{m}) = \sin(m_1)\cos(m_2)$. *Shown are 5000 samples from* q^* *and 500 MC and BIMC samples.*

A-BIMC attempts to improve the performance of BIMC in this regime by constructing a mixture of Gaussians for importance sampling. Gaussian mixtures are a class of probability distributions of the form $Q(\boldsymbol{m}) = \sum_{k=1}^{K} \alpha_k \mathcal{N}(\boldsymbol{m}_k, \boldsymbol{\Sigma}_k)$, $\sum_k \alpha_k = 1$, and are sufficiently rich to simulate complicated phenomena. Constructing a suitable IS density in the Gaussian mixture context amounts to identifying the mean $\boldsymbol{m}_k$, covariance $\boldsymbol{\Sigma}_k$, and mixture weight α_k of each component. The algorithm does so in two stages, both of which proceed iteratively. Stage-1 enriches the IS mixture with a new component at every iteration, till the algorithm is satisfied that no more components are required in the mixture. The aim of this stage is to arrive at a mixture distribution that roughly approximates $q^*(\boldsymbol{m})$. Stage-2 tunes the mixture that results at the end of Stage-1 using the Mixture Population Monte Carlo algorithm [18] so that it forms a better approximation of q^*. Tuning the IS mixture in this manner also removes the effect of any poorly selected parameters, such as σ^2 or y. The following subsections describe each stage in more detail.

3.3.1 Stage-1

As mentioned previously, this stage constructs a crude approximation of q^* by adding a new component to the IS mixture at every iteration. To establish notation, the IS mixture at the k-th iteration of this stage is denoted by Q_k. Since each iteration in Stage-1 adds a new component to the IS mixture, Q_k always has k components. The i-th component of Q_k is denoted by q_i. Further, the concept of a fictitious inverse problem (including its components: the pseudo-prior, pseudo-likelihood, and pseudo-posterior) introduced in Section 2.3 is re-used here.

First, the mixture is initialized using the BIMC procedure to $Q_1 = \mathcal{N}(\boldsymbol{m}_{\text{MAP}}, \boldsymbol{\Sigma}_{\text{MAP}})$. For $k = 2, 3, \ldots$, the algorithm adds a new component $\mathcal{N}(\boldsymbol{m}_k, \boldsymbol{\Sigma}_k)$ to Q_{k-1} with some weight α_k. The center $\boldsymbol{m}_k$ of every new component is found by solving an optimization problem. The covariance $\boldsymbol{\Sigma}_k$ and weight α_k are evaluated heuristically, but still depend on $\boldsymbol{m}_k$. The number of components in the mixture grows till a termination condition based on user-specified tolerances is satisfied. Sections 3.3.1.1 and 3.3.1.2 respectively describe how $\boldsymbol{\Sigma}_k$ and α_k are chosen once $\boldsymbol{m}_k$ is known. Section 3.3.1.3 describes how the center $\boldsymbol{m}_k$ of a new component is chosen in the first place, and the condition that terminates this stage of A-BIMC.

3.3.1.1 Tuning covariance

Suppose a new component of the Gaussian mixture, denoted q_k, is to be placed at $\boldsymbol{m}_k$. Then, for its covariance $\boldsymbol{\Sigma}_k$, we choose the inverse of the Gauss-Newton Hessian matrix of the pseudo-posterior $-\log p(\boldsymbol{m}|y)$ at $\boldsymbol{m}_k$. This way $\mathcal{N}(\boldsymbol{m}_k, \boldsymbol{\Sigma}_k)$ crudely approximates q^* around $\boldsymbol{m}_k$. The inverse of the Gauss-Newton Hessian, and hence $\boldsymbol{\Sigma}_k$ is given by:

$$\begin{aligned}\mathbf{H}_{\mathrm{GN}}^{-1} &= \left(\frac{\nabla f(\boldsymbol{m}_k)\nabla f(\boldsymbol{m}_k)^T}{\sigma^2} + \boldsymbol{\Sigma}_0^{-1}\right)^{-1} \\ &= \boldsymbol{\Sigma}_0 - \frac{1}{\sigma^2 + \nabla f(\boldsymbol{m}_k)^T \boldsymbol{\Sigma}_0 \nabla f(\boldsymbol{m}_k)} \left(\boldsymbol{\Sigma}_0 \nabla f(\boldsymbol{m}_k)\right)\left(\boldsymbol{\Sigma}_0 \nabla f(\boldsymbol{m}_k)\right)^T,\end{aligned} \tag{3.1}$$

and again an appropriate value for σ remains is unknown. As in BIMC, this covariance matrix is parameterized by σ^2, the variance of the pseudo-likelihood density. Note that unlike BIMC, $\mathcal{N}(\boldsymbol{m}_k, \boldsymbol{\Sigma}_k)$ isn't dependent on y, the pseudo-data point: BIMC's dependence on y arose out of $\boldsymbol{m}_{\mathrm{MAP}}$'s dependence on y. Now, however, the center of this new component is fixed at $\boldsymbol{m}_k$, severing its y-dependence. As a result, the procedure for selecting σ^2 is slightly different in this case. A-BIMC selects that value of σ^2 which minimizes the Kullback-Leibler divergence between the linearized pushforwards of q^* and q_k.

Suppose $f^{\mathrm{lin}}(\cdot) = \nabla f(\boldsymbol{m}_k)^T(\cdot - \boldsymbol{m}_k) + f(\boldsymbol{m}_k)$ is the linearized approximation of f at $\boldsymbol{m}_k$ and$q_\sharp^*$ and $q_{k,\sharp}$ are the pushforward densities of q^* and q_k under f^{lin}. Then, the algorithm selects $\sigma_k^* = \arg\min D_{\mathrm{KL}}(q_\sharp^* || q_{k,\sharp})$ for constructing $\mathbf{H}_{\mathrm{GN}}^{-1}$. The reason for resorting to the KL divergence between linearized pushforwards is that an analytical expression for $D_{\mathrm{KL}}(q^*||q_k)$ is difficult to obtain even in the affine-Gaussian case, let alone for arbitrary f. On the other hand, $q_\sharp^*$ and $q_{k,\sharp}$ being univariate densities, both $D_{\mathrm{KL}}(q_\sharp^*||q_{k,\sharp})$ and σ_k^* have analytical expressions (provided in Equations (B.5) and (B.6)).

3.3.1.2 Identifying weights

Whenever a new component $q_k = \mathcal{N}(\boldsymbol{m}_k, \boldsymbol{\Sigma}_k)$ is added to the IS mixture, A-BIMC readjusts the weight of all components in the IS mixture so that they satisfy following rule:

$$\alpha_i \propto \int q_i(\boldsymbol{m}) p(\boldsymbol{m}) \mathrm{d}\boldsymbol{m}, \tag{3.2}$$

where q_i is the i-th component of Q_k. This heuristic for the mixture weights α_i is motivated by the knowledge that components in regions where $p(\boldsymbol{m})$ is large should dominate in the resultant IS mixture. If $p(\boldsymbol{m})$ is a Gaussian, then the integrals in Equation (3.2) can be evaluated analytically.

3.3.1.3 Identifying centers

The center of the first component in the mixture, $\boldsymbol{m}_1$, is always fixed to be the $\boldsymbol{m}_{\text{MAP}}$, the MAP point of the pseudo-posterior $p(\boldsymbol{m}|y)$. Now, suppose that at the beginning of some iteration k, the IS mixture has $k-1$ components whose centers are at $\boldsymbol{m}_1, \boldsymbol{m}_2, \ldots, \boldsymbol{m}_{k-1}$. Identifying the center of a new component, denoted $\boldsymbol{m}_k$, is a delicate balancing act. It must

1. not be extremely close to an existing center $\boldsymbol{m}_1, \ldots, \boldsymbol{m}_{k-1}$, as this makes $\boldsymbol{m}_k$ redundant, wasting time and effort spent in discovering it,

2. be in regions that correspond to high probability mass under $p(\boldsymbol{m})$ so that the mixture resembles $q^*(\boldsymbol{m})$, but this requirement can conflict with the previous one, and,

3. must lie inside $f^{-1}(\mathbb{Y})$ to maintain efficiency.

A-BIMC constructs an optimization problem whose cost functional mathematically captures these requirements. The solution of the optimization problem should then be a suitable location to place $\boldsymbol{m}_k$, as it represents the best compromise between the potentially conflicting requirements. Requirement 1 is represented mathematically by defining a fictitious repulsive force between $\{\boldsymbol{m}_1, \boldsymbol{m}_2, \ldots, \boldsymbol{m}_{k-1}\}$ and $\boldsymbol{m}_k$. This repulsive force defines a fictitious potential energy, $\mathcal{U}(\boldsymbol{m}_k)$, that becomes the first term in the cost functional of this optimization problem. Requirement 2 is met by leveraging $p(\boldsymbol{m})$ to define an attractive potential, $\mathcal{P}(\boldsymbol{m}_k)$, which becomes the second term in the cost functional. And the third requirement is enforced by adding the constraint $f(\boldsymbol{m}_k) \in \mathbb{Y}$.

The repulsive force is defined by imagining like-charged particles placed at $\{\boldsymbol{m}_1, \ldots, \boldsymbol{m}_{k-1}\}$ and $\boldsymbol{m}_k$. The charges at $\{\boldsymbol{m}_1, \boldsymbol{m}_2, \ldots, \boldsymbol{m}_{k-1}\}$ are considered stationary, while the charge at $\boldsymbol{m}_k$ is allowed to move. Then, the electrostatic repulsion between $\boldsymbol{m}_k$ and $\{\boldsymbol{m}_1, \ldots, \boldsymbol{m}_{k-1}\}$ forces $\boldsymbol{m}_k$ away from the latter. Note that it is possible to enrich the set $\{\boldsymbol{m}_1, \ldots, \boldsymbol{m}_{k-1}\}$ with more (stationary) particles at locations where it is undesirable for a new component to be placed. Henceforth, the set of undesirable locations for $\boldsymbol{m}_k$ will be denoted $\boldsymbol{\chi}^{(k)}_{\text{fixed}} = \{\boldsymbol{m}^{(i)}_{\text{fixed}}, i = 1, \ldots, n_{\text{fixed}}\}$. The set $\boldsymbol{\chi}^{(k)}_{\text{fixed}}$ always contains the existing particle centers, $\boldsymbol{m}_1, \ldots, \boldsymbol{m}_k \subseteq \boldsymbol{\chi}^{(k)}_{\text{fixed}}$, but is allowed to contain any other locations discovered by the algorithm (how $\boldsymbol{\chi}^{(k)}_{\text{fixed}}$ is modified is described in a later section).

Since $\boldsymbol{m}^{(1)}_{\text{fixed}}, \ldots, \boldsymbol{m}^{(n_{\text{fixed}})}_{\text{fixed}}$ are fixed, the electrostatic potential energy, $\mathcal{U}$, only varies with $\boldsymbol{m}_k$, and the contribution to potential energy due to the pairwise interactions of the members of $\boldsymbol{\chi}^{(k)}_{\text{fixed}}$ remains a constant. Subsequently, $\mathcal{U}$ is expressed only as a function of $\boldsymbol{m}_k$ and the constant potential energy due to $\boldsymbol{m}^{(1)}_{\text{fixed}}, \ldots, \boldsymbol{m}^{(n_{\text{fixed}})}_{\text{fixed}}$ is omitted.

$$\mathcal{U}(\boldsymbol{m}_k) = \sum_{i=1}^{n_{\text{fixed}}} \frac{1}{\|\boldsymbol{m}_k - \boldsymbol{m}^{(i)}_{\text{fixed}}\|}$$

The attractive potential $\mathcal{P}(\boldsymbol{m})$ of a particle at some location $\boldsymbol{m}$ is set to be $-\beta \log p(\boldsymbol{m})$, where β is a scale factor. Thus, the total attractive potential energy due to this "pseudo-prior" potential energy is $\mathcal{P}(\boldsymbol{\chi}_{\text{fixed}}, \boldsymbol{m}_k) = -\log p(\boldsymbol{m}_k) - \beta \sum_{i=1}^{n_{\text{fixed}}} - \log p(\boldsymbol{m}^{(i)}_{\text{fixed}})$. Again, the constant contribution to $\mathcal{P}(\boldsymbol{\chi}_{\text{fixed}}, \boldsymbol{m}_k)$ by the n_{fixed} fixed charges is ignored and the pseudo-prior potential energy is expressed only as $\mathcal{P}(\boldsymbol{m}_k) = -\beta \log(\boldsymbol{m}_k)$. Hence, the total potential energy of the system as a function of the center of the prospective k-th component is:

$$\mathcal{J}(\boldsymbol{m}_k) = \mathcal{U}(\boldsymbol{m}_k) + \mathcal{P}(\boldsymbol{m}_k)$$

Now, $\boldsymbol{m}_k$ can be found by minimizing the potential energy of the system provided the minima lies in the pre-image of the target interval $\mathbb{Y}$. This third requirement is met by adding the constraint $y_k = f(\boldsymbol{m}_k)$, where $y_k \sim \mathbb{U}(\mathbb{Y})$ is randomly chosen from $\mathbb{Y}$ with uniform probability. Thus, the following optimization problem is formulated:

$$\begin{aligned} \boldsymbol{m}_k = \underset{\boldsymbol{m}\in\mathbb{R}^d}{\arg\min} \sum_{i=1}^{n_{\text{fixed}}} \frac{1}{\|\boldsymbol{m} - \boldsymbol{m}_{\text{fixed}}^{(i)}\|} - \beta \log p(\boldsymbol{m}) \\ \text{s.t. } y_k = f(\boldsymbol{m}_k) \end{aligned} \tag{3.3}$$

The scale parameter β controls the relative tradeoff between the repulsive and the attractive potentials, and consequently, the spacing between $\boldsymbol{m}_k$ and the fixed centers $\boldsymbol{m}_{\text{fixed}}^{(1)}, \ldots, \boldsymbol{m}_{\text{fixed}}^{(n_{\text{fixed}})}$. To see this, imagine that the system contains a single fixed charge at $\boldsymbol{m}_1$, and the optimization problem in Equation (3.3) has been set up to find an appropriate location for a new Gaussian component, whose center will be at $\boldsymbol{m}_2$ (see Figure 3.2 for an illustration). If β is very small, then the total potential energy will be dominated by electrostatic repulsion and the minimizer of $\mathcal{J}(\boldsymbol{m}_2)$ will be far away from $\boldsymbol{m}_1$, possibly where $p(\boldsymbol{m}_2)$ is small. On the other hand, if β is large, then the pseudo-prior potential energy will dominate and the minimizer will be close to the nearest local minimum of $p(\boldsymbol{m})$, preventing exploration of $f^{-1}(\mathbb{Y})$ away from $\boldsymbol{m}_1$. Both these situations are undesirable, and hence, β must be chosen suitably. However, a suitable value of β isn't known *a priori*. To ensure a spacing that's appropriate for the purposes of importance sampling, A-BIMC employs a continuation scheme to implicitly fix β, which is described next.

Parameter continuation The basic idea behind the continuation scheme in A-BIMC is the following. The scheme tries several values of β to minimize Equation (3.3), creates prospective IS mixtures corresponding to each minimizer, and then selects one that is most appropriate (in a sense that will be made precise shortly).

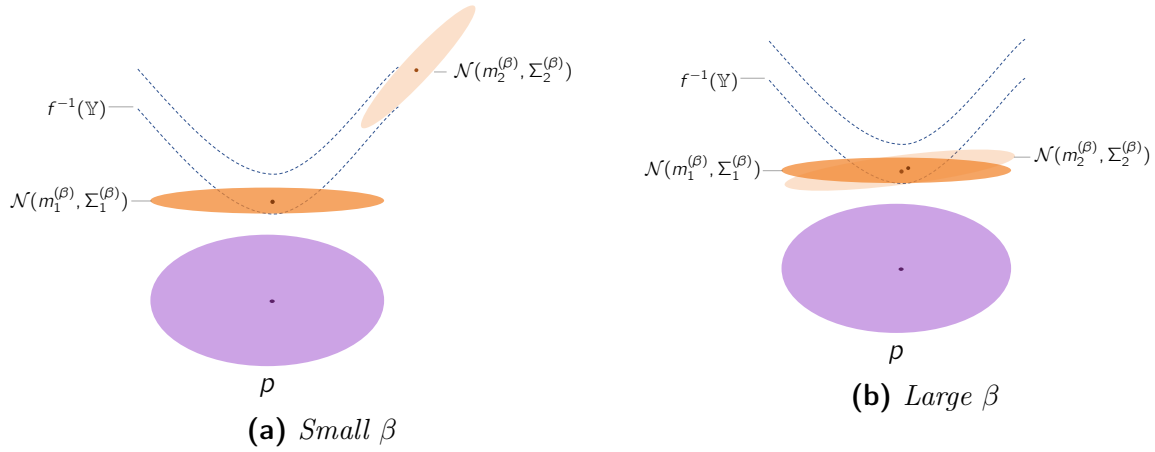

(a) *Small* β **(b)** *Large* β

Figure 3.2: *Illustration of the effect of the scale parameter* β*. A small value of* β *leads to the new component with center* $\boldsymbol{m}_2$ *being placed far away from* $p(\boldsymbol{m})$*. On the other hand, if* β *is too large, then the new component center will be undesirably close to* $\boldsymbol{m}_1$*. The continuation procedure described in Algorithm 2 is designed to yield an intermediate value of* β *that avoids both extremes.*

At the beginning of Stage-1, the minimum and maximum values for β, $\beta_{\min}$ and $\beta_{\max}$, are computed by studying the relative magnitudes of $\mathcal{U}(\boldsymbol{m})$ and $\mathcal{P}(\boldsymbol{m})$. Then, the scheme tries five different values of β, logarithmically spaced between $\beta_{\min}$ and $\beta_{\max}$, starting at $\beta_{\min}$. Each value of β leads to a solution of the optimization problem in Equation (3.3), say $\boldsymbol{m}_k^{(\beta)}$. Through Equations (3.1) and (3.2) each minimizer $\boldsymbol{m}_k^{(\beta)}$ is in turn associated with a new prospective component $\mathcal{N}(\boldsymbol{m}_k^{(\beta)}, \boldsymbol{\Sigma}_k^{(\beta)})$, which can be added to the IS mixture with weight $\alpha_k^{(\beta)}$ leading to a prospective IS mixture, say $Q_k^{(\beta)}$. To decide whether $Q_k^{(\beta)}$ is suitable or not, the scheme computes a sample estimate of the KL divergence $D_{\mathrm{KL}}(Q_{k-1}||Q_k^{(\beta)})$ between the current IS mixture Q_{k-1} and $Q_k^{(\beta)}$. The scheme tries larger and larger values of β as long as $D_{\mathrm{KL}}(Q_{k-1}||Q_k^{(\beta)})$ increases with β. If from one iteration to the next, $D_{\mathrm{KL}}(Q_{k-1}||Q_k^{(\beta)})$ decreases, the scheme stops and appends the prospective mixture $Q_k^{(\beta)}$ from the previous iteration. Hence, implicitly, the scheme selects that value of β which makes the resulting IS mixture most different from the current one.

As there's no guarantee that the minimizer at a given β, $\boldsymbol{m}_k^{(\beta)}$, will get accepted, Equa-

tion (3.3) is solved inexactly for each value of β. Further, the minimizer at some β, $\boldsymbol{m}_k^{(\beta)}$, is supplied as the initial guess for solving Equation (3.3) at the next value of β. Each $\boldsymbol{m}_k^{(\beta)}$ is also added to the set of fixed charges, $\boldsymbol{\chi}_{\text{fixed}}$, ensuring that any future center is placed away from all $\boldsymbol{m}_k^{(\beta)}$, in addition to the center that was finally appended to the IS mixture. This prevents A-BIMC from exploring regions that it has previously explored and forces it to venture into previously unexplored regions.

The next paragraph describes how Equation (3.3) is solved at a given value of β.

Solving the constrained optimization problem For a given value of β, the nonlinearly constrained optimization is solved as follows. First, Equation (3.3) is transformed to an unconstrained optimization problem via the Augmented Lagrangian (AL) method. In the AL method, the equality constraint is enforced by augmenting the Lagrangian with a term that penalizes violation of the constraint. For Equation (3.3), choosing a quadratic penalty term yields the following objective function:

$$\mathcal{L}(\boldsymbol{m}) = \mathcal{U}(\boldsymbol{m}) + \mathcal{P}(\boldsymbol{m}) + \frac{1}{2\delta}\left(y - f(\boldsymbol{m})\right)^2 - \lambda\left(y - f(\boldsymbol{m})\right) \tag{3.4}$$

In a traditional implementation of the AL algorithm, the constraint is enforced by solving a sequence of optimization problems where the coefficient of the penalty term, $1/\delta$ and the Lagrange multiplier term, λ are modified simultaneously. Eventually, the minimizer of the unconstrained Augmented Lagrangian converges to the minimizer of the constrained optimization problem (see [59] for a basic implementation of this algorithm). Although A-BIMC adopts the AL approach, for the purposes of IS, enforcing $y = f(\boldsymbol{m})$ exactly is unnecessary. It suffices if $f(\boldsymbol{m}) \in \mathbb{Y}$. Starting from some initial guess for δ and λ, δ_0, λ_0, the algorithm adopts the iterative approach only if the corresponding minimizer, $\boldsymbol{m}^*$, does not evaluate inside $\mathbb{Y}$. The moment $f(\boldsymbol{m}^*) \in \mathbb{Y}$, the AL iterations are terminated.

Procedure 2 CONTINUATION

Input: current IS mixture Q_{k-1}, set of fixed charges $\boldsymbol{\chi}_{\text{fixed}}$, set of values for the continuation parameter $B = \{\beta_1, \beta_2, \ldots, \beta_{|B|}\}$, initial guess for the quadratic penalty parameter δ_{start}, initial guess for the Lagrange multiplier λ_{start}, constraint value y,

Output: IS mixture enriched with a new component Q_k, new fixed charges discovered $\boldsymbol{\chi}_{\text{new}}$, sample estimate of $D_{\text{KL}}(Q_{k-1}||Q_k)$

$\boldsymbol{\chi}_{\text{new}} \leftarrow \varnothing$
Choose $\boldsymbol{m}_{\text{start}} \in \mathbb{R}^d$
for $1 \leq j \leq |B|$ **do**
    Using $\delta_{\text{start}}, \lambda_{\text{start}}, \boldsymbol{m}_{\text{start}}$ as starting guesses for $\delta, \lambda, \boldsymbol{m}$, $\beta = \beta_j$ and $\boldsymbol{\chi}_{\text{fixed}}$ as the set of fixed charges, follow algorithm 3 to minimize Equation (3.3)
    $\boldsymbol{m}_{\text{new}} \leftarrow$ MODIFIEDAUGMENTEDLAGRANGIAN$(y, \mathbb{Y}, \lambda_{\text{start}}, \delta_{\text{start}}, \boldsymbol{m}_{\text{start}})$
    Using $\boldsymbol{m} = \boldsymbol{m}_{\text{new}}$ in Equation (B.6) compute a suitable value of the pseudo-likelihood variance σ_{new}
    Using $\boldsymbol{m} = \boldsymbol{m}_{\text{new}}, \sigma = \sigma_{\text{new}}$ in Equation (3.1), compute $\mathbf{H}_{\text{GN}}^{-1}$ and assign it to $\boldsymbol{\Sigma}_{\text{new}}$
    Obtain a prospective IS distribution $Q_k^{(\beta_j)}$ by adding $\mathcal{N}(\boldsymbol{m}_{\text{new}}, \boldsymbol{\Sigma}_{\text{new}})$ to Q_{k-1}
    $\boldsymbol{m}_{\text{start}} \leftarrow \boldsymbol{m}_{\text{new}}$
    $\boldsymbol{\chi}_{\text{new}} \leftarrow \boldsymbol{\chi}_{\text{new}} \cup \{\boldsymbol{m}_{\text{new}}\}$
    Compute a sample estimate of $D_{\text{KL}}(Q_{k-1}||Q_k^{(\beta_j)})$ and assign it to $\hat{D}_{\text{KL}}[j]$
    if $\hat{D}_{\text{KL}}[j] > \hat{D}_{\text{KL}}[j-1]$ **then**
        Try a larger value of β
        continue
    else
        $Q_k^{(\beta_{j-1})}$ *was more different from* Q_{k-1} *than* $Q_k^{(\beta_j)}$
        $Q_k \leftarrow Q_k^{(\beta_{j-1})}$
        return $(Q_k, \boldsymbol{\chi}_{\text{new}}, \hat{D}_{\text{KL}}[j-1])$
    end if
end for
$\hat{D}_{\text{KL}}(Q_{k-1}||Q_k^{(\beta_j)})$ *increases with* j*, hence* $Q_k^{(\beta_{|B|})}$ *is most different from* Q_{k-1}
$Q_k \leftarrow Q_k^{(\beta_{|B|})}$
return $(Q_k, \boldsymbol{\chi}_{\text{new}}, \hat{D}_{\text{KL}}[|B|])$

Procedure 3 ModifiedAugmentedLagrangian

Input: desired constraint value y, target interval $\mathbb{Y}$, starting guess for Lagrange multiplier λ_{start}, starting guess for penalty coefficient δ_{start}, starting guess for the optimizer $\boldsymbol{m}_{\text{start}}$

Output: Approximate minimizer of Equation (3.3) $\boldsymbol{m}^*$

$\delta \leftarrow \delta_{\text{start}}$
$\lambda \leftarrow \lambda_{\text{start}}$
$\boldsymbol{m}^* \leftarrow \boldsymbol{m}_{\text{start}}$
while $f(\boldsymbol{m}^*) \notin \mathbb{Y}$ **do**
    Starting from $\boldsymbol{m}_{\text{start}}$, compute the approximate minimizer of $\mathcal{L}(\cdot; \delta, \lambda)$ and assign it to $\boldsymbol{m}^*$
    $\lambda \leftarrow \lambda - \frac{1}{\delta}\left(y - f(\boldsymbol{m}^*)\right)$
    $\delta \leftarrow 0.5\delta$
    $\boldsymbol{m}_{\text{start}} \leftarrow \boldsymbol{m}^*$
end while
return $\boldsymbol{m}^*$

This concludes the description of how A-BIMC finds centers of new components. The continuation and modified Augmented Lagrangian algorithms described above are reproduced in pseudo-code in Algorithms 2 and 3. The next subsection describes the termination criterion employed in Stage-1.

3.3.1.4 Termination

The procedure described above adds new components to the IS mixture in every iteration. Hence, the number of components in the mixture grows steadily. In order to decide whether the IS mixture is sufficiently stable, or conversely, if more components are required, the algorithm keeps track of how the IS mixture changes across iterations. The change in the IS mixture is measured in terms of a quantity that resembles perplexity, $\zeta = \exp(-D_{\text{KL}}(Q_{k-1}||Q_k))$, where Q_k is the IS mixture at the k-th iteration. Since $D_{\text{KL}}\left(Q_{k-1}||Q_k\right) \geq 0$, $\zeta \in (0, 1]$. The KL divergence here is once again a sample estimate, and is in fact the same quantity computed in the continuation scheme. Stage-1 is terminated if relative change in ζ falls below a user specified relative change threshold, or its absolute value exceeds a user-specified absolute change threshold.

3.3.1.5 Summary

In summary, Stage-1 adaptively explores the pre-image of the interval $f^{-1}(\mathbb{Y})$, and yields an IS distribution with the following form:

$$Q(\boldsymbol{m}) = \sum_{k=1}^{K} \alpha_k \mathcal{N}\left(\boldsymbol{m}_k, \boldsymbol{\Sigma}_k\right). \tag{3.5}$$

The centers of the Gaussian mixture components are obtained by solving a sequence of optimization problems, the weights α_k are heuristically evaluated, and the covariances $\boldsymbol{\Sigma}_k$ are local Gauss-Newton Hessians. This procedure is heuristic, with no guarantees on the quality of the final Gaussian mixture for importance sampling. Hence, Stage-2 of A-BIMC further modifies the Gaussian mixture that results at the end of Stage-1. Details of Stage-2 are provided next.

3.3.2 Stage-2

Stage-2 of A-BIMC modifies the Gaussian mixture obtained at the end of Stage-1 via the Mixture Population Monte Carlo algorithm. This subsection begins with a brief introduction to the MPMC algorithm, before describing how it's employed within A-BIMC.

3.3.2.1 Mixture Population Monte Carlo method

The MPMC algorithm generates an importance sampling distribution to approximate some target distribution π using the following approach. Among all possible Gaussian mixtures with K components, it seeks that mixture Q^* which is closest in KL divergence to π:

$$Q^* = \underset{Q \in \mathcal{Q}_K}{\arg\min}\, D_{KL}(\pi || Q), \tag{3.6}$$

where $\mathcal{Q}_K$ denotes the family of K-component Gaussian mixtures. Here, K is assumed to be known and fixed. Importance sampling is then performed using Q^*.

Seeking Q^* is equivalent to seeking its K mixture weights $(\omega_1^*, \ldots, \omega_K^*)$ and the means $\boldsymbol{m}_k^*$ and covariances $\mathbf{C}_k^*$ of its components. Equation (3.6) can be restated as:

$$(\omega_1^*, \ldots, \omega_K^*, \boldsymbol{m}_1^*, \ldots, \boldsymbol{m}_K^*, \mathbf{C}_1^*, \ldots, \mathbf{C}_K^*) = \underset{\substack{\sum_k \omega_k = 1 \\ \mathbf{C}_k \succ \mathbf{0} \\ \boldsymbol{m}_k \in \mathbb{R}^d}}{\arg\min} D_{\mathrm{KL}} \left(\pi || \sum_k \omega_k \mathcal{N}(\boldsymbol{m}_k, \mathbf{C}_k) \right), \tag{3.7}$$

which, from the definition of KL divergence, is equivalent to

$$(\omega_1^*, \ldots, \omega_K^*, \boldsymbol{m}_1^*, \ldots, \boldsymbol{m}_K^*, \mathbf{C}_1^*, \ldots, \mathbf{C}_K^*) = \underset{\substack{\sum_k \omega_k = 1 \\ \mathbf{C}_k \succ \mathbf{0} \\ \boldsymbol{m}_i \in \mathbb{R}^d}}{\arg\max} \int \pi(\boldsymbol{m}) \log \left(\sum_k \omega_k \mathcal{N}(\boldsymbol{m}_k, \mathbf{C}_k) \right) \mathrm{d}\boldsymbol{m}. \tag{3.8}$$

Here, the notation $\mathbf{C}_k \succ \mathbf{0}$ implies that $\mathbf{C}_k$ is positive definite. The constraints $\sum_k \omega_k = 1$ and $\mathbf{C}_k \succ \mathbf{0}$ are necessary for Q^* to remain a valid Gaussian mixture.

The optimization problem in Equation (3.8) strongly resembles maximum likelihood estimation of the mixture parameters, for which the Expectation Maximization (EM) algorithm [28] is usually employed. As a result, MPMC also closely follows the EM algorithm, except that the sum over i.i.d. data is replaced with an integration over $\pi(\boldsymbol{m})$. Like EM, MPMC is an iterative algorithm. Starting from some initial mixture, the mixture weights, and the means and covariances of its components are updated in every iteration. The update expressions involve evaluating expectations with respect to π. These integrals are in turn evaluated using autonormalized importance sampling, and hence, the algorithm only requires the ability to evaluate $\pi(\boldsymbol{m})$ up to a constant.

Procedure 4 FORWARDSURROGATE

Input: input-output map $f(\cdot)$, set of fixed charges $\boldsymbol{\chi}_{\text{fixed}}$, query location $\boldsymbol{m}$
Output: A surrogate $f_{\text{surrogate}}(\boldsymbol{m})$ for $f(\boldsymbol{m})$
1: Find that member of $\boldsymbol{\chi}_{\text{fixed}}$ to which $\boldsymbol{m}$ is closest and assign it to $\boldsymbol{m}_{\text{min}}$
2: $f_{\text{surrogate}}(\boldsymbol{m}) \leftarrow f(\boldsymbol{m}_{\text{min}}) + \nabla f(\boldsymbol{m}_{\text{min}})^T(\boldsymbol{m} - \boldsymbol{m}_{\text{min}}) + 0.5(\boldsymbol{m} - \boldsymbol{m}_{\text{min}})^T \nabla^2 f(\boldsymbol{m}_{\text{min}})(\boldsymbol{m} - \boldsymbol{m}_{\text{min}})$
3: **return** $f_{\text{surrogate}}(\boldsymbol{m})$

The progress of the algorithm is tracked by measuring the normalized perplexity of the IS weights used in computing the update integrals. The algorithm is terminated when, at some iteration, the normalized perplexity stagnates, or becomes sufficiently close to 1. The Gaussian mixture obtained at the end of this iterative procedure is then used for importance sampling of π. The next subsection describes how MPMC is used within A-BIMC.

3.3.2.2 MPMC and A-BIMC

As the mixture obtained at the end of Stage-1, Q_K, only roughly approximates q^*, it is further refined using the MPMC algorithm. One way to do this could be to set the target distribution π to q^*, and supplying Q_K as the initial guess to the algorithm. However, this would require additional evaluations of f, driving up the computational cost of the method. A-BIMC instead constructs a cheap surrogate for f, denoted $f_{\text{surrogate}}$, and then sets $\pi(\boldsymbol{m}) = 1_{\mathbb{Y}}(f_{\text{surrogate}}(\boldsymbol{m}))p(\boldsymbol{m})$ in order to tune Q_K. The surrogate $f_{\text{surrogate}}$ is constructed as follows.

During the continuation phase in Stage-1, A-BIMC saves $(f(\boldsymbol{m}^i_{\text{fixed}}), \nabla f(\boldsymbol{m}^i_{\text{fixed}}), \nabla^2 f(\boldsymbol{m}^i_{\text{fixed}}))$ at each fixed charge $\boldsymbol{m}^i_{\text{fixed}}$. These three quantities can be used to construct a second-order Taylor series expansion around each fixed charge $\boldsymbol{m}^i_{\text{fixed}}$. In order to approximate $f(\boldsymbol{m})$ at some $\boldsymbol{m}$, the surrogate first finds the fixed charged in $\boldsymbol{\chi}_{\text{fixed}}$ which is closest in Euclidean distance to $\boldsymbol{m}$, let's say $\boldsymbol{m}_{\text{min}}$. Then, $f(\boldsymbol{m})$ is approximated as: $f(\boldsymbol{m}_{\text{min}}) + \nabla_{\boldsymbol{m}} f(\boldsymbol{m}_{\text{min}})^T(\boldsymbol{m} - \boldsymbol{m}_{\text{min}}) + 0.5(\boldsymbol{m} - \boldsymbol{m}_{\text{min}})^T \nabla^2_{\boldsymbol{m}} f(\boldsymbol{m}_{\text{min}})(\boldsymbol{m} - \boldsymbol{m}_{\text{min}})$. Pseudo-code for this procedure is provided in Algorithm 4.

The surrogate constructed here is merely a suggestion. If a better, more principled surrogate is available, then that may be used in constructing the target distribution π in MPMC. Irrespective of how the surrogate is constructed, it is only used while tuning Q_K via MPMC and nowhere else. The actual function f is used for the final importance sampling stage. This concludes the presentation of the A-BIMC methodology. The next subsection offers a summary of our algorithm.

3.3.3 Summary

In summary, our algorithm involves the following steps:

- *Constructing the IS distribution*: First, the importance sampling distribution is constructed. This itself is a two stage process. In Stage-1, a sequence of optimization problems is solved to adaptively discover $f^{-1}(\mathbb{Y})$. The resulting sequence of local minima are consolidated into a Gaussian mixture using heuristic estimates of the covariance and mixture weights. Stage-2 involves tuning the Gaussian mixture that results from the first stage against $q^*(\boldsymbol{m})$ via MPMC. This involves evaluations of $q^*(\boldsymbol{m})$, which in turn requires evaluations of $f(\boldsymbol{m})$. While tuning with MPMC, a cheap surrogate for f is used, in order to keep function evaluations low. For simplicity, we will denote the importance sampling mixture at the end of this two stage procedure using just Q.

- *Sampling the IS distribution*: Finally, the mixture that is obtained at the end of the previous stage is used as an importance sampling density to evaluate the rare-event probability. In this step, A-BIMC uses true evaluations of $f(\boldsymbol{m})$, instead of any surrogates.

Pseudo-code for the A-BIMC methodology is provided in Algorithm 5.

Procedure 5 AdaptiveBIMC

Input: input-output map $f(\cdot)$, target interval $\mathbb{Y}$, mean $\boldsymbol{m}_0$ and covariance $\boldsymbol{\Sigma}_0$ of $p(\boldsymbol{m})$, absolute and relative tolerances ϵ_{abs} and ϵ_{rel}, number of samples N

Output: importance sampling estimate of the rare event probability $\tilde{\mu}^N$, the associated relative root mean square error $\tilde{e}^N_{\text{RMS}}$

Construct the IS distribution

Stage-1

Find $\boldsymbol{m}_{\text{start}}$ such that $f(\boldsymbol{m}_{\text{start}}) \in \mathbb{Y}$

Linearize $f(\boldsymbol{m})$ around $\boldsymbol{m}_{\text{start}}$, and use this linearized approximation in Equation (2.21) to compute the optimum pseudo-likelihood variance σ^{*2} and optimum pseudo-data y^*

Construct the pseudo-posterior $p(\boldsymbol{m}|y)$ using $y = y^*$ and $\sigma = \sigma^*$ and compute its MAP point, assign it to $\boldsymbol{m}_{\text{MAP}}$

Using $\boldsymbol{m} = \boldsymbol{m}_{\text{MAP}}, \sigma = \sigma^*$ in Equation (3.1), compute $\mathbf{H}^{-1}_{\text{GN}}$ and assign it to $\boldsymbol{\Sigma}_{\text{MAP}}$

$Q_1 \leftarrow \mathcal{N}(\boldsymbol{m}_{\text{MAP}}, \boldsymbol{\Sigma}_{\text{MAP}})$

$\boldsymbol{\chi}_{\text{fixed}} \leftarrow \{\boldsymbol{m}_{\text{MAP}}\}$

Choose initial guess for the Lagrange multiplier $\lambda_{\text{start}} \in \mathbb{R}$

Choose initial guess for the penalty $\delta_{\text{start}} \in \mathbb{R}^+$

Choose values for the scale parameter $B \leftarrow \{\beta_1, \beta_2, \ldots, \beta_{|B|}\}$.

for $k = 2, 3, \ldots$ **do**

  Sample y uniformly from $\mathbb{Y}$

  Add a new component to Q_{k-1} using Algorithm 2. As a side effect, obtain $\hat{D}_{\text{KL}}(Q_{k-1}||Q_k)$ and $\boldsymbol{\chi}_{\text{new}}$ $(Q_k, \boldsymbol{\chi}_{\text{new}}, \hat{D}_{\text{KL}}) \leftarrow \textsc{Continuation}(Q_{k-1}, \delta_{\text{start}}, \lambda_{\text{start}}, y, \boldsymbol{\chi}_{\text{fixed}}, B)$

  $\boldsymbol{\chi}_{\text{fixed}} \leftarrow \boldsymbol{\chi}_{\text{fixed}} \cup \boldsymbol{\chi}_{\text{new}}$

  $\zeta[k] \leftarrow \exp(-\hat{D}_{\text{KL}}(Q_{k-1}||Q_k))$

  if $\zeta[k] > \epsilon_{\text{abs}}$ **or** $|\zeta[k] - \zeta[k-1]|/\zeta[k] < \epsilon_{\text{rel}}$ **then** break

  end if

end for

Assume Stage-1 required K iterations. Denote the mixture obtained Q_K.

Stage-2

Using $\boldsymbol{\chi} = \boldsymbol{\chi}_{\text{fixed}}$, employ Algorithm 4 to construct a surrogate $f_{\text{surrogate}}$ for f.

Define $q^*_{\text{surrogate}} \propto \mathbf{1}_{\mathbb{Y}}(f_{\text{surrogate}})p$.

Tune the IS mixture Q_K to match $q^*_{\text{surrogate}}$ using the MPMC algorithm, and assign the tuned mixture to Q

Compute the rare event probability

Generate N samples from the tuned mixture $\boldsymbol{X}_1, \ldots, \boldsymbol{X}_N \overset{\text{i.i.d.}}{\sim} Q$

$w_i \leftarrow \frac{\mathbf{1}_{\mathbb{Y}}(f(\boldsymbol{X}_i))p(\boldsymbol{X}_i)}{Q(\boldsymbol{X}_i)}, i = 1, \ldots, N$

$\tilde{\mu}^N \leftarrow \frac{1}{N}\sum_i w_i$

$\tilde{e}^N_{\text{RMS}} \leftarrow \sqrt{\sum_i (w_i - \tilde{\mu}^N)^2}/N\tilde{\mu}^N$

return $\tilde{\mu}^N, \tilde{e}^N_{\text{RMS}}$

3.4 Experiments

This section presents results from a variety of numerical experiments. These experiments have been designed to assess how A-BIMC performs, expose the conditions that affect its performance, and in the process, unearth any potential limitations. To provide a context in which the results can be understood, the following remarks are in order.

Measuring performance Objectively assessing the performance of an IS scheme solely from samples is still an unresolved question. Appealing to Chebyshev's inequality [88] reveals a simple (but potentially restrictive) criterion: a low relative RMSE is sufficient for $\tilde{\mu}^N$ to be close to μ with high probability. As a diagnostic quantity, the relative RMSE also appears in disguise elsewhere; for instance, as the χ^2-divergence between q^* and Q in [2, 78], the Effective Sample Size [2, 63, 78] or the second moment of the IS weights [2]. These studies have established the central role that the relative RMSE and its variants play in controlling the error between $\tilde{\mu}^N$ and μ. For this reason, A-BIMC's performance is primarily measured in terms of the relative RMSE. Since the true relative RMSE is unavailable, it is approximated via samples. Let $\boldsymbol{M}_1, \ldots, \boldsymbol{M}_N \overset{i.i.d.}{\sim} Q(\boldsymbol{m})$ be N samples from Q. The relative RMSE, defined in Equation (4) in Part I, can be estimated via samples as follows:

$$\tilde{e}^N_{\text{RMS}} = \sqrt{\frac{\sum_i w_i^2}{(\sum_i w_i)^2} - \frac{1}{N}}$$

where $w_i = \mathbf{1}_{\mathbb{Y}}(f(\boldsymbol{M}_i))p(\boldsymbol{M}_i)/Q(\boldsymbol{M}_i)$. The sample estimate of the relative RMSE has been shown to be an inadequate indicator of performance in [19]. However, in the large N asymptotic regime, $\tilde{e}^N_{\text{RMS}}$ approximates e_{RMS} well, and therefore $\tilde{e}_{\text{RMS}}$ and its variants are expected to perform adequately as diagnostics [2]. In addition to the sample estimate of the relative RMSE, the ESS is also reported. Taking inspiration from the the function-specific ESS defined in [63], the following rare-event specific ESS is employed:

$$\text{ESS} = \frac{1}{\sum_i \bar{w}_i^2},$$

where $\bar{w}_i = \mathbf{1}_{\mathbb{Y}}(f(\boldsymbol{m}_i))p(\boldsymbol{m}_i)/Q(\boldsymbol{m}_i)/\sum_j \mathbf{1}_{\mathbb{Y}}(f(\boldsymbol{m}_j))p(\boldsymbol{m}_j)/Q(\boldsymbol{m}_j)$. Section B.2 establishes that there exists a one-to-one correspondence between $\tilde{e}^N_{\text{RMS}}$ and the rare-event specific ESS. Hence, the ESS is only reported for a few representative experiments.

Measuring function evaluations Along with performance estimates, the number of function evaluations required during Stage-1 of A-BIMC are also reported. Recall that Stage-1 solves a sequence of optimization problems to iteratively explore $f^{-1}(\mathbb{Y})$. Here, it is assumed that A-BIMC has access to an oracle who, when queried, returns $f(\boldsymbol{m}), \nabla f(\boldsymbol{m})$ and $\nabla^2 f(\boldsymbol{m})$ at some $\boldsymbol{m}$. The function evaluations reported correspond to the number of queries that Stage-1 made to this oracle. It is further assumed that the cost of evaluating the surrogate $f_{\text{surrogate}}$ during Stage-2 is negligible, and is not reported.

Forward maps As proof-of-concept, the toy periodic map presented in Section 3.2 is revisited. In addition, A-BIMC is tested on synthetic maps drawn from the following classes of functions. Maps that belong to these classes are sufficiently rich to expose both the advantages and drawbacks of A-BIMC. The manner in which these maps are actually constructed is detailed while describing the setup for each experiment. The function classes are:

- Quadratic polynomials: The class of functions $f : \mathbb{R}^d \to \mathbb{R}$ of the form: $f(\boldsymbol{m}) = \boldsymbol{m}^T\mathbf{H}\boldsymbol{m} + \boldsymbol{b}^T\boldsymbol{m} + c$ for some $\mathbf{H} \in \mathbb{R}^{d\times d}$, $\boldsymbol{b} \in \mathbb{R}^d$ and $c \in \mathbb{R}$. In other words, f is nonlinear but with constant curvature. Note that for this class of functions, $f = f_{\text{surrogate}}$.
- Cubic polynomials: The class of functions $f : \mathbb{R}^d \to \mathbb{R}$ of the form: $f(\boldsymbol{m}) = \boldsymbol{\mathcal{S}} : \boldsymbol{\mathcal{M}} + \boldsymbol{m}^T\mathbf{H}\boldsymbol{m} + \boldsymbol{b}^T\boldsymbol{m} + c$ for some $\boldsymbol{\mathcal{S}} \in \mathbb{R}^{d\times d\times d}$, $\mathbf{H} \in \mathbb{R}^{d\times d}$, $\boldsymbol{b} \in \mathbb{R}^d$ and $c \in \mathbb{R}$ and

where the tensor contraction $\boldsymbol{\mathcal{S}} : \boldsymbol{\mathcal{M}}$ is defined as $\boldsymbol{\mathcal{S}} : \boldsymbol{\mathcal{M}} = \mathcal{S}_{ijk} m_i m_j m_k$. Now, f is nonlinear and again possesses varying curvature since $\nabla^2 f(\boldsymbol{m})$ varies with $\boldsymbol{m}$.

Implementation A-BIMC has been implemented in MATLAB. The optimization problems posed in Section 3.3.1.3 are solved using the Trust Region algorithm, as implemented in MATLAB's in-built `fminunc` routine. In the implementation, the gradients and the Hessian of the objective function are passed to the optimizer. Because each individual optimization problem the continuation phase of Stage-1 does not need to be solved exactly, the optimizer is terminated if the gradient is reduced by a factor of 10^{-2} or if the number of iterations exceeds 5.

Algorithmic parameters Unless otherwise noted, A-BIMC is run using the following parameters: $\epsilon_{\text{abs}} = 1 - 10^{-3}$ and $\epsilon_{\text{rel}} = 10^{-3}$. For Stage-2, the specific variant of MPMC used is termed the Rao-Blackwellized version in [18]. By default, MPMC uses $N_{\text{MPMC}} = 10^6$ samples per iteration and a maximum of 50 iterations.

The following subsections present the results of numerical experiments. The first experiment is a proof-of-concept that establishes whether all of BIMC's drawbacks have been rectified. The next experiment subjects A-BIMC to problems of increasing dimensionality. This is followed by a study of its performance as the rarity of the problem is increased.

3.4.1 A toy problem

Purpose This is a proof-of-concept experiment whose aim is to establish that A-BIMC leads to a consistent importance sampling distribution and that all of the drawbacks listed in Section 3.2 have been fixed.

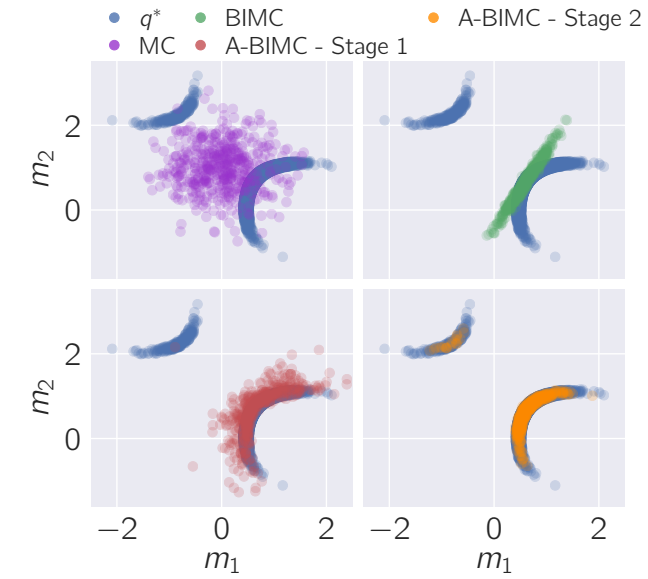

(a) *Samples*

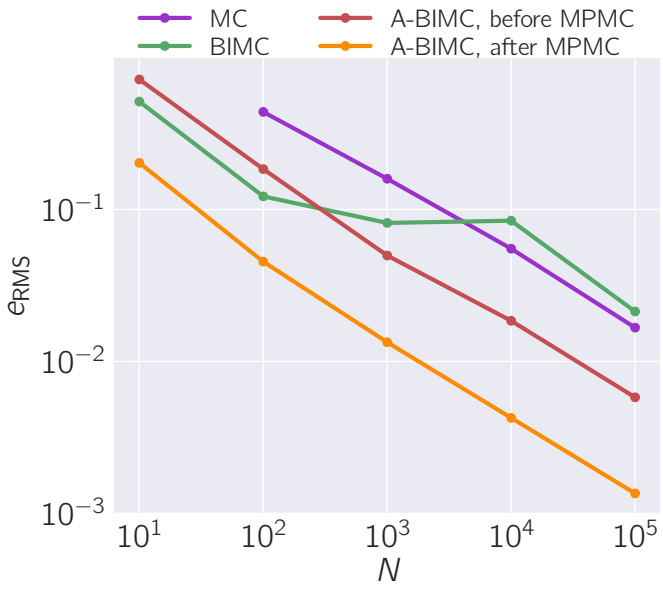

(b) *Relative RMSE versus number of samples N*

Figure 3.3: *A comparison of simple Monte Carlo, BIMC, and the various stages of A-BIMC using the toy problem - samples (Figure 3.3a) and relative error (Figure 3.3b). Figure 3.3a shows 5000 samples from q^* and 500 from each estimator. While the IS mixture at the end of Stage-1 of A-BIMC is an improvement over BIMC, tuning via MPMC drastically improves its quality.*

Setup As noted earlier, for this toy problem, the forward map is defined as $f(\boldsymbol{m}) := \sin(m_1)\cos(m_2)$. The nominal distribution is $p(\boldsymbol{m}) = \mathcal{N}(\boldsymbol{m}_0, \boldsymbol{\Sigma}_0)$ where $\boldsymbol{m}_0 = [0, 1]^T$ and $\boldsymbol{\Sigma}_0 = 0.3\mathbf{I}_2$. A Monte Carlo simulation using 10^6 samples results in the following 99% confidence interval: $3.413 \times 10^{-2} \pm 4.68 \times 10^{-4}$.

Results and discussion Figure 3.3 compares the quality of various estimators – MC, BIMC, and A-BIMC at the end of Stages 1 and 2, in terms of the quality of samples and the relative RMSE. As is evident, Stage-1 yields a mixture that roughly approximates q^*. This mixture contains 46 components. MPMC takes this rough approximation of q^* and and tunes it so that it better resembles q^*. Also noteworthy is the fact that at the end of Stage-1, A-BIMC finds the successfully finds the secondary mode of q^*, albeit with an insufficient mixture weight, a discrepancy which is fixed by MPMC. The total number of function evaluations required by A-BIMC was 3051.

3.4.2 Effect of dimensionality

Purpose Importance sampling schemes are known to suffer from the curse of dimensionality. This experiment investigates how increasing the dimensionality of the rare-event probability estimation problem affects A-BIMC's performance.

Setup To obtain a complete understanding of A-BIMC's performance, two different notions of dimensionality are varied. The first notion of dimensionality is the ambient dimension of the problem, which is simply the dimension of the space in which the uncertain parameters live. Therefore, if $\boldsymbol{m} \in \mathbb{R}^d$, then the ambient dimension of the problem is d. The second notion of dimension is that of the intrinsic dimension d_{int} of the problem. The intrinsic dimension of the posed rare-event probability estimation problem is defined to be the dimension of the subspace in which the ideal importance sampling distribution q^* differs from

the nominal distribution p. Such a situation can arise, for instance, if the forward map f is sensitive only to a few directions in the input parameter space. This definition of intrinsic dimension for rare-events closely follows that for Bayesian inference, where it is taken to be the dimension of the subspace where the posterior differs from the prior [26, 86].

Given the ambient dimension d, the intrinsic dimension of the problem is specified as follows. First, p is set to $p = \mathcal{N}(\mathbf{1}_d, \mathbf{I}_d)$, where $\mathbf{1}_d = [1, 1, \dots 1]^T \in \mathbb{R}^d$ is the vector of all 1's and $\mathbf{I}_d$ is the $d \times d$ identity matrix. Then forward maps $f(\boldsymbol{m})$ are constructed so that they satisfy $\partial f / \partial m_i = 0$ for $i = d_{\text{int}} + 1, \dots, d$. This way, the maps are insensitive to any variation of the input parameters in $\text{span}\{\boldsymbol{e}_{d_{\text{int}}+1}, \dots, \boldsymbol{e}_d\}$, where $\boldsymbol{e}_i$ is the i-th canonical basis vector. In addition, since p is a Normal distribution with identity covariance, q^* differs from p only in $\text{span}\{\boldsymbol{e}_1, \dots, \boldsymbol{e}_{d_{\text{int}}}\}$. In $\text{span}\{\boldsymbol{e}_{d_{\text{int}+1}}, \dots, \boldsymbol{e}_d\}$, q^* is identical to p by construction.

As for actually constructing $\boldsymbol{\mathcal{S}}, \mathbf{H}, \boldsymbol{b}$, the following procedure is adopted. Given d_{int} and d, we set (in MATLAB notation) $\boldsymbol{\mathcal{S}}[d_{\text{int}}+1 : d, d_{\text{int}}+1 : d, d_{\text{int}}+1 : d] = \mathbf{0}$, $\mathbf{H}[d_{\text{int}}+1 : d, d_{\text{int}}+1 : d] = \mathbf{0}$ and $\boldsymbol{b}[d_{\text{int}} + 1 : d] = \mathbf{0}$. Now, let $\bar{\boldsymbol{\mathcal{S}}}$, $\bar{\mathbf{H}}$ and $\bar{\boldsymbol{b}}$ denote the non-zero blocks of $\boldsymbol{\mathcal{S}}$, $\mathbf{H}$, and $\boldsymbol{b}$, i.e., $\boldsymbol{\mathcal{S}}[1 : d_{\text{int}}, 1 : d_{\text{int}}, 1 : d_{\text{int}}], \mathbf{H}[1 : d_{\text{int}}, 1 : d_{\text{int}}], \boldsymbol{b}[1 : d_{\text{int}}]$. These are constructed as follows.

The tensor $\bar{\boldsymbol{\mathcal{S}}}$ is constructed as: $\bar{\boldsymbol{\mathcal{S}}} = 10\boldsymbol{\mathcal{I}} + \boldsymbol{\mathcal{G}}$. Here $\boldsymbol{\mathcal{I}}$ is defined as $\boldsymbol{\mathcal{I}}_{ijk} := \boldsymbol{\delta}_{ij}\mathbf{1}_k$, $\boldsymbol{\delta}_{ij}$ is the Kronecker delta, and $\mathbf{1}_k$ assumes the value 1 for all possible k. The tensor $\boldsymbol{\mathcal{G}}$ is a tensor of i.i.d. standard Normal variables, $\boldsymbol{\mathcal{G}}_{ijk} \sim \mathcal{N}(0, 1)$. The matrix $\bar{\mathbf{H}}$ is constructed as a sample from a Wishart distribution with scale matrix $2\mathbf{I}_{d_{\text{int}}}$ and $d_{\text{int}} + 1$ degrees of freedom, $\bar{\mathbf{H}} \sim W(2\mathbf{I}_{d_{\text{int}}}, d_{\text{int}} + 1)$. The vector $\bar{\boldsymbol{b}}$ is a vector of uniformly distributed random numbers in $[0, 1]$, $\bar{\boldsymbol{b}}_i \sim \mathbb{U}([0, 1])$.

The ambient dimension d is set to $16, 32, 64$, and for d, the intrinsic dimension d_{int} is varied from a minimum of $d_{\text{int}} = 4$ to a maximum of $d_{\text{int}} = d$.

Results and discussion Figures 3.4 and 3.5 reports the relative RMSE obtained. Stage-1 of A-BIMC only yields consistent estimates of the rare-event probability at low d_{int}. At large d_{int}, the error after Stage-1 fails to exhibit the expected $1/\sqrt{N}$ convergence. Stage-2 of A-BIMC appears weakly dependent on the intrinsic dimension of the problem. Notably, it consistently leads to low errors. For instance, achieving a relative RMSE of around 10% only requires $N = 100$ samples. Exceptions to this trend is the cubic case at $d_{\text{int}} = 4$ and $d = 16$ and $d_{\text{int}} = 64, d = 64$.

The poor performance at $d_{\text{int}} = 4$ and $d = 64$ (this case is referred to as F1 subsequently) can be attributed to the surrogate $f_{\text{surrogate}}$ not possessing sufficient accuracy. The poor performance at $d_{\text{int}} = d = 64$ (referred to as F2 subsequently) is due to the relatively higher ambient dimensionality of the problem, which causes MPMC to result in mixtures whose components have rank-deficient covariance matrices. These limitations, as well as a measures to diagnose and fix them, are discussed in Section 3.5.

Figure 3.6 reports the number of function evaluations required by Stage-1 of A-BIMC. The function evaluations display no significant trend with either ambient, or the intrinsic dimension of the problem. Tables 3.2 and 3.3 reports the best and worst observed normalized-ESS, ESS/N for each ambient dimension at $N = 10^4$. The normalized-ESS reflects the poorly performing cases noted earlier ($\{d_{\text{int}} = 4, d = 16\}$ and $\{d_{\text{int}} = 64, d = 64\}$.

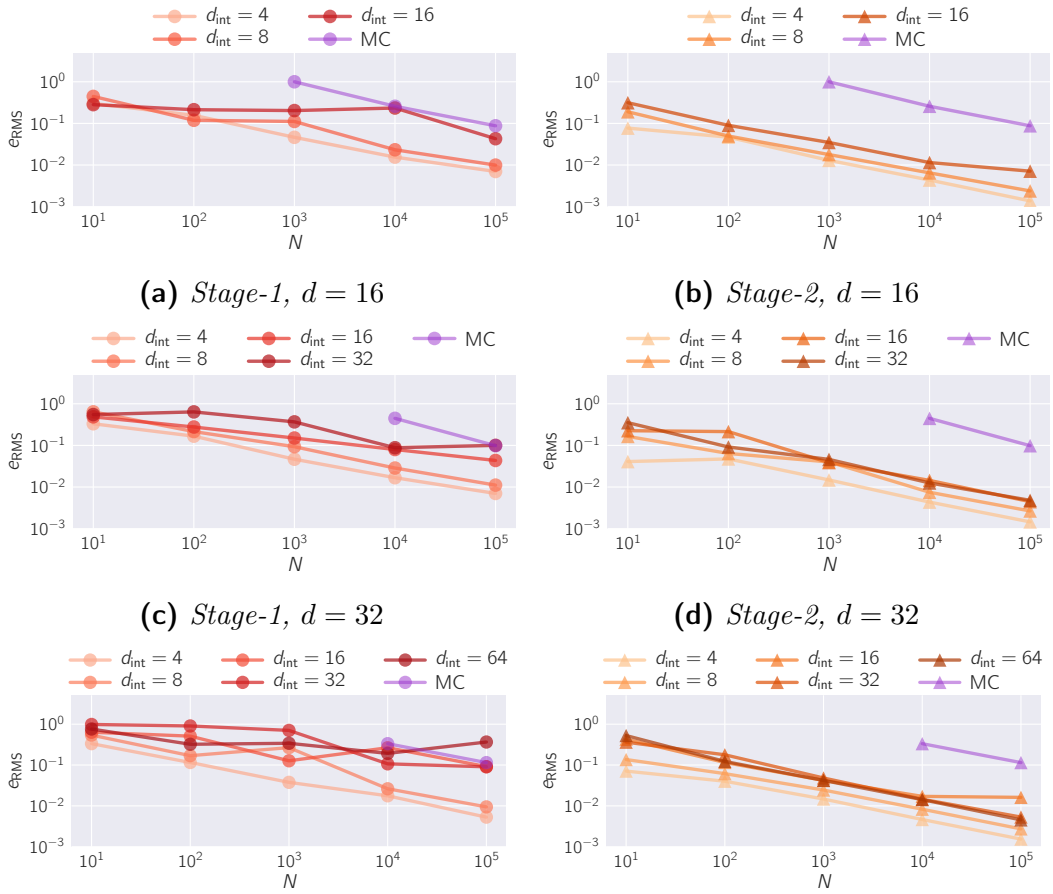

(a) *Stage-1*, $d = 16$ **(b)** *Stage-2*, $d = 16$

(c) *Stage-1*, $d = 32$ **(d)** *Stage-2*, $d = 32$

(e) *Stage-1*, $d = 64$ **(f)** *Stage-2*, $d = 64$

Figure 3.4: *Convergence of the relative RMSE,* e_{RMS}*, with number of samples* N *at various combinations of* d *and* d_{int} *for the quadratic problem.*

d	Worst ESS (corresponding d_{int})	Best ESS (corresponding d_{int})
16	0.43 (16)	0.84 (4)
32	0.32 (16)	0.84 (4)
64	0.25 (16)	0.82 (4)

Table 3.2: *Worst and best observed normalized-ESS at various ambient dimension* d *for the quadratic problem. The normalized-ESS is reported at* $N = 10^4$*. The values in parentheses indicate the intrinsic dimension* d_{int} *at which the normalized-ESS was observed.*

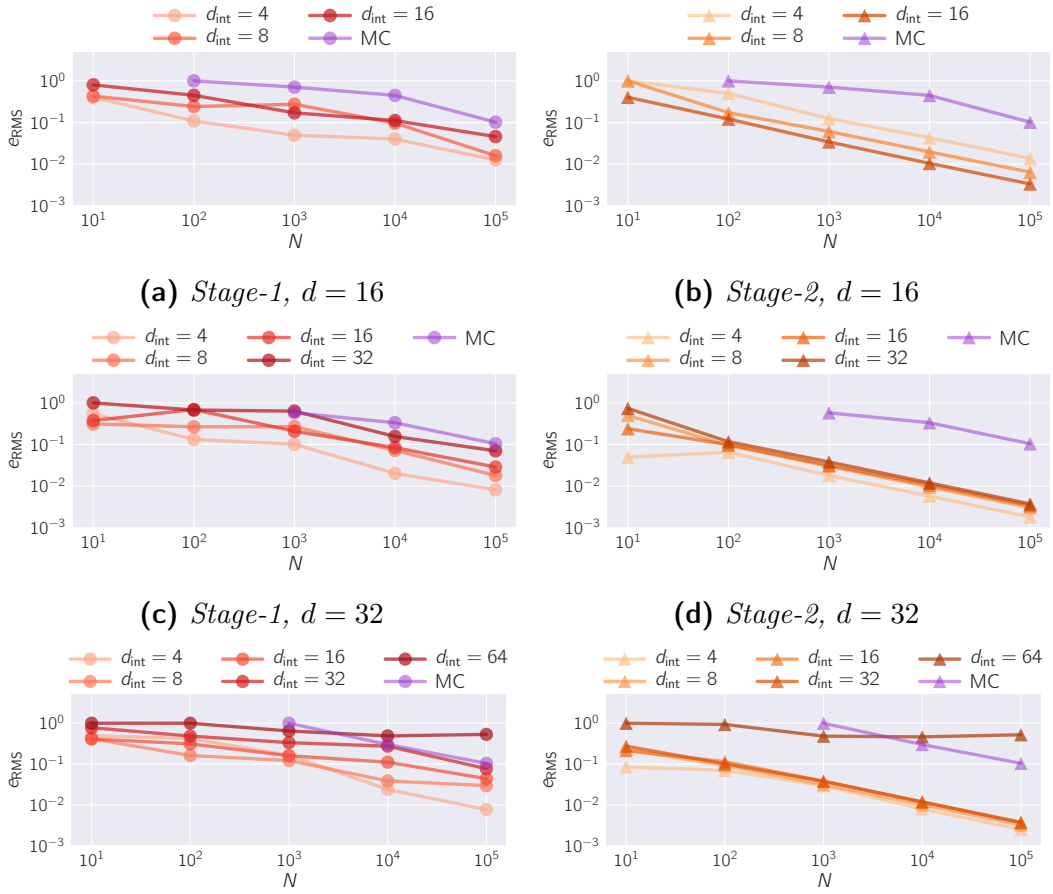

(a) *Stage-1*, $d = 16$ **(b)** *Stage-2*, $d = 16$

(c) *Stage-1*, $d = 32$ **(d)** *Stage-2*, $d = 32$

(e) *Stage-1*, $d = 64$ **(f)** *Stage-2*, $d = 64$

Figure 3.5: *Convergence of the relative RMSE,* e_{RMS}*, with number of samples* N *at various combinations of* d *and* d_{int} *for the cubic problem.*

d	Worst ESS (corresponding d_{int})	Best ESS (corresponding d_{int})
16	0.051 (4)	0.48 (16)
32	0.41 (32)	0.75 (32)
64	0.00046 (64)	0.61 (4)

Table 3.3: *Worst and best observed normalized-ESS at various ambient dimension* d *for the cubic problem. The normalized-ESS is reported at* $N = 10^4$*. The values in parentheses indicate the intrinsic dimension* d_{int} *at which the normalized-ESS was observed.*

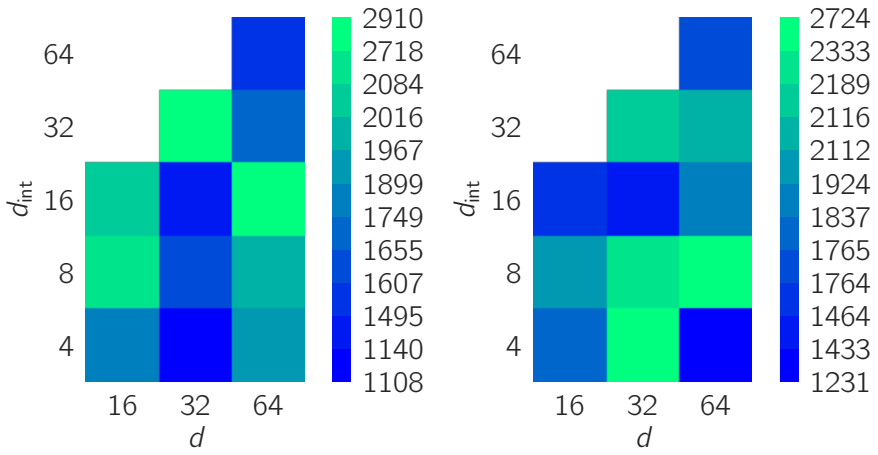

(a) *Quadratic problem* **(b)** *Cubic problem*

Figure 3.6: *Function evaluations required by Stage-1 of A-BIMC display no significant trend with either d or d_{int}.*

3.4.3 Effect of rarity

Purpose This experiment is designed to answer the following question: how does A-BIMC perform as the magnitude of the rare-event probability is decreased?

Setup Both the quadratic and cubic forward maps are constructed as in Section 3.4.2 but the dimensionality of the problem is fixed at $d = 16$ and $d_{\text{int}} = 8$ so that the effect of decreasing probability level can be extracted. The nominal distribution for both forward maps is also as in Section 3.4.2, $p(\boldsymbol{m}) = \mathcal{N}(\mathbf{1}_d, \boldsymbol{I}_d)$. The rarity level is increased by choosing $\mathbb{Y}$ so that the rare-event probability is approximately $\mathcal{O}(10^{-4}), \mathcal{O}(10^{-5}), \mathcal{O}(10^{-6})$ respectively for each forward map.

Results and discussion As was demonstrated in Section 2.2, the number of samples required by a simple Monte Carlo method to achieve a specified accuracy in the rare-event probability increases as the probability decreases. Figure 3.7 offers evidence that this is

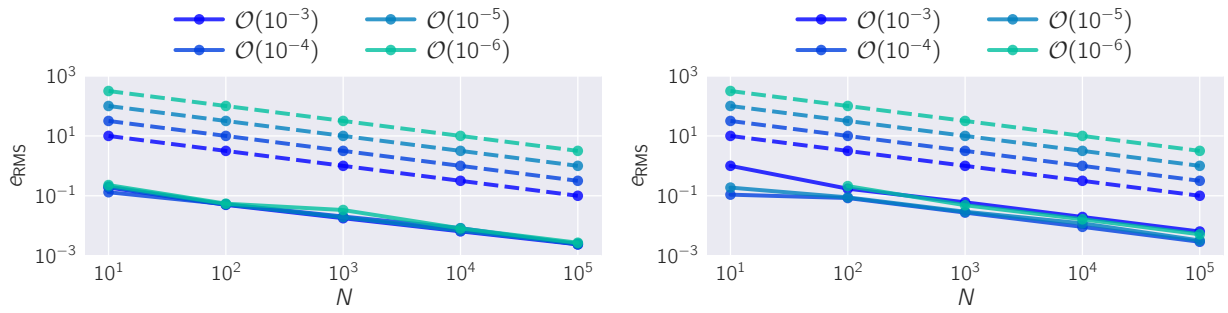

(a) *Quadratic problem* **(b)** *Cubic problem*

Figure 3.7: *This figure demonstrates that A-BIMC (solid lines) performs consistently well even as the magnitude of the rare-event probability is decreased from $\mathcal{O}(10^{-3})$ to $\mathcal{O}(10^{-6})$. The dashed lines show the expected theoretical performance of the simple Monte Carlo estimator $\hat{\mu}$, computed using the expression $\sqrt{(1-\hat{\mu})/(\hat{\mu}N)}$ (see Section 2.2).*

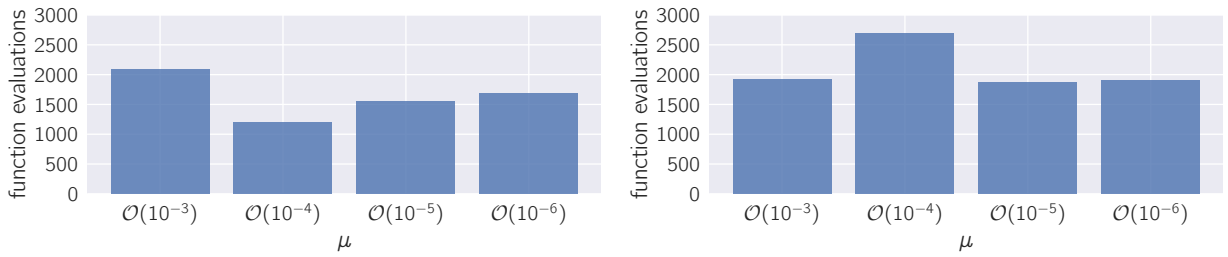

(a) *Quadratic problem* **(b)** *Cubic problem*

Figure 3.8: *Function evaluations required by A-BIMC remain independent of the magnitude of the rare-event probability, as this probability is decreased from $\mathcal{O}(10^{-3})$ down to $\mathcal{O}(10^{-6})$.*

not the case for A-BIMC. Figure 3.8 demonstrates that the number of function evaluations required to explore $f^{-1}(\mathbb{Y})$ also remains approximately constant as the probability magnitude decreases.

This concludes the presentation of results of numerical experiments. The next section explores how A-BIMC can fail, and in particular, offers explanations for why A-BIMC performed unsatisfactorily in experiments F1 and F2 in Section 3.4.2.

3.5 Failure

In this section, we explore how A-BIMC can fail. A-BIMC's failure is tied to inappropriately choosing the tolerance ϵ_{abs}, or the number of samples used by MPMC per iteration, N_{MPMC} (in order to keep the number of tunable parameters to a minimum, we always choose $\epsilon_{\text{rel}} = 1 - \epsilon_{\text{abs}}$). Hence, this section doubles as a discussion on the consequences of choosing these parameters inappropriately. In addition to exploring the mechanisms behind failure, recommendations for diagnosing, as well as mitigating it, are offered.

Inappropriate ϵ_{abs} Recall that ϵ_{abs} is a tolerance on how similar mixtures are allowed to be from one iteration to the next in Stage-1. A smaller value of ϵ_{abs} means mixtures are allowed to be similar, which in turn implies more components will be added to the mixture in Stage-1. Adding more components is advantageous for two reasons – it aids discovery of disjoint regions of $f^{-1}(\mathbb{Y})$, and leads to a more accurate surrogate $f_{\text{surrogate}}$ (this fact illustrated in Figure 3.9 for the toy problem). At the same time, adding more components requires solving more optimization problems, driving up the computational cost of Stage-1. Clearly, ϵ_{abs} represents trade-off between a smaller computational footprint and better discovery of $f^{-1}(\mathbb{Y})$. However, an *a priori* prescription for ϵ_{abs} remains elusive at this time.

A possible hypothesis for why A-BIMC performed poorly in experiment F1 is that $\epsilon_{\text{abs}} = 1 - 10^{-3}$ was too loose, leading to an inaccurate surrogate. Running A-BIMC at $\epsilon_{\text{abs}} =$

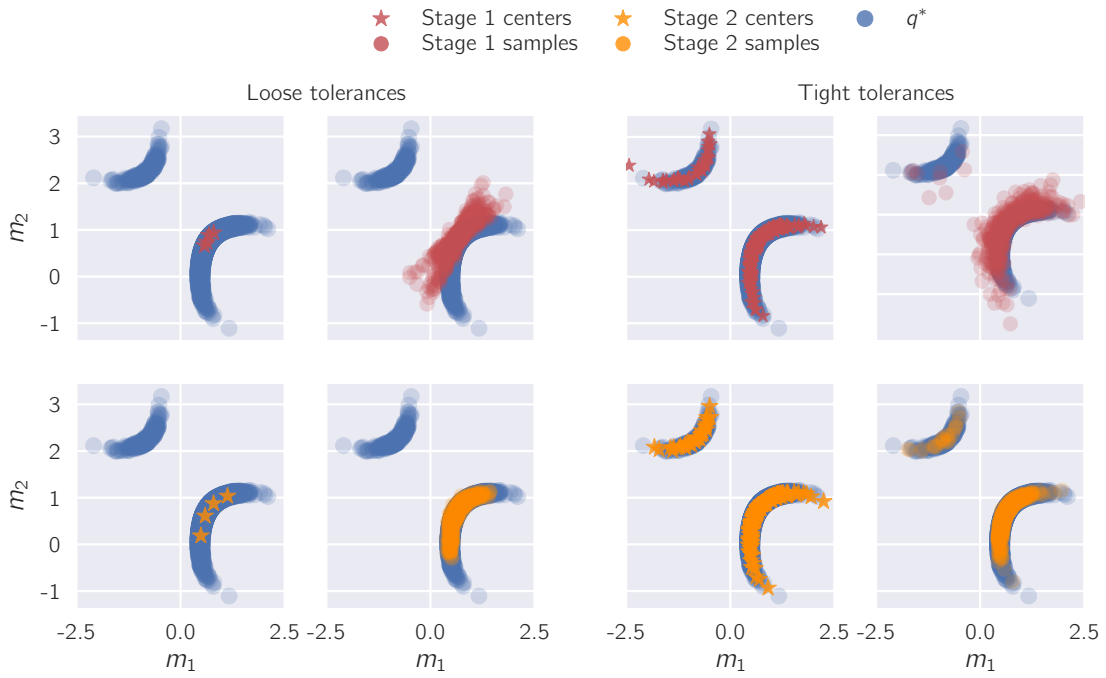

Figure 3.9: *This figure illustrates the effect of varying the tolerances* ϵ_{abs} *and* ϵ_{rel}*. The left half of the figure corresponds to a loose tolerance,* $\epsilon_{\text{abs}} = 1 - 10^{-1}$*, while the right half corresponds to a tighter tolerance,* $\epsilon_{\text{abs}} = 1 - 10^{-5}$*. In both cases,* $\epsilon_{\text{rel}} = 1 - \epsilon_{\text{abs}}$ *and* $N_{\text{MPMC}} = 10^6$*. Tighter tolerances lead to a greater number of components in the mixture and can aid the discovery of disjoint regions of* $f^{-1}(\mathbb{Y})$*. However, they increase the computational cost. For instance,* $\epsilon_{\text{abs}} = 1 - 10^{-1}$ *required 266 function evaluations, whereas* $\epsilon_{\text{abs}} = 10^{-5}$ *required 19749. All cases show 5000 samples from* q^* *and 500 samples from the IS mixture obtained after Stages 1 and 2.*

$1 - 10^{-4}$ immediately improves the surrogate, and consequently, A-BIMC's performance, lending credibility to this hypothesis (see Figure 3.10a). Therefore, an inappropriate ϵ_{abs} can be diagnosed by a low ESS. Note that A-BIMC need not be re-run from scratch to correct for loose ϵ_{abs}. Let Q_1^{loose} and $\boldsymbol{\chi}_{\text{fixed}}^{\text{loose}}$ denote the IS mixture and set of fixed charges computed at the end of Stage-1 with a loose ϵ_{abs}. Then, rectifying the effect of a loose ϵ_{abs} simply involves starting from Q_1^{loose} and $\boldsymbol{\chi}_{\text{fixed}}^{\text{loose}}$ and re-running lines 10-17 of Algorithm 5 using a tighter ϵ_{abs}. This will have the same effect as a cold restart of A-BIMC using the tighter tolerance.

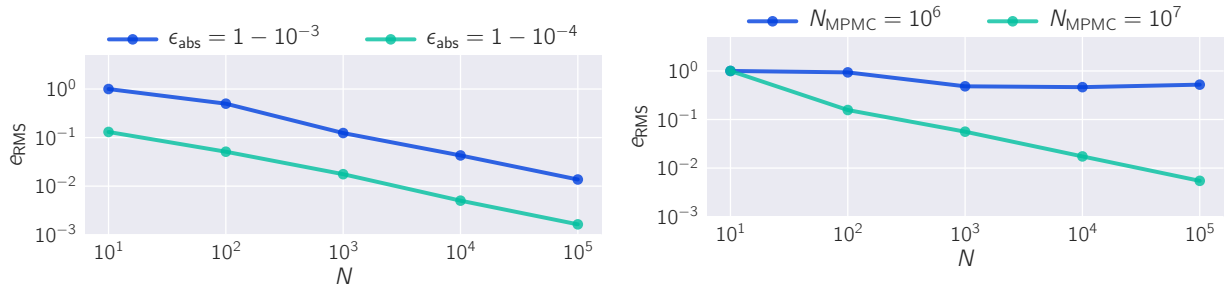

(a) *Failure case F1 is remedied by increasing* ϵ_{abs}. **(b)** *Failure case F2 is remedied by increasing* N_{MPMC}.

Figure 3.10: *Fixing failure cases F1 and F2. Decreasing* ϵ_{abs} *in failure case F1 increased the number of function calls from 1765 to 3429.*

Poor surrogates The surrogate used to replace full evaluations of $f(\boldsymbol{m})$ is a heuristic, and unfortunately, possesses no guarantees as to its accuracy. If the surrogate poorly approximates $f(\boldsymbol{m})$, then the resulting mixture will be a poor approximation of $\mathbf{1}_{\mathbb{Y}}(f(\boldsymbol{m}))$. This failure is tied to choosing an inappropriate ϵ_{abs}, but can also occur independently, for instance when no computationally tractable ϵ_{abs} can deliver a surrogate that is accurate enough.

High ambient dimensionality MPMC is particularly susceptible to failure when the dimension of the parameter $\boldsymbol{m}$ is high. This is because the update formulae for α_k's, $\boldsymbol{m}_k$'s and $\boldsymbol{\Sigma}_k$'s in MPMC are posed as high-dimensional integrals. These integrals are approximated via IS, and at a given sample size, become poorer approximations of the the true updates as the dimension of the parameters increases. This failure mechanism usually manifests as one of the $\boldsymbol{\Sigma}_k$'s becoming rank-deficient during the tuning procedure. This is the mechanism of failure in experiment F2. In this case, it is truly the high ambient dimensionality of the problem, and not other factors, such as an inaccurate surrogate, that cause MPMC to fail. This is confirmed in Figure 3.10b, where MPMC is rerun using $N_{\text{MPMC}} = 10^7$, but with the same surrogate. Increasing N_{MPMC} successfully improves performance. This failure mode usually manifests as a rank-deficient covariance matrix in one of the mixture components during MPMC, and it can be fixed by increasing N_{MPMC}. Note that such a failure mode, compared to an inappropriate ϵ_{abs}, is relatively benign as it doesn't require additional evaluations of f.

Inspired by recent progress in dimension reduction for non-linear Bayesian inverse problems [24, 96], we believe that this deterioration in performance with increasing ambient dimensionality can be arrested. In the next subsection, we preview a general dimension reduction strategy that has the potential to lead to importance sampling algorithms that are independent of the ambient dimension of the problem.

3.6 Dimension reduction

The key to our dimension reduction strategy is the observation that in many natural applications, the density p is smoothing and the parameter-to-QoI map f is only dependent on a few directions in parameter space. In fact, this is precisely how BIMC was able to achieve optimality for the affine-Gaussian case, where f was only sensitive to variations of the parameter $\boldsymbol{m}$ along a single direction $m_1 = \boldsymbol{v}^\top \boldsymbol{m}$. Here, we extend this idea more

generally. We begin our analysis by studying maps which are sensitive to at most $r \ll d$ directions in the input space. After shedding light on the structure of the ideal IS density for such maps, we theoretically establish that exploiting this r dimensional *dominant subspace* is imperative. Finally, based on this analysis, we outline a dimension reduction strategy for the more realistic situation where the map f depends more strongly on at most r directions in parameter space than others.

Let $f : \mathbb{R}^d \to \mathbb{R}$ be a map that only depends on at most $r \ll d$ directions in $\mathbb{R}^d$. Also, let $\boldsymbol{\Phi}_r \in \mathbb{R}^{d\times r}$ be a $\boldsymbol{\Sigma}_0^{-1}$-orthogonal basis (*i.e.*, $\boldsymbol{\Phi}_r^\top \boldsymbol{\Sigma}_0^{-1} \boldsymbol{\Phi}^\top = \boldsymbol{I}_r$) for this r-dimensional dominant subspace. If $\boldsymbol{\Phi}_\perp$ is chosen so that $[\boldsymbol{\Phi}_r, \boldsymbol{\Phi}_\perp]$ forms a complete orthonormal system in $\mathbb{R}^d$, then any $\boldsymbol{m} \in \mathbb{R}^d$ can be expressed as:

$$\boldsymbol{m} = \boldsymbol{\Phi}_r \boldsymbol{m}_r + \boldsymbol{\Phi}_\perp \boldsymbol{m}_\perp,$$

where $\boldsymbol{m}_r \in \mathbb{R}^r$ and $\boldsymbol{m}_\perp \in \mathbb{R}^{d-r}$ are the coefficients associated with the bases $\boldsymbol{\Phi}_r$ and $\boldsymbol{\Phi}_\perp$. Because $\boldsymbol{\Phi}_r$ is $\boldsymbol{\Sigma}_0^{-1}$-orthogonal, it decorrelates the dominant subspace, Range($\boldsymbol{\Phi}_r$), and its complement, Range($\boldsymbol{\Phi}_\perp$), so that the nominal distribution $p(\boldsymbol{m})$ is expressible as the product of independent marginals, p_r and $p_\perp$:

$$p(\boldsymbol{m}) = p_r(\boldsymbol{m}_r) p_\perp(\boldsymbol{m}_\perp) \tag{3.9}$$

Consequently, the ideal importance sampling density becomes (up to a normalizing constant):

$$\begin{aligned} q^*(\boldsymbol{m}) &\propto \mathbf{1}_{\mathbb{Y}}(f(\boldsymbol{m})) p(\boldsymbol{m}) \\ &\propto \mathbf{1}_{\mathbb{Y}}(\hat{f}(\boldsymbol{m}_r)) p_r(\boldsymbol{m}_r) p_\perp(\boldsymbol{m}_\perp) \end{aligned} \tag{3.10}$$

where we've taken advantage of the fact that f is insensitive to variations along Range($\Phi_\perp$), and hence $\boldsymbol{m}_\perp$, and used the prior factorization in Equation (3.9).

Equation (3.10) reveals that the ideal IS distribution $q^*(\boldsymbol{m})$ can be factorized into a *reduced* ideal distribution $q_r^* \propto \mathbf{1}_{\mathbb{Y}}(\hat{f}(\boldsymbol{m}_r))p_r(\boldsymbol{m}_r)$ and the marginal $p_\perp$. Such a factorization is advantageous, because it implies that the full ideal IS density q^* differs from the nominal distribution only over an r-dimension subspace, or, in other words, the *intrinsic dimension* of the rare-event simulation problem is r. Knowing that q^* is identical to $p_\perp$ in Range($\boldsymbol{\Phi}_\perp$) precludes its exploration in that subspace. Therefore, importance sampling need only approximate q_r^*, a distribution in $\mathbb{R}^r$, a task much more tractable than trying to approximate q^* in $\mathbb{R}^d$, especially when $r \ll d$. In fact, the following theorem establishes that not exploiting this lower-dimensional structure leads to estimators of poorer quality.

Theorem 1 (Rao-Blackwellisation). *If f is independent of $\boldsymbol{m}_\perp$, then no IS distribution $q(\boldsymbol{m}_r, \boldsymbol{m}_\perp)$ can perform better than its marginal $q_r(\boldsymbol{m}_r)$. The two distributions will perform equally well iff $q(\boldsymbol{m}_r, \boldsymbol{m}_\perp) = q_r(\boldsymbol{m}_r)p_\perp(\boldsymbol{m}_\perp)$.*

Proof. We begin the proof by defining the importance sampling estimator based on $q(\boldsymbol{m}_r, \boldsymbol{m}_\perp)$:

$$\psi(\boldsymbol{m}_r, \boldsymbol{m}_\perp) = \frac{\mathbf{1}_{\mathbb{Y}}(f(\boldsymbol{m}_r))p_r(\boldsymbol{m}_r)p_\perp(\boldsymbol{m}_\perp)}{q(\boldsymbol{m}_r, \boldsymbol{m}_\perp)} \tag{3.11}$$

The Rao-Blackwellized version of this estimator is its conditional expectation given $\boldsymbol{m}_r$:

$$\psi_{\mathrm{RB}}(\boldsymbol{m}_r) = \int \psi(\boldsymbol{m}_r, \boldsymbol{m}_\perp) q_\perp(\boldsymbol{m}_\perp, \boldsymbol{m}_r) \mathrm{d}\boldsymbol{m}_\perp \tag{3.12}$$

$$= \int\int \frac{\mathbf{1}_{\mathbb{Y}}(f(\boldsymbol{m}_r)) p_r(\boldsymbol{m}_r) p_\perp(\boldsymbol{m}_\perp)}{q(\boldsymbol{m}_r, \boldsymbol{m}_\perp)} q_\perp(\boldsymbol{m}_\perp|\boldsymbol{m}_r) \mathrm{d}\boldsymbol{m}_r \mathrm{d}\boldsymbol{m}_\perp \tag{3.13}$$

$$= \frac{\mathbf{1}_{\mathbb{Y}}(f(\boldsymbol{m}_r) p_r(\boldsymbol{m}_r)}{q_r(\boldsymbol{m}_r)} \tag{3.14}$$

In other words, the Rao-Blackwellized version of $\psi(\boldsymbol{m}_r, \boldsymbol{m}_\perp)$ is nothing but the IS estimator based on the marginal $q_r(\boldsymbol{m}_r)$. In addition,

$$\mathbb{E}_{\boldsymbol{m}_r}\left[\psi_{\mathrm{RB}}(\boldsymbol{m}_r)\right] = \int \psi_{\mathrm{RB}}(\boldsymbol{m}_r) q_r(\boldsymbol{m}_r) \mathrm{d}\boldsymbol{m}_r \tag{3.15}$$

$$= \int\int \psi(\boldsymbol{m}_r, \boldsymbol{m}_\perp) q_\perp(\boldsymbol{m}_r, \boldsymbol{m}_\perp) q_r(\boldsymbol{m}_r) \mathrm{d}\boldsymbol{m}_r \mathrm{d}\boldsymbol{m}_\perp \tag{3.16}$$

$$= \mu \tag{3.17}$$

Hence, ψ_{RB} is an unbiased estimator of μ. Then, using the relationship between the variance of conditional and unconditional expectations, we have,

$$\mathbb{V}_{\boldsymbol{m}}(\psi(\boldsymbol{m}_r, \boldsymbol{m}_\perp)) = \mathbb{V}_{\boldsymbol{m}_r}\left[\mathbb{E}_{\boldsymbol{m}_\perp|\boldsymbol{m}_r}(\psi(\boldsymbol{m}_r, \boldsymbol{m}_\perp))\right] + \mathbb{E}_{\boldsymbol{m}_r}\left[\mathbb{V}_{\boldsymbol{m}_\perp|\boldsymbol{m}_r}(\psi(\boldsymbol{m}_r, \boldsymbol{m}_\perp))\right] \tag{3.18}$$

$$= \mathbb{V}_{\boldsymbol{m}_r}\left[\psi_{\mathrm{RB}}\right] + \mathbb{E}_{\boldsymbol{m}_r}\left[\mathbb{V}_{\boldsymbol{m}_\perp|\boldsymbol{m}_r}(\psi(\boldsymbol{m}_r, \boldsymbol{m}_\perp))\right] \tag{3.19}$$

Since $\mathbb{V}_{\boldsymbol{m}_r, \boldsymbol{m}_\perp}(\cdot) \geq 0$, the variance of the IS estimator based on $q(\boldsymbol{m}_r, \boldsymbol{m}_\perp)$ is never smaller than the variance of the IS estimator based on $q_r(\boldsymbol{m}_r)$.

The two estimators are of equal quality iff $\mathbb{V}_{\boldsymbol{m}_\perp|\boldsymbol{m}_r}\left[\psi(\boldsymbol{m}_r, \boldsymbol{m}_\perp)\right] = 0$. The variance of a random variable is zero iff it's a constant. This implies that $\psi(\boldsymbol{m}_r, \boldsymbol{m}_\perp)$ must be independent of $\boldsymbol{m}_\perp$. In other words, $\psi(\boldsymbol{m}_r, \boldsymbol{m}_\perp)$ must be constant that depends only on $\boldsymbol{m}_r$. But, according to its definition,

$$\begin{aligned}\psi(\boldsymbol{m}_r, \boldsymbol{m}_\perp) &= \frac{\mathbf{1}_{\mathbb{Y}}(f(\boldsymbol{m}_r))p_r(\boldsymbol{m}_r)p_\perp(\boldsymbol{m}_\perp)}{q(\boldsymbol{m}_r, \boldsymbol{m}_\perp)} \\ &= \frac{\mathbf{1}_{\mathbb{Y}}(f(\boldsymbol{m}_r))p_r(\boldsymbol{m}_r)}{q_r(\boldsymbol{m}_r)} \frac{p_\perp(\boldsymbol{m}_\perp)}{q_\perp(\boldsymbol{m}_\perp|\boldsymbol{m}_r)}\end{aligned} \tag{3.20}$$

Hence, $p_\perp(\boldsymbol{m}_\perp)/q_\perp(\boldsymbol{m}_\perp|\boldsymbol{m}_r)$ must be a function of $\boldsymbol{m}_r$. Since $q_\perp(\boldsymbol{m}_\perp|\boldsymbol{m}_r)$ and $p_\perp(\boldsymbol{m}_\perp)$ are proper distributions, this function must be 1. Therefore, we've showed that the two estimators are of equal quality iff $q_\perp(\boldsymbol{m}_\perp|\boldsymbol{m}_r) = p_\perp(\boldsymbol{m}_\perp)$, and thus $q(\boldsymbol{m}_r, \boldsymbol{m}_\perp) = q_r(\boldsymbol{m}_r)p_\perp(\boldsymbol{m}_\perp)$. □

Theorem 1 tells us that for forward maps that are insensitive to a linear subspace of the parameter space, a good choice for an IS distribution is one that marginalizes to the complement prior $p_\perp$. Trying to devise an IS distribution in the full parameter space, then, is a futile attempt, since it'll always perform worse than its marginal – unless of course, one arrives at a distribution in the full space that fortuitously marginalizes to the complement prior.

In natural practical applications, one rarely encounters such a clean separation between a dominant and non-dominant subspace for a parameter-to-QoI map f. However, maps that strongly depend on a handful of dimensions in the parameter space and weakly dependent on the rest are quite common. For such situations, we recommend the following dimension reduction approach. Construct the IS distribution in the dominant subspace q_r, but augment it with the complement prior $p_\perp$ to evaluate the rare-event probability. The importance sampling estimator based on N samples then becomes:

$$\tilde{\mu}_N = \frac{1}{N}\sum_{i=1}^{N} \mathbf{1}_{\mathbb{Y}}(f(\boldsymbol{\Phi}_r\boldsymbol{m}_{r,i} + \boldsymbol{\Phi}_\perp\boldsymbol{m}_{\perp,i}))\frac{p_r(\boldsymbol{m}_{r,i})p_\perp(\boldsymbol{m}_{\perp,i})}{q_r(\boldsymbol{m}_{r,i})p_\perp(\boldsymbol{m}_{\perp,i})}, \tag{3.21}$$

where $\boldsymbol{m}_{r,i} \sim q_r(\boldsymbol{m}_r)$ and $\boldsymbol{m}_{\perp,i} \sim p_\perp(\boldsymbol{m}_{\perp,i})$. Of course, $p_\perp$ cancels in Equation (3.21), but has been included for clarity. Note that constructing q_r in the reduced subspace can be accomplished using any algorithm, for instance, A-BIMC, or even MPMC alone. The methodology described above simply reduces the dimension in which the chosen IS algorithm is employed, and is agnostic to the actual choice of the algorithm. Therefore, the prescription above has the potential to make existing algorithms independent of the ambient dimension of the problem.

Throughout this section, we assumed the knowledge of a dominant r-dimensional subspace. However, identifying such subspaces for arbitrary f and p is still an open research question. Several approaches have been proposed in the context of dimension-reduction for Bayesian inference [24, 96]. A common feature of these schemes is that the dominant subspace is defined as the subspace spanned by the r leading eigenvectors of an average Hessian-like object. For instance, in Active Subspaces [24], the average Hessian-like object is the prior-averaged covariance of the gradient, while in [96], it's the posterior-averaged covariance of the log-likelihood gradient. We conjecture that a similar approach can be adopted in the context of rare-event importance sampling as well, but leave identifying the appropriate averaged Hessian as future work.

3.7 Conclusion and future work

In this chapter, we extend the applicability of BIMC, an algorithm for computing rare-event probabilities. The extended algorithm, called Adaptive-BIMC, proceeds in two stages. In Stage-1, A-BIMC constructs a rough approximation of the (theoretical) ideal importance sampling distribution by exploring the regions that trigger the rare-event on a global scale. This is in contrast to BIMC, which can only achieve local exploration of the region of interest around the so-called pseudo-MAP point. Global exploration in A-BIMC is achieved by solving a sequence of optimization problems to discover points along the region of interest, and

then accruing the discovered points into a Gaussian mixture distribution. Both the optimization, and the covariances of the components in the Gaussian mixture are derivative-aware. Stage 2 of A-BIMC refines the rough approximation yielded by Stage 1 using the Mixture Population Monte Carlo algorithm. While this would usually require further evaluations of the forward map, we avoid doing so by using a heuristic surrogate which is constructed on-the-fly.

Results from several numerical experiments allow us to make the following conclusions:

- A-BIMC is independent of the rarity level of the problem, a trait desirable from any scheme that aims to efficiently compute rare-event probabilities
- A-BIMC does break down as the ambient dimensionality of the problem increases. This breakdown is due to MPMC, the algorithm employed to refine the Gaussian mixture distribution yielded by Stage 1.

We also outlined a general dimension reduction strategy for rare-event importance sampling. The key observation here was that the breakdown of IS schemes with increasing ambient dimension can be arrested by employing those algorithms only in the subspace in which the ideal importance sampling density differs from the nominal distribution. The challenge here will be to discover the subspace in question. In the future, we aim to apply techniques developed for dimension reduction in Bayesian inverse problems [24, 96] to reduce the dimension of the rare-event probability estimation problem.

Chapter 4

Inferring fault transmissibilities from production data: a Bayesian approach

The previous chapters focused on rare-event probability estimation, where the goal was to efficiently explore probability distributions conditioned to the *occurrence of a rare-event*. In this chapter, we focus on exploring a different kind of conditional probability distribution – one where the conditioning occurs with respect to *observed data*. Within the Bayesian perspective, this conditional probability distribution is nothing but the *posterior* distribution, which provides a complete description of uncertainties in the system, accounting for prior knowledge, observed data, and measurement and/or modeling errors. The posterior distributions we consider in this chapter originate from hydrocarbon reservoirs containing faults whose transmissibilities are unknown, and hence uncertain. Directly measuring the petrophysical properties that control the transmissibilities is rarely possible; the only recourse is to indirectly infer them from production data captured over the lifetime of the reservoir. This chapter describes a Bayesian formulation to do so. In addition to describing our Bayesian formulation, we also investigate how the posterior uncertainties change under different reservoir conditions via numerical experiments. The end goal of this analysis is facilitate uncertainty-equipped production forecasts of the reservoir. Therefore, beyond just reporting uncertainties in the fault transmissibilities, we also propagate them to production forecasts and explore the nature of uncertainties that result.

4.1 Introduction

Faults in hydrocarbon bearing reservoirs can significantly influence fluid flow. For instance, faults aid the injected fluid in sweeping hydrocarbons from the reservoir. On the other hand, they can also seal hydrocarbon-rich regions from the injected fluid, making recovery nearly impossible. Since faults directly affect the financial performance of a reservoir, knowing their relevant petrophysical properties is crucial for prudent reservoir operation. Gathering this knowledge remains challenging, however, as directly measuring fault-zone properties is seldom possible. The only feasible recourse that remains is to infer these properties indirectly from production data.

This procedure, commonly referred to as history-matching, is inherently computational. Computational models of the reservoir are calibrated against observed data, and then used to issue predictions regarding the future performance of the reservoir. In such computational models, faults are represented as surfaces of co-dimension one, i.e., as surfaces in 3D, and lines in 2D. Their petrophysical properties get lumped into a single quantity, known as the transmissibility multiplier. The transmissibility multiplier for each fault acts as a computational proxy for its petrophysical properties. As faults are almost always incorporated via transmissibility multipliers, it makes sense to bypass the petrophysical properties, and directly infer transmissibilities from production data.

In this chapter, we study the problem of inferring fault transmissibilities from production data. To do so, we consider synthetic two-dimensional reservoirs containing multiple faults, and prescribe a constant, but unknown, transmissibility to each fault. We assume that production data is available in the form of noisy pressure measurements recorded at the wells at regular time intervals. To model fluid flow within the reservoir, we use a transient, compressible, two-phase flow model, coupled with a reduced model for fault behavior.

We are especially interested in quantifying uncertainty in our inferred estimate of the fault transmissibilities. This is so that any operational decisions that rely on the inferred trans-

missibilities are made with full awareness of the confidence (or lack thereof) in that estimate. For this reason, we adopt the Bayesian perspective to pose our inference problem. The end result of Bayesian inference is a *posterior* description of uncertainty, expressed as a probability distribution, which is consistent with *prior* knowledge as well as production data, while being cognizant of measurement and/or model errors. Adopting the Bayesian approach has the added advantage of dealing with the natural ill-posedness of the problem. The fact that multiple sets of transmissibilities can be equally consistent with the observed data is naturally expressed within the probability density representation. The posterior distribution can then be used to quantify uncertainties in decision-relevant Quantities-of-Interest (QoIs). For instance, knowing these uncertainties can help estimate the risk associated with financial decisions, or predict the possible range over which production forecasts are expected to vary.

Contributions. Our primary goal in this chapter is to explore uncertainties in the inferred fault transmissibilities, propagate them to decision-relevant Quantities-of-Interest (QoIs), and most importantly, explore how these uncertainties are affected by changing reservoir conditions. In summary, our contributions are:

- We combine advances in fault modeling [4, 7, 56] with state-of-the-art algorithms for Bayesian inference [25, 46] to solve the problem of inferring fault transmissibilities from production data.
- We study how posterior uncertainties in the fault transmissibilities and decision-relevant QoIs change under different reservoir configurations using two numerical experiments:
  - First, we consider a reservoir with two faults and investigate the effect of varying their relative arrangement on posterior uncertainties.

– Next, we consider a more realistic situation where the location of only a few major faults is known with certainty. That is, the presence of smaller faults is suspected, but their location and number are unknown. We explore whether production data can help pinpoint the location of the smaller faults and the nature of the uncertainties that result.

Owing to the strongly non-linear nature of the problem, an analytical exploration of these issues isn't possible.

Limitations. Our work has several limitations which we summarize below:

- A major drawback of our study is that it's two-dimensional.
- Although faults have a finite thickness, we represent them using an interface. This is standard practice when building computational models of faults, as fault thicknesses are often too small to be resolved on a computational mesh.
- We make several simplifying assumptions in our flow models. Specifically, we neglect capillary pressure and gravity. Within the fault regions, we assume that the permeability along the length of the fault is zero, while permeability normal to the fault is uniform. In addition, the reservoirs we consider in this study are simple idealizations. This is intentional. Our goal is to develop intuition and provide easily interpretable results that don't depend on the specific details of the field under study.

Related work The body of work on reservoir simulation, fault modeling, and Bayesian inference is extensive. Here, we review work that is most relevant to our study.

Subsurface flow and fault models. Depending on the recovery mechanism and the physical state of the fluids, flow within a hydrocarbon reservoir can involve multiple fluid phases and

components [22,51]. As a compromise between ease of implementation and predictive power, we only consider two-phase compressible flow during secondary production. We again refer to [22,51] for the derivation of the governing PDEs.

Despite being valid flow descriptions, these governing PDEs are rarely solved exactly within the fault regions. This is because meshing faults and capturing the sharp flow gradients induced by them can be computationally expensive. To circumvent this, the effect of faults on fluid flow is modeled. One common approach is to average the governing PDEs across the aperture of the fault to arrive at a reduced set of equations. Such reduced models, which effectively render the fault as an interface, have been derived for single-phase flows [7,34,35, 56,87], two-phase flows [4,36,45,72], as well as compositional flow [44]. A separate class of fault models, known as dual-porosity/permeability models, treat the subsurface as consisting of two-separate coexisting continua [8,13,93]. However, these models are restricted to dense fault networks that possess higher porosity and permeability than the host rock. In this study, we use the fault model in [4].

History matching. Faults have been the subject of several history-matching studies, using a variety of subsurface flow models, production data, and algorithms to quantify uncertainty. For a general review of history-matching methods, see [61]. In [3], the authors manually tuned fault sealing parameters to match production data. The studies in [76,81] used genetic algorithms to infer, among other unknown reservoir properties, fault transmissibilities. All these studies used deterministic methods, that is, methods that only yield a point-estimate of the inferred parameters, and did not quantify uncertainty.

Uncertainty estimates for the inferred fault transmissibilities, again jointly with other reservoir unknowns, are reported in [30–32,82]. Notably, all of these studies used the Ensemble Kalman Filter (EnKF) to estimate uncertainties. Indeed, the EnKF and its variants have become a popular algorithm for history-matching in general [1,20,21,40,83]. A major drawback of these algorithms, however, is that they only keep track of the first two moments

of the ensemble, thereby ignoring non-Gaussian effects. As a result the ensemble uncertainty may not be consistent with the true posterior uncertainty for non-linear problems. In addition, none of the previous studies have investigated how posterior uncertainties in the fault transmissibilities change under different reservoir conditions. Our work evaluates the performance of a full Bayesian perspective.

In order to explore posterior uncertainties, we employ the Markov Chain Monte Carlo (MCMC) method [73]. The challenge is to design a transition kernel that lets the Markov chain explore the posterior distribution efficiently. A wide range of ideas have been proposed to address this challenge, such as leveraging Langevin diffusions [25, 39, 55, 75], using low-fidelity approximations of the likelihood distribution [23, 29], exploiting tractable approximations of the posterior [16, 62, 62, 67], and recently, transport maps [64]. Our approach follows [25], wherein a small modification to the Random-Walk Metropolis-Hastings algorithm results in a Langevin diffusion with attractive properties.

In addition to exploring posterior uncertainties, we also assess the validity of approximating the posterior distribution via Laplace's approximation [50, 95] as a cheaper means of quantifying uncertainty. This has been previously been considered in history-matching literature [61, 62], as well as more generally for Bayesian inverse problems [16, 46, 68, 79]. An intermediate step in computing Laplace's approximation is finding the mode of the posterior, which is equivalent to a deterministic history-matching procedure. We employ gradient-accelerated algorithms, following [16, 46]. The gradients are computed using the method of adjoints [41].

Notation and Organization. This chapter is organized as follows. In Section 4.2, we describe the model we use to solve the forward problem: given fault transmissibilities, predict the pressure observations at the wells. We describe how we setup the inverse problem to infer fault transmissibilities from pressure observations in Section 4.3. Section 4.4 describes

Symbols/Acronyms	Meaning
DG	Discontinuous Galerkin
MAP	Maximum *A Posteriori*
CG	Conjugate Gradient
MCMC	Markov Chain Monte Carlo
pCN	preconditioned Crank Nicholson
RWMH	Random Walk Metropolis Hastings
NPV	Net Present Value
$\boldsymbol{x}$	spatial coordinates, $\boldsymbol{x} = [x_1, x_2]$
t	time
Ω	spatial domain
Γ_i	i-th fault
K	permeability field
$K_{f,i}$	normal permeability of the i-th fault
ϕ	porosity field
p	global pressure
$\boldsymbol{v}$	total velocity
S_w	saturation of the wetting phase
$\boldsymbol{u}$, $\mathbf{u}$	continuous and discrete state variable
$\boldsymbol{m}$	vector of fault log-transmissibilities
$\mathbf{p_n}$	adjoint variable at time t_n
T	lifetime of the reservoir
T_{obs}	time at which data collection ends
$\mathcal{B}$, $\mathbf{B}$	continuous and discretized observation operator
π_{like}, π_{prior}, π_{post}, π_{laplace}	likelihood, prior, posterior, and Laplace approximation
∇	gradient operator
$\nabla\cdot$	divergence operator
$[\![\cdot]\!]$	jump operator

Table 4.1: *Summary of key notation used in this chapter.*

two decision-relevant Quantities-of-Interest. We report results from numerical experiments in Section 4.5. In Section 4.6, we summarize our conclusions and discuss possible avenues for future work.

Frequently used symbols in this chapter and their meaning are listed in Table 4.1.

4.2 The forward problem

In this section, we formulate a relationship between the fault transmissibilities and the pressure distribution of the fluids within the reservoir. We begin, in Section 4.2.1, by reviewing a general model for fluid flow in porous media. Although this model applies to the entire reservoir, including the fault regions, we employ a separate, reduced model for faults. We discuss our motivation for doing so and the details of the reduced model in Section 4.2.2. Then, in Section 4.2.3, we discuss how we include wells in our formulation. Taken together, these models form a coupled PDE system, which implicitly relates the fault transmissibilities and the fluid pressure. We summarize this PDE system in Section 4.2.4, and discuss numerical methods for solving it in Section 4.2.5. Throughout this section, we will use the abstract reservoir in Figure 4.1 as a reference.

In our reservoir flow model, we account for the presence of up to two immiscible and compressible liquid phases – oil and water. We start by introducing the saturation of each phase as the fraction of pore volume occupied by it. Since, both fluids fill the entire pore volume, the oil and water saturations, S_w and S_o, must add up to 1: $S_w + S_o = 1$[1].No mass transfers across phases as they're immiscible. Hence, the statement of mass conservation becomes:

[1]Here, and in what follows, we will use the subscripts w and o to refer to the water and oil phases respectively. When making a statement that holds for both phases, we will use the subscript α.

$$\frac{\partial \phi \rho_\alpha S_\alpha}{\partial t} + \nabla \cdot (\rho_\alpha \boldsymbol{v}_\alpha) = \rho_\alpha q_\alpha \quad \alpha = o, w, \tag{4.1}$$

where ϕ is the porosity of the medium, $\boldsymbol{v}_\alpha$ is the velocity of phase α, ρ_α is its density, and q_α is its volumetric production rate. Further, due to surface tension effects, the oil and liquid phases are at different pressures, $p_w \neq p_n$.

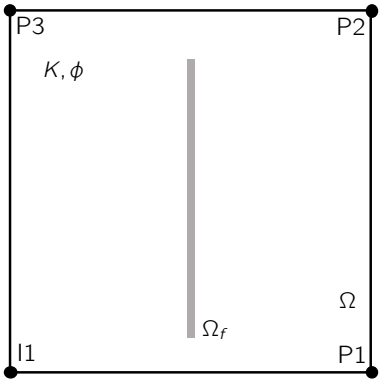

Figure 4.1: *An abstract reservoir Ω containing a fault Ω_f, injection well I1, and production wells P1, P2, P3.*

4.2.1 Porous media flow

According to this formulation, the state of each phase is described by its saturation, velocity, pressure, and because we consider compressible flow, its density. However, at this stage, there are more unknowns than equations, and it becomes necessary to introduce assumptions to close the system.

First, we assume that each phase follows a multi-phase extension of Darcy's law. If $\boldsymbol{K}$ is the permeability tensor of the rock matrix, and $\boldsymbol{g}$ is the acceleration due to gravity, then $\boldsymbol{v}_\alpha$ satisfies

$$\boldsymbol{v}_\alpha = \frac{-k_{r\alpha}\boldsymbol{K}}{\mu_\alpha}(\nabla p_\alpha - \rho_\alpha \boldsymbol{g}), \tag{4.2}$$

where μ_α and ρ_α are the viscosity and density of phase α and $k_{r\alpha}$ is the relative permeability function. The relative permeability function accounts for the fact that each phase in the porous medium hinders the movement of the other, effectively lowering its velocity. The relative permeability function is modeled to be a function of the phase saturation, $k_{r\alpha} = k_{r\alpha}(S_\alpha)$. Another closure relationship comes from the capillary pressure, which is defined as the difference between the phase pressures, $p_c = p_o - p_w$, and is modeled, empirically, as a function of the water saturation $p_c = p_c(S_w)$.

The modeling assumptions and constitutive relationships described so far are a complete description of fluid flow in the reservoir. To simplify our implementation of this reservoir flow model, we impose that:

- gravity is negligible, $\boldsymbol{g} = \boldsymbol{0}$,
- assume that everywhere except the fault region, the permeability tensor is isotropic, $\boldsymbol{K}(\boldsymbol{x}) = K(\boldsymbol{x})\boldsymbol{I}, \forall \boldsymbol{x} \in \Omega \backslash \Omega_f$,
- capillary pressure is negligible, implying equal phase pressures, $p_w = p_o$,
- the relative permeability function is a quadratic function of the phase saturations $k_{r\alpha} = S_\alpha^2$.

In light of the simplifications above, the final reservoir model is summarized below:

$$
\begin{aligned}
\boldsymbol{v} &= -(\lambda_w + \lambda_o)\boldsymbol{K}\nabla p \quad \text{in}\,\Omega, \\
\Bigg(\phi\left(c_r + (1-S_w)c_n + S_w c_w\right)\frac{\partial p}{\partial t} &+ \nabla\cdot\boldsymbol{v} \\
&- \left[c_w\lambda_w + c_n\lambda_o\right]\frac{\boldsymbol{v}\cdot\boldsymbol{K}^{-1}\boldsymbol{v}}{(\lambda_w+\lambda_o)^2}\Bigg) = q_w + q_n \qquad \text{in}\,\Omega\times(0,T], \\
\frac{\partial\phi\rho_w S_w}{\partial t} &+ \nabla\cdot\left[\frac{\rho_w\lambda_w\boldsymbol{v}}{\lambda_w+\lambda_o}\right] = \rho_w q_w \qquad \text{in}\,\Omega\times(0,T],
\end{aligned}
\tag{4.3}
$$

Here, we've introduced the notion of a global pressure $p = p_w = p_n$ and a total velocity, $\boldsymbol{v} = \boldsymbol{v}_w + \boldsymbol{v}_o$. In addition, to access the global pressure p directly, we've exchanged the evolution equation for S_o for an evolution equation for p. The procedure for doing so is provided in Section C.1.

While Equation (4.3) applies to the entire reservoir, including the fault regions Ω_f, solving it numerically presents potential pitfalls. As mentioned in Section 1, the presence of faults can have a strong effect on fluid flow within a reservoir. For instance, faults whose thickness is small (relative to a representative reservoir length scale), can lead to pressure and/or velocity profiles which possess large spatial gradients. Capturing such profiles numerically can require a very fine mesh, substantially increasing the computational and memory burden of a single reservoir solve. Accomplishing an uncertainty quantification task then, which typically requires thousands of forward solves, may become prohibitively expensive. In order to accelerate the forward solve, an alternative is to forgo using a fine mesh to capture the faults and model its presence indirectly on a coarser mesh. We use such an approach in our formulation, and devote the next subsection to its description.

4.2.2 Fault model

We use the fault model derived in [4]. Here, the fault is shrunk into an interface of co-dimension one by averaging the governing flow equations across its width. This way, it acts

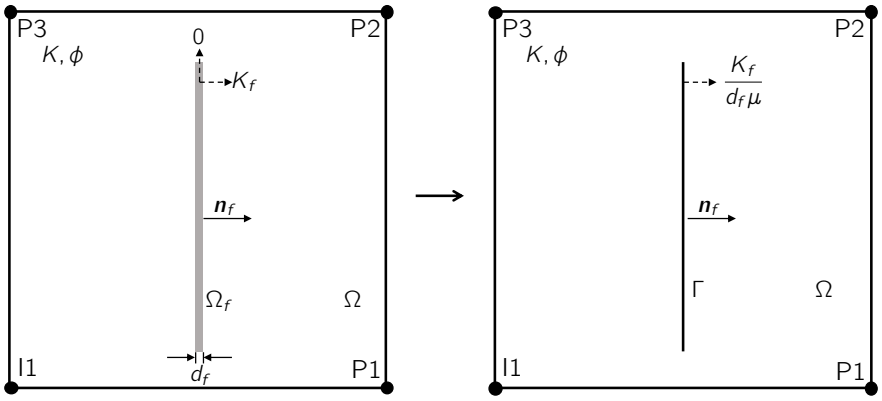

Figure 4.2: *In our reduced fault model, the fault Ω_f is shrunk across its width into an interface Γ. Assuming that the fault permeability is zero tangential to the fault and K_f normal to it, the reduced fault Γ influences flow via a single lumped quantity $e^m = K_f/(d_f\mu)$, which we call its transmissibility.*

as an internal boundary and its aperture doesn't have to be resolved on a computational mesh. The final model in [4] is a set of two-phase flow problems – one in the shrunken fault interface, say Γ, the other in the remainder of the reservoir, $\Omega\backslash\Gamma$ – coupled together via transmission conditions.

Among the many assumptions that this reduced model relies on, one asserts that the permeability tensor within the fault must be uniform, albeit anisotropic. As we incorporate this model within our formulation, we further impose that the permeability tangential to the fault must be zero, leaving only a component normal to the fault. We also assume that there are no sources or sinks within the fault, and as in Section 4.2.1, neglect capillary pressure and gravity. Consequently, the coupled two-phase flow problems of the original reduced model condense to a pair of jump conditions that dictate how the total Darcy velocity $\boldsymbol{v}$ and global pressure p change across the fault interface. For a fault Γ with thickness d_f , permeability (normal to the fault) K_f, and whose normal vector is $\boldsymbol{n}_f$, these jump conditions are:

$$[\![\boldsymbol{v} \cdot \boldsymbol{n}_f]\!]_\Gamma = 0, \text{ and, } \quad \boldsymbol{v} \cdot \boldsymbol{n}_f - \frac{K_f}{d_f \mu} [\![p]\!]_\Gamma = 0, \tag{4.4}$$

where $[\![\cdot]\!]$ is the operator which computes the jump across the fault interface, and μ is the viscosity of the fluid present initially in the fault. Figure 4.2 provides a visual illustration of the reduced fault model.

The lumped quantity $K_f/d_f\mu$, which relates the jump in global pressure ($[\![p]\!]_\Gamma$) to the total velocity flux ($\boldsymbol{v} \cdot \boldsymbol{n}_f$), is referred to as the transmissibility of the fault. Instead of working with the transmissibility directly, we will find it more convenient to work with its logarithm $m = \log(K_f/d_f\mu)$. The following equation, obtained by simple algebraic re-arrangement, offers a more physical interpretation of the log-transmissibility m:

$$m - \log \frac{K}{d_f \mu} = \log \frac{K_f}{K}. \tag{4.5}$$

Hence, the log-transmissibility is, up to a constant, nothing but the logarithm of the ratio of fracture and background permeabilities. The constant, $\log(K/d_f\mu)$, which we denote as m_0, is the log-transmissibility which leads to equal fracture and background permeabilities. We will later use m_0 to construct a prior distribution for our Bayesian inverse problem.

This completes our discussion of the fault model we employ. The final component of the reservoir that requires modeling are wells, which we discuss in the next section.

4.2.3 Well models

In this work, we only consider water flooding (or secondary production), where water is injected in to the reservoir using an injection well in order to displace oil towards production wells. This way, wells act as sources and sinks for the oil and water phases. Let there be n_I

injection wells and n_P production wells in the reservoir, located at $\{\boldsymbol{x}_I^{(i)}\}_{i=1}^{n_I}$ and $\{\boldsymbol{x}_P^{(j)}\}_{j=1}^{n_P}$ respectively. Then, the mathematical expressions for the volumetric sources and sinks are:

$$\begin{aligned} q_w &= \sum_{i=1}^{n_I} \frac{\lambda_w}{\lambda_w + \lambda_o} Q_I^{(i)} \delta(\boldsymbol{x} - \boldsymbol{x}^{(i)}) - \sum_{j=1}^{n_P} \frac{\lambda_w}{\lambda_w + \lambda_o} Q_P^{(i)} \delta(\boldsymbol{x} - \boldsymbol{x}_P^{(i)}) \\ q_o &= \sum_{i=1}^{n_I} \frac{\lambda_o}{\lambda_w + \lambda_o} Q_I^{(i)} \delta(\boldsymbol{x} - \boldsymbol{x}_I^{(i)}) - \sum_{j=1}^{n_P} \frac{\lambda_o}{\lambda_w + \lambda_o} Q_P^{(i)} \delta(\boldsymbol{x} - \boldsymbol{x}_P^{(i)}), \end{aligned} \tag{4.6}$$

where $Q_I^{(i)}$ and $Q_P^{(j)}$ refer to the total fluid flow rate (*i.e.* oil and water) through that injection or production well, and $\delta(\cdot)$ is the Dirac-δ function. The pre-multiplying factors $\lambda_w/(\lambda_w+\lambda_o)$ and $\lambda_o/(\lambda_w + \lambda_o)$ yield the fraction of water or oil flowing through that well respectively.

Since there are no situations where oil is injected into the reservoir, these equations simplify to:

$$\begin{aligned} q_w &= \sum_{i=1}^{n_I} Q_I^{(i)} \delta(\boldsymbol{x} - \boldsymbol{x}_I^{(i)}) - \sum_{j=1}^{n_P} \frac{\lambda_w}{\lambda_w + \lambda_o} Q_P^{(i)} \delta(\boldsymbol{x} - \boldsymbol{x}_P^{(i)}) \\ q_o &= -\sum_{j=1}^{n_P} \frac{\lambda_o}{\lambda_w + \lambda_o} Q_P^{(i)} \delta(\boldsymbol{x} - \boldsymbol{x}_P^{(i)}), \end{aligned} \tag{4.7}$$

In practice, wells operate in one of two modes: constant fluid flow rate, or constant bottom hole pressure. In the former case, the total fluid flow rate through the well is specified and the pressure at the bottom hole varies to maintain that flow rate. In the latter, the situation is reversed – the well maintains a constant pressure at its bottom hole and the total fluid flow rate through it varies.

Note that in Equation (4.7), only the total fluid flow rate through the well appears. This means that constant rate wells, whose fluid flow rate ($Q_I^{(i)}$ or $Q_P^{(j)}$, as applicable) are described

exactly by Equation (4.7). On the other hand, the dependence of the fluid flow through a constant pressure well requires modeling. One of the simplest modeling paradigms is to assume that the total fluid flow rate is proportional to the difference between the numerically computed gridblock pressure p and the bottom hole pressure p_{bh}. Therefore, $Q_I = J(p_{\text{bh}} - p)$ for an injector well and $Q_P = J(p - p_{\text{bh}})$ for a producer well. The constant of proportionality J depends on the well geometry and the numerical method being employed (we provide the exact expression in our implementation in Section 4.2.5). Finally, in our implementation, we approximate the Dirac-δ function centered at some location $\boldsymbol{x}_w$ with a Gaussian distribution whose mean is $\boldsymbol{x}_w$ and covariance matrix is $\boldsymbol{\Sigma}_w$, $\eta(\boldsymbol{x}_w, \boldsymbol{\Sigma}_w)$. Further, we assume that the injector wells always operate in constant pressure mode, whereas producer wells operate in constant rate mode. With these assumptions, the equations that describe the wells mathematically are:

$$\begin{aligned} q_w &= \sum_{i=1}^{n_I} J(p_{\text{bh}} - p)\eta(\boldsymbol{x}_I^{(i)}, \boldsymbol{\Sigma}_w) - \sum_{j=1}^{n_P} \frac{\lambda_w}{\lambda_w + \lambda_o} Q_P^{(i)} \eta(\boldsymbol{x}_P^{(j)}, \boldsymbol{\Sigma}_w) \\ q_o &= -\sum_{j=1}^{n_P} \frac{\lambda_o}{\lambda_w + \lambda_o} Q_P^{(i)} \eta(\boldsymbol{x}_P^{(j)}, \boldsymbol{\Sigma}_w) \end{aligned} \tag{4.8}$$

For easy reference, we summarize our reservoir model in the next sub-section.

4.2.4 Summary

Let there be n_f faults within the reservoir. Denoting each fault as Γ_i and its log-transmissibility m_i, the full set of equations governing flow within the fractured reservoir is:

$$
\begin{aligned}
\boldsymbol{v} &= -(\lambda_w + \lambda_o) K \nabla p \quad \text{in } \Omega, \\
\Bigg(\phi \left(c_r + (1 - S_w) c_o + S_w c_w \right) \frac{\partial p}{\partial t} + \nabla \cdot \boldsymbol{v} & \\
- \left[c_w \lambda_w + c_o \lambda_o \right] \frac{\boldsymbol{v} \cdot \boldsymbol{v}}{\lambda_t^2 K} \Bigg) &= q_w + q_o \qquad \text{in } \Omega \times (0, T], \\
\frac{\partial \phi \rho_w S_w}{\partial t} + \nabla \cdot \left[\frac{\rho_w \lambda_w \boldsymbol{v}}{\lambda_t} \right] &= \rho_w q_w \qquad \text{in } \Omega \times (0, T], \\
[\![\boldsymbol{v} \cdot \boldsymbol{n}_f^{(i)}]\!]_{\Gamma_i} &= 0 \qquad \text{in } \Gamma_i,\ i = 1, \ldots, n_f \\
\boldsymbol{v} \cdot \boldsymbol{n}_f^{(i)} - \exp\left(m^{(i)} \right) [\![p]\!]_{\Gamma_i} &= 0, \qquad \text{in } \Gamma_i,\ i = 1, \ldots, n_f \\
p &= p_0 \qquad \text{in } \Omega \times \{0\}, \\
S_w &= S_{w,0} \qquad \text{in } \Omega \times \{0\}, \\
\boldsymbol{v} \cdot \boldsymbol{n} &= 0 \qquad \text{in } \partial\Omega \times [0, T]
\end{aligned}
\tag{4.9}
$$

Here we've also introduced the necessary initial and boundary conditions. We've assumed that initial global pressure and water saturation are specified, say p_0 and $S_{w,0}$. At the boundaries, we've assumed a no flux boundary condition, $\boldsymbol{v} \cdot \boldsymbol{n} = 0$.

This PDE system can be viewed as an implicit relationship between the pressure, velocity, and saturation fields, $p, S_w, \boldsymbol{v}$, and the log-transmissibilities, $m_1, \ldots, m_{n_f}$. We will denote this implicit relationship as $c(\boldsymbol{u}, \boldsymbol{m}) = 0$, where $\boldsymbol{u}$ denotes the consolidated state variable, $\boldsymbol{u} = (p, S, \boldsymbol{v})$, and $\boldsymbol{m} \in \mathbb{R}^{n_f}$ is the vector of log-transmissibilities, $\boldsymbol{m} = [m_1, \ldots, m_{n_f}]^\top$.

The following section describes how we discretize and solve this PDE system numerically.

4.2.5 Numerical discretization.

We discretize the reservoir domain Ω with an unstructured triangular mesh in such a way that the cell edges conform to the faults Γ_i. To solve Equation (4.9), we use a mixed finite

element method for velocity and pressure, and a discontinuous Galerkin (DG) method for saturation. We use lowest-order Raviart-Thomas elements to discretize the velocity field and constant discontinuous Lagrange elements to discretize the pressure and saturation fields. Our DG implementation uses upwind flux at the cell facets. The well-index J corresponding to our spatial discretization scheme has the following expression [97]:

$$J = \frac{2\pi\left(\lambda_w + \lambda_o\right)K}{\log\left(\frac{2\sqrt{2}}{3}h\right) - \frac{\pi}{6}}, \tag{4.10}$$

where h is the minimum cell diameter of the mesh. We use a backward Euler scheme for time integration. We will use the notation $\mathbf{c}_n(\mathbf{u}_n, \mathbf{u}_{n-1}, \boldsymbol{m})$ to refer to the system of equations arising from the space-time discretization of the continuous system $c(\boldsymbol{u}, \boldsymbol{m}) = 0$. Here, n denotes the n-th iteration of the time-marching scheme corresponding to $t = t_n$ and $\mathbf{u}_n$ denotes the spatially discretized state variable $\boldsymbol{u}$ at time t_n. At each n, $\mathbf{c}_n(\mathbf{u}_n, \mathbf{u}_{n-1}, \boldsymbol{m})$ represents a non-linear system of equations for the unknown $\boldsymbol{u}_n$. For this, we use a trust-region Newton method. Our solver software uses `FEniCS` [6] to discretize the PDEs, and `PETSc` [12] for efficient non-linear and linear solvers. We use `gmsh` for automatic mesh generation [37].

The reservoir flow model and numerics discussed in this section enable us to solve the forward problem – given fault transmissibilities, predict the state (including pressure) of the fluids within the reservoir. Next, we describe how we formulate and solve the inverse problem – given observations of the fluid pressure, predict the transmissibilities that led to those observations.

4.3 The inverse problem

As we mentioned in Section 4.1, we pose the problem of inferring fault transmissibilities from pressure observations within the Bayesian framework. In this section, we provide details of our Bayesian inference setup. We also review Markov Chain Monte Carlo methods to generate draws from the posterior distribution obtained at the end of the Bayesian inference workflow. We conclude this section with a review of Laplace's approximation of the posterior as a cheaper alternative to quantify uncertainty.

4.3.1 Bayesian inference setup

Let there be n_w wells in the reservoir. We denote with $\boldsymbol{y}_i$ the pressure observations recorded by all wells at time τ_i, $i = 1, \ldots, n_o$, $\boldsymbol{y}_i \in \mathbb{R}^{n_w}$. If $\boldsymbol{m} \in \mathbb{R}^{n_f}$ denotes the vector of the fault log-transmissibilities, then, from Bayes' theorem, we have:

$$\pi_{\text{post}}(\boldsymbol{m}|\boldsymbol{y}_1, \ldots, \boldsymbol{y}_{n_o}) \propto \pi_{\text{like}}(\boldsymbol{y}_1, \ldots, \boldsymbol{y}_{n_o}|\boldsymbol{m})\pi_{\text{prior}}(\boldsymbol{m}) \tag{4.11}$$

In Equation (4.11), $\pi_{\text{prior}}(\boldsymbol{m})$ is the prior distribution, which expresses prior assumptions regarding the uncertainty in $\boldsymbol{m}$ before production history is recorded, and $\pi_{\text{like}}(\boldsymbol{y}|\boldsymbol{m})$ is the likelihood distribution, which encodes the likelihood of observing $\boldsymbol{y}$ given some candidate log-transmissibilities $\boldsymbol{m}$. The product of the prior and the likelihood distributions is the posterior distribution $\pi_{\text{post}}(\boldsymbol{m}|\boldsymbol{y})$, which reflects updated uncertainties after accounting for the production history $\boldsymbol{y}$. The posterior distribution quantifies uncertainties in the transmissibilities in the following way – to every set $\mathcal{M} \subset \mathbb{R}^{n_f}$, it assigns a probability that the true log-transmissibilities are contained in $\mathcal{M}$. This probability is simply $\int_{\mathcal{M}} \pi_{\text{post}}(\boldsymbol{m}|\boldsymbol{y}_1, \ldots, \boldsymbol{y}_{n_o})\mathrm{d}\boldsymbol{m}$.

In this work, we model prior uncertainties in $\boldsymbol{m}$ using a Gaussian distribution with specified mean $\boldsymbol{m}_{\text{prior}}$ and covariance $\boldsymbol{\Sigma}_{\text{prior}}$, $\pi_{\text{prior}}(\boldsymbol{m}) = \mathcal{N}(\boldsymbol{m}_{\text{prior}}, \boldsymbol{\Sigma}_{\text{prior}})$. We further assume that

pressure observations recorded at the wells at time τ_i are contaminated with additive random noise $\boldsymbol{\beta}_i$. If $\mathcal{G}_i(\boldsymbol{m})$ is the map from the log-transmissibilities to the well pressures at time τ_i, then this implies $\boldsymbol{y}_i = \mathcal{G}_i(\boldsymbol{m}) + \boldsymbol{\beta}_i$. We model $\boldsymbol{\beta}_i$ as a Gaussian random variable whose mean is zero, and whose covariance $\boldsymbol{\Sigma}_{\text{noise}}$ is such that observations from distinct wells are statistically independent, while observations originating from a particular well are corrupted with noise of the same magnitude, say, σ_j^2 for well j. Then, the likelihood distribution becomes:

$$\pi_{\text{like}}(\boldsymbol{m}|\boldsymbol{y}_1, \ldots, \boldsymbol{y}_{n_o}) \propto \exp\left(\sum_{i=1}^{n_o} -\frac{1}{2}\|\boldsymbol{y}_i - \mathcal{G}_i(\boldsymbol{m})\|^2_{\boldsymbol{\Sigma}^{-1}_{\text{noise}}}\right), \tag{4.12}$$

where $\boldsymbol{\Sigma}^{-1}_{\text{noise}} = \texttt{diag}[\sigma_1^2, \ldots, \sigma_{n_w}^2]$.

The map $\mathcal{G}_i(\boldsymbol{m})$ can be re-expressed in terms of the state variable $\boldsymbol{u}$ as $\mathcal{G}_i(\boldsymbol{m}) = \mathcal{B}\boldsymbol{u}(\tau_i; \boldsymbol{m})$, where $\boldsymbol{u}(\tau_i; \boldsymbol{m})$ denotes state variable corresponding to the parameter $\boldsymbol{m}$ at time τ_i, and $\mathcal{B}$ is the operator that maps the state variable to the pressure at the well locations. In the rest of this chapter, we will use this alternative definition. Then, owing to the likelihood and prior choices, the posterior has the following form:

$$\pi_{\text{post}}(\boldsymbol{m}|\boldsymbol{y}_1, \ldots, \boldsymbol{y}_{n_o}) \propto \exp\left(\sum_{i=1}^{n_o} -\frac{1}{2}\|\boldsymbol{y}_i - \mathcal{B}\boldsymbol{u}(\tau_i; \boldsymbol{m})\|^2_{\boldsymbol{\Sigma}^{-1}_{\text{noise}}} - \frac{1}{2}\|\boldsymbol{m} - \boldsymbol{m}_{\text{prior}}\|^2_{\boldsymbol{\Sigma}^{-1}_{\text{prior}}}\right) \tag{4.13}$$

One last modification to the definition above is necessary. In practice, we don't have access to the continuous state variable – we only have at our disposal its discretized (both in space and time) approximation $\mathbf{v}_n$, obtained by solving the abstract discrete PDE system $\mathbf{c}_n(\mathbf{u}_n, \mathbf{u}_{n-1}, \boldsymbol{m}) = 0$. The posterior distribution that we must work with is therefore:

$$\pi_{\text{post}}(\boldsymbol{m}|\boldsymbol{y}_1, \ldots, \boldsymbol{y}_{n_o}) \propto \exp\left(\sum_{n=1}^{n_o} -\frac{1}{2}\|\boldsymbol{y}_n - \mathbf{B}\mathbf{v}_i\|^2_{\boldsymbol{\Sigma}^{-1}_{\text{noise}}} - \frac{1}{2}\|\boldsymbol{m} - \boldsymbol{m}_{\text{prior}}\|^2_{\boldsymbol{\Sigma}^{-1}_{\text{prior}}}\right) \tag{4.14}$$

where we've replaced the continuous linear operator $\mathcal{B}$ with its discretized counterpart $\mathbf{B}$, and assumed that the observation times coincide with the time steps of the time-marching scheme, $\tau_i = t_i$. Consequently, our assimilation window is $[0, t_{n_o}]$. For notational convenience, we will denote the end of the assimilation window t_{n_o} by T_{obs}. In the rest of this chapter, whenever we use π_{post}, we imply the discretized posterior in Equation (4.14).

In an uncertainty quantification workflow, often the end goal is to estimate summary statistics – either of the uncertain parameters $\boldsymbol{m}$ themselves, or of decision-relevant quantities-of-interest that depend on $\boldsymbol{m}$, say $f(\boldsymbol{m})$. These statistics, which include the mean, variance, and event-probabilities, are expressed as expectations with respect to the posterior. Even though the likelihood and prior distributions are Gaussian, the posterior in Equation (4.14) is non-Gaussian because the state variable $\mathbf{u}_n$ implicitly depends on the log-transmissibilities $\boldsymbol{m}$ through a non-linear system of equations. The non-Gaussianity of the posterior renders the analytical calculation of these expectations impossible, and although quadrature methods can in principle be used to numerically estimate these expectations, they are effective only up to a handful of dimensions. The standard approach is to use the Monte Carlo method, where the expectation is approximated with a sample mean using draws $\{\boldsymbol{m}_i\}_{i=1}^N$ from the posterior distribution. The Law of Large Numbers guarantees that the sample average converges to the true expectation as the number of samples grows to infinity.

Yet again, the non-Gaussianity of the posterior presents a challenge – drawing independent samples from the posterior directly isn't usually possible. In order to generate samples $\{\boldsymbol{m}_i\}_{i=1}^N$ from the posterior, we employ a Markov Chain Monte Carlo (MCMC) algorithm. MCMC algorithms generate a Markov chain whose stationary distribution is set to be the target distribution from which samples are desired, which in this case is $\pi_{\text{post}}(\boldsymbol{m}|\boldsymbol{y}_1, \ldots, \boldsymbol{y}_{n_o})$. Once stationarity is achieved, the Markov chain yields correlated samples that are approximately distributed according to $\pi_{\text{post}}(\boldsymbol{m}|\boldsymbol{y}_1, \ldots, \boldsymbol{y}_{n_o})$. MCMC algorithms only require the ability to evaluate the target distribution up to a normalizing constant (some algorithms

additionally use gradients of the target), and hence are a natural choice for generating samples from intractable distributions. Note that in our context, evaluating the target distribution $\pi_{\text{post}}(\boldsymbol{m}|\boldsymbol{y}_1, \ldots, \boldsymbol{y}_{n_o})$ requires evaluating the likelihood distribution $\pi_{\text{post}}(\boldsymbol{y}_1, \ldots, \boldsymbol{y}_{n_o}|\boldsymbol{m})$, which in turn requires simulating the PDE system in Equation (8) from $t = 0$ to $t = t_{n_o}$.

We use the preconditioned Crank-Nicholson (pCN) algorithm [25] to explore and sample from the posterior. The pCN algorithm only differs slightly in implementation from a vanilla Random Walk Metropolis method Hastings (RWMH), but has the desirable property of possessing a proposal which is reversible with respect to the prior. This means that in the trivial case that the likelihood is zero, the pCN algorithm produces exact samples from the posterior, a property that does not hold for the RWMH algorithm.

The need for the elaborate sampling algorithms described above stems primarily from the non-Gaussianity of the posterior. Such algorithms, can, in principle, be avoided if the posterior is approximated with a Gaussian distribution. We describe, in the next sub-section, such an approximation, and the consequences of using it.

4.3.2 Gaussianizing the posterior

One way to construct a Gaussian approximation of the posterior is to construct a second-order Taylor series expansion of the negative log-posterior at its mode. The mode, also known as the Maximum *A Posteriori* point, is where the posterior density is the highest. Therefore, in the Taylor series expansion, the gradient of the negative log-posterior vanishes and we're left with (up to a constant):

$$-\log \pi_{\text{post}}(\boldsymbol{m}|\boldsymbol{y}_1, \ldots, \boldsymbol{y}_{n_o}) \approx \frac{1}{2} (\boldsymbol{m} - \boldsymbol{m}_{\text{MAP}})^\top \boldsymbol{H}_{\text{MAP}} (\boldsymbol{m} - \boldsymbol{m}_{\text{MAP}}) \tag{4.15}$$

where $\boldsymbol{m}_{\text{MAP}}$ denotes the MAP point, and $\boldsymbol{H}_{\text{MAP}}$ denotes the Hessian matrix of $-\log \pi_{\text{post}}(\boldsymbol{m}|\boldsymbol{y}_1, \ldots, \boldsymbol{y}_{n_o})$ at $\boldsymbol{m}_{\text{MAP}}$. This implies, $\pi_{\text{post}} \approx \pi_{\text{laplace}}$, where

$$\pi_{\text{laplace}}(\boldsymbol{m}) \propto \exp\left(-\frac{1}{2}\|\boldsymbol{m}-\boldsymbol{m}_{\text{MAP}}\|^2_{\boldsymbol{H}_{\text{MAP}}}\right) \tag{4.16}$$

The extent to which π_{laplace} approximates the true posterior π_{post} depends on how non-linear the parameter-to-observable map $\mathcal{G}_i(\boldsymbol{m})$ (which we take to be $\boldsymbol{B}(\boldsymbol{v}_i;\boldsymbol{m})$) is – the closer this map is to being nearly linear, the better the approximation. Note that this includes the situation where the $\boldsymbol{G}_i(\boldsymbol{m})$ is nearly constant for some directions of the parameter space. These will be directions that are poorly informed by the data. The posterior distribution in these directions will resemble the prior, and this resemblance will be well-captured by the Laplace approximation.

Two ingredients are necessary to construct the Laplace distribution – the MAP point, and the Hessian matrix of $-\log\pi_{\text{post}}(\boldsymbol{m}|\boldsymbol{y}_1,\ldots,\boldsymbol{y}_{n_o})$. The MAP point, by definition, maximizes the posterior distribution, or equivalently, minimizes $-\log\pi_{\text{post}}(\boldsymbol{m}|\boldsymbol{y}_1,\ldots,\boldsymbol{y}_{n_o})$:

$$\begin{aligned}\boldsymbol{m}_{\text{MAP}} = \underset{\boldsymbol{m}\in\mathbb{R}^{n_f}}{\arg\min} \sum_{i=1}^{n_o} \frac{1}{2}\|\boldsymbol{y}_i-\mathbf{B}\mathbf{u}_i\|^2_{\boldsymbol{\Sigma}^{-1}_{\text{noise}}} + \frac{1}{2}\|\boldsymbol{m}-\boldsymbol{m}_{\text{prior}}\|^2_{\boldsymbol{\Sigma}^{-1}_{\text{prior}}} \\ \text{subject to } \mathbf{c}_n(\mathbf{u}_n,\mathbf{u}_{n-1},\boldsymbol{m})=\mathbf{0}, n=1,\ldots,n_o\end{aligned} \tag{4.17}$$

Because state-of-the-art algorithms to solve optimization problems (like the one in Equation (4.17)) rely on derivatives of the objective function, computing $\boldsymbol{m}_{\text{MAP}}$ and $\boldsymbol{H}_{\text{MAP}}$ are intertwined. For instance, Newton's method uses both first- and second-order derivatives to arrive at the local extremum. To compute derivatives of $-\log\pi_{\text{post}}$, we invoke the Lagrangian formalism. However, before we describe our approach any further, a remark regarding our notation is in order. In what follows, we will denote the Jacobian matrix of a vector-valued function of several vector-valued variables, say, $\boldsymbol{c}(\boldsymbol{x},\boldsymbol{y})$, by $\partial\boldsymbol{c}/\partial\boldsymbol{x}$, whose $(i,j)^{\text{th}}$ entry is $\partial c_i/\partial x_j$. The second-derivative of such a function is a third-rank tensor, which we denote with $\partial^2\boldsymbol{c}/\partial\boldsymbol{x}\partial\boldsymbol{y}$, and whose $(i,j,k)^{\text{th}}$ entry is:

$$\left(\frac{\partial^2 \mathbf{c}}{\partial \boldsymbol{x} \partial \boldsymbol{y}}\right)_{ijk} \equiv \frac{\partial}{\partial x_k}\left(\frac{\partial c_i}{\partial y_j}\right) \tag{4.18}$$

Then, introducing the Lagrange multipliers, or adjoint variables, $\mathbf{p}_n$, $n = 1, \ldots, n_o$, the Lagrangian for this constrained optimization problem is:

$$\begin{aligned}\mathcal{L}(\mathbf{u}_1, \ldots, \mathbf{u}_n, \boldsymbol{m}, \mathbf{p}_1, \ldots, \mathbf{p}_n) = &\sum_{i=1}^{n_o} \frac{1}{2}\|\boldsymbol{y}_i - \mathbf{B}\mathbf{u}_i\|^2_{\boldsymbol{\Sigma}^{-1}_{\text{noise}}} + \frac{1}{2}\|\boldsymbol{m} - \boldsymbol{m}_{\text{prior}}\|^2_{\boldsymbol{\Sigma}^{-1}_{\text{prior}}} \\ &+ \sum_{i=1}^{n_o} \mathbf{p}_n^\top \mathbf{c}_n(\mathbf{u}_n, \mathbf{u}_{n-1}, m)\end{aligned} \tag{4.19}$$

The gradient of the objective function, $\boldsymbol{g}$, is obtained by computing the first variation of $\mathcal{L}$ with respect $\boldsymbol{m}$, which is (in strong form):

$$\boldsymbol{g} = \boldsymbol{\Sigma}^{-1}_{\text{prior}}(\boldsymbol{m} - \boldsymbol{m}_{\text{prior}}) + \sum_{i=1}^{n_o} \mathbf{p}_n^\top \frac{\partial \mathbf{c}_n}{\partial \boldsymbol{m}}, \tag{4.20}$$

The adjoint and state variables $\mathbf{p}_n$ and $\mathbf{u}_n$ are found by setting the first variation of $\mathcal{L}$ with respect to $\mathbf{u}_n$ and $\mathbf{p}_n$ to zero, leading to (again, in strong form):

$$\mathbf{c}_n(\mathbf{u}_n, \mathbf{u}_{n-1}, \boldsymbol{m}) = \mathbf{0} \tag{4.21a}$$

$$\begin{aligned}\left(\frac{\partial \mathbf{c}_n}{\partial \mathbf{u}_n}\right)^\top \mathbf{p}_n &= -\left(\frac{\partial \mathbf{c}_{n+1}}{\partial \mathbf{u}_n}\right)^\top \mathbf{p}_{n+1} - \mathbf{B}^\top \boldsymbol{\Sigma}_{\text{noise}}\left(\mathbf{B}\mathbf{u}_n - \boldsymbol{y}_n\right), \; n = 1, \ldots, n_o - 1 \\ \left(\frac{\partial \mathbf{c}_{n_o}}{\partial \mathbf{u}_{n_o}}\right)^\top \mathbf{p}_{n_o} &= -\mathbf{B}^\top \boldsymbol{\Sigma}_{\text{noise}}\left(\mathbf{B}\mathbf{u}_{n_o} - \boldsymbol{y}_{n_o}\right)\end{aligned} \tag{4.21b}$$

Equation (4.21a) is nothing but the discretized forward problem. Equation (4.21b) is the adjoint equation. Notice how, starting from $n = n_o$, the adjoint variable corresponding to

step n, $\mathbf{p}_n$, depends on the adjoint variable at step $n+1$, $\mathbf{p}_{n+1}$, as if it's evolving backwards in time. Another notable feature of the adjoint equation is that it's linear, even though the discrete forward problem is non-linear. Therefore, computing the gradient of the objective function requires solving the discretized PDE system to obtain the state variable $\mathbf{u}_n$, and in addition, solving a linear adjoint equation, to obtain the adjoint variables $\mathbf{p}_n$.

We compute the Hessian of the objective function in a similar manner, by defining the meta-Lagrangian functional:

$$\begin{aligned}\mathcal{L}^H = &(\boldsymbol{m} - \boldsymbol{m}_{\text{prior}})^\top \boldsymbol{\Sigma}_{\text{prior}}^{-1} \tilde{\boldsymbol{m}} + \sum_{i=1}^{n_o} \mathbf{p}_n^\top \frac{\partial \mathbf{c}_n}{\partial \boldsymbol{m}} \tilde{\boldsymbol{m}} \\ &+ \sum_{i=1}^{n_o} \tilde{\mathbf{p}}_n^\top \mathbf{c}_n(\mathbf{u}_n, \mathbf{u}_{n-1}, \boldsymbol{m}) \\ &+ \sum_{i=1}^{n_o} \tilde{\mathbf{u}}_n^\top \left[\left(\frac{\partial \mathbf{c}_n}{\partial \mathbf{u}_n} \right)^\top \mathbf{p}_n + \left(\frac{\partial \mathbf{c}_{n+1}}{\partial \mathbf{u}_n} \right)^\top \mathbf{p}_{n+1} + \mathbf{B}^\top \boldsymbol{\Sigma}_{\text{noise}} \left(\mathbf{B}\mathbf{u}_n - \boldsymbol{y}_n \right) \right] \\ &+ \tilde{\mathbf{u}}_{n_o}^\top \left[\left(\frac{\partial \mathbf{c}_{n_o}}{\partial \mathbf{u}_{n_o}} \right)^\top \mathbf{p}_{n_o} + \mathbf{B}^\top \boldsymbol{\Sigma}_{\text{noise}} \left(\mathbf{B}\mathbf{u}_{n_o} - \boldsymbol{y}_{n_o} \right) \right]\end{aligned} \tag{4.22}$$

The first term in the meta-Lagrangian is the action of $\boldsymbol{g}$ along some direction $\tilde{\boldsymbol{m}}$ – this is the function whose gradient we desire, loosely speaking. The rest of the terms arise from the constraints which the variables $\mathbf{u}_n$ and $\mathbf{p}_n$ must obey – these are the discrete forward and adjoint equations in Equation (4.21). The so-called incremental adjoint and forward variables, $\tilde{\mathbf{p}}_n$ and $\tilde{\mathbf{u}}_n$, are the Lagrange multipliers that correspond to these constraints. The action of the Hessian along some direction $\tilde{\boldsymbol{m}}$ is then (in weak form):

$$\begin{aligned}\hat{\boldsymbol{m}}^\top \boldsymbol{H} \tilde{\boldsymbol{m}} = \hat{\boldsymbol{m}}^\top \boldsymbol{\Sigma}_{\text{prior}} \tilde{\boldsymbol{m}} &+ \sum_{n=1}^{n_o} \left(\frac{\partial^2 \mathbf{c}_n}{\partial \boldsymbol{m}^2} \right) : (\mathbf{p}_n \circ \tilde{\boldsymbol{m}} \circ \hat{\boldsymbol{m}}) + \sum_{n=1}^{n_o} \tilde{\mathbf{p}}_n^\top \frac{\partial \mathbf{c}_n}{\partial \boldsymbol{m}} \hat{\boldsymbol{m}} \\ &+ \sum_{n=1}^{n_o} \left(\frac{\partial^2 \mathbf{c}_n}{\partial \boldsymbol{m} \partial \mathbf{u}_n} \right) : (\mathbf{p}_n \circ \tilde{\mathbf{u}}_n \circ \hat{\boldsymbol{m}}) \left(\frac{\partial^2 \mathbf{c}_{n+1}}{\partial \boldsymbol{m} \partial \mathbf{u}_n} \right) : (\mathbf{p}_{n+1} \circ \tilde{\mathbf{u}}_n \circ \hat{\boldsymbol{m}}) \\ &+ \left(\frac{\partial^2 \mathbf{c}_{n_o}}{\partial \boldsymbol{m} \partial \mathbf{u}_{n_o}} \right) : (\mathbf{p}_{n_o} \circ \tilde{\mathbf{u}}_{n_o} \circ \hat{\boldsymbol{m}}) \quad \forall \, \hat{\boldsymbol{m}} \in \mathbb{R}^{n_f},\end{aligned} \tag{4.23}$$

where $\circ$ is the vector outer product and : denotes the tensor double dot product: $\boldsymbol{A} : \mathbf{B} = \sum_{i,j,k} A_{ijk} B_{ijk}$.

Setting the first variation of the meta-Lagrangian with respect to the state $\mathbf{u}_n$ and adjoint variables $\mathbf{p}_n$ to zero yields the equations governing $\tilde{\mathbf{p}}$ and $\tilde{\mathbf{u}}_n$, respectively. These are the so-called incremental adjoint and incremental forward equations. These equations, which we omit here for brevity, are both linear. Therefore, in order to obtain the Hessian action in some direction, we must solve, in addition to the discrete forward and adjoint equations, the incremental forward and adjoint equations.

Our approach above, where we compute the derivatives of the discretized objective function and constraints, and then perform optimization is known in literature as the discretize-then-optimize approach [41]. In contrast, the optimize-then-discretize approach involves first analytically deriving the optimality conditions necessary to solve the continuous counterpart of Equation (4.17) (that is, involving the continuous state variable $\boldsymbol{u}$ instead of the discretized $\mathbf{u}$) and then discretizing them. The OTD approach can yield derivatives that are inconsistent with the discrete forward problem, and although DTO and OTD are equivalent for a standard Galerkin method, they may not necessarily be equivalent for a discontinuous Galerkin method. By using a discretize-then-optimize approach, we ensure that the derivatives are consistent with the discrete forward problem and the resulting Hessian matrices are symmetric to machine precision.

In our software, we use the symbolic differentiation feature in `FEniCS` to compute the first and second-order derivatives of $\mathbf{c}_n$ (terms such as $\partial \mathbf{c}_n / \partial \boldsymbol{m}$, $\partial^2 \mathbf{c}_n / \partial \boldsymbol{m}^2$, or $\partial^2 \mathbf{c}_n / \partial \boldsymbol{m} \partial \mathbf{c}_n$). We solve the linear equations arising at each time-step of the adjoint, and the incremental forward and adjoint equations using a direct linear solver. To compute the MAP point, we feed the gradient and Hessian action computed above to a Newton-CG algorithm [90], as implemented in `hIPPYlib` [89], a Python based inverse problem library. The `hIPPYlib` implementation uses Armijo line search to achieve globalization and Steihaug criterion to avoid negative curvature. Early iterations of the Newton-CG algorithm use the Gauss-Newton Hessian to avoid the indefinite Hessian matrices far from the extremum.

Finally, to construct π_{laplace}, we assemble $\boldsymbol{H}_{\text{MAP}}$ by simply computing it's action on all canonical basis vectors in $\mathbb{R}^{n_f}$. This approach requires as many incremental forward and incremental adjoint solves as there are parameters (n_f in this case) and doesn't scale to situations where the parameter space is really high-dimensional. It's possible to skirt this issue using low-rank approximations of the prior-preconditioned data-misfit Hessian [46], but our parameter spaces aren't large enough to necessitate such an approach.

In this section, we described our approach for inferring log-transmissibilities $\boldsymbol{m}$ from production data $\boldsymbol{y}_1, \ldots, \boldsymbol{y}_{n_o}$. Often, the end goal in an uncertainty quantification workflow is to propagate these uncertainties to one or many decision-relevant quantity-of-interests. We describe the QoIs we use in the work in the next section.

4.4 Quantity of Interest

In this work, we formulate two representative quantities-of-interest, motivated by decision-relevant quantities that a practicing reservoir operator may wish to predict. Both quantities are based on the Net Present Value (NPV) of the reservoir, an indicator routinely employed in reservoir operation and management to assess the financial feasibility of a project. The NPV is defined as the difference between the *future* value of all projected earnings and any

investments. Assuming that the primary revenue source for an oil reservoir is profits after oil sales, it follows that the Net Present Value of the reservoir should be:

$$V_{\text{net}} = \int_{T_{\text{obs}}}^{T} c_{\text{oil}}(t) Q_{\text{oil}}(t) e^{-r(t-T_{\text{obs}})} \mathrm{d}t - c_{\text{in}}, \tag{4.24}$$

where Q_{oil} is the total oil production rate of the reservoir at time t, r is the discount rate, $c_{\text{oil}}(t)$ is the projected cost of oil at time t, and c_{in} are any investments made.

Our first QoI is the discounted future oil production:

$$V = \int_{T_{\text{obs}}}^{T} Q_{\text{oil}}(t) e^{-r(t-T_{\text{obs}})} \mathrm{d}t, \tag{4.25}$$

which is identical to the NPV assuming unit oil price and ignoring c_{in}. Note that our prediction window $[T_{\text{obs}}, T]$ begins after the data assimilation $[0, T_{\text{obs}}]$ window ends.

For our second Quantity-of-Interest, we consider the situation where an infill well needs to be drilled at some location $\boldsymbol{x}_{\text{infill}}$ at time T_{obs}. A natural way to assess whether drilling the infill well is a feasible investment or not is to compare the Net Present Value of the reservoir at time T_{obs} with and without the infill well operational. As a surrogate for the NPV, we will instead compute the relative change in the discounted future oil production, with and without the infill. Hence, our second QOI is:

$$Q_{\text{excess}} = \frac{V_{\text{infill}} - V}{V}, \tag{4.26}$$

where V_{infill} is the discounted future oil production with an infill well at $\boldsymbol{x}_{\text{infill}}$ and V without. We estimate the time integral in Equation (4.25) using a right Riemann sum, as follows:

$$V = \sum_{i=n_o+1}^{N} Q_{\text{oil}}(t_i) e^{-r(t_i-T_{\text{obs}})} \Delta t. \tag{4.27}$$

The time step Δt is equal to the time-step we use in the forward simulation. With this, we conclude our review of the background theory and methods. In the next section, we describe our numerical experiments and results.

4.5 Experiments

Our goal in this chapter is to report uncertainties in the inferred transmissibilities and QoIs, and explore how these uncertainties change under different reservoir conditions. Systematically exploring the role of each free parameter that appears in the forward and inverse problem is a formidable task, and one that we will not attempt to undertake. Instead, we restrict our attention to the following scenarios:

- In our first experiment, we consider a reservoir containing two faults and investigate the effect of varying their relative arrangement on posterior uncertainties.
- In our second experiment, we consider a more realistic situation where the location of only a few major faults is known with certainty. The presence of smaller faults is suspected, but their location and number are unknown. Here we ask whether production data can help pinpoint the location of the smaller faults and the nature of the uncertainties that result.

The forward and inverse problem setup for both experiments share several commonalities, which we describe next.

Forward problem In both experiments, we assume that:

- the reservoir has square shape with length L,
- the porosity ϕ is uniform,

- initially, the reservoir is at some pressure p_0 and flooded with oil, $S_{w,o} = 0$,
- injection wells operate at the same constant bottom-hole pressure p_{bh}, while production wells operate at identical constant rate Q,
- all wells have the same radius r_{well},
- the Gaussian distribution we use to represent wells has covariance $(2h)^2\boldsymbol{I}$, where h is the minimum cell diameter of the mesh,
- all faults in the reservoir have the same thickness d_f and length L_f,
- the discount rate r used to predict the Quantities-of-Interest r is the same.

The values for the parameters above, as well as physical properties of the fluids that we use are provided in Table 4.2. For the solution of the nonlinear system of equations at each time-step, we set an absolute tolerance of 10^{-10} and relative tolerance of 10^{-8}. In order to specify the mesh size in each experiment, we enforce an element size of $L/32$ at the reservoir corners and end points of each fault. The element sizes in the rest of the domain are then interpolated from these specified values.

Inverse problem In each experiment, the prior distribution is $\mathcal{N}(\boldsymbol{m}_0, 49\boldsymbol{I})$, where $\boldsymbol{m}_0 = [m_0, \ldots, m_0]^\top \in \mathbb{R}^{n_f}$ and m_0 represents the log-transmissibility which leads to equal fault and background permeabilities Equation (4.5). This way, the prior is equivocal about whether the faults are more sealing than the background or not. Moreover, for each fault, approximately 95% of the prior probability mass is between $K_f/K = 10^{-6}$ and $K_f/K = 10^6$.

For both experiments we select a set of ground-truth log-transmissibilities for the faults, using which we generate synthetic production data. To this synthetic data, we add white noise whose magnitude is 1% of the maximum pressure observed at each well. The observation

Parameter	Value
L	500 m
ϕ	0.3
p_0	10^7 Pa
p_b	1.2×10^7 Pa (120 bar)
d_f	0.5 m
r_{well}	0.28 m (0.5 ft)
r	equivalent to 10% per annum
c_w	4.35×10^{-10} Pa^{-1}
c_o	4.35×10^{-10} Pa^{-1}
c_r	1.45×10^{-10} Pa^{-1}
μ_w	3×10^{-4} Pa $\cdot$ s (0.3 cP)
μ_o	6×10^{-4} Pa $\cdot$ s (0.6 cP)

Table 4.2: *Common physical parameters used in our experiments.*

time T_{obs} is that time when net oil production falls to 50% of the peak production with the ground-truth log-transmissibilities. The prediction window for the discounted future oil production begins at $t = T_{\text{obs}}$, and ends when the water-cut reaches around 75%. When computing the MAP point, we terminate the Newton-CG algorithm when either the norm of the gradient falls below 10^{-6}, either in absolute terms, or relative to its initial value. Finally, a note regarding our plots – although the fault log-transmissibilities are our inference targets, in our plots, we report uncertainties in $\log K_{f,i}/K$, where $K_{f,i}$ is the permeability (normal to the fault) of the i-th fault. The log-transmissibilities for each fault m_i and $\log K_{f,i}/K$ are equivalent up to a constant (Equation (4.5)), but $\log K_{f,i}/K$ directly conveys the sealing capacity of the fault and is much easier to interpret. We emphasize that since the two differ only by a constant, this doesn't transform the uncertainties in any way. Any conclusions we make regarding one directly apply to the other.

Next, we describe our experiments in detail.

4.5.1 Effect of fault geometry and placement

Purpose To study how the relative placement of the faults affects:

- the uncertainties in the fault transmissibilities themselves, and,
- uncertainty in the discounted future oil production V.

Setup In addition to the setup described at the beginning of this section, we prescribe a constant background permeability $K = 100$ mD. Further, we assume that the wells are arranged in an inverted nine-spot pattern, with the injection well operating at constant bottom-hole pressure, $p_{\text{bh}} = 1.2 \times 10^7$ Pa, and production wells operating at a constant rate, $Q = 0.0001$ m^3/s (assuming a nominal reservoir height of 1m).

Next, we assume that the reservoir contains two equal-length parallel faults which make an angle θ with the x_1-axis and whose centers are separated by an equal distance $L_c/2$ from the center of the reservoir (see Figure 4.3 for a schematic of the reservoir). Clearly, θ and L_c parameterize relative fault placement. We generate different fault arrangements by varying θ and L_c, and observe how uncertainties in the fault log-transmissibilities and the future discounted oil production are affected. We try 3 different values for $\theta : [0°, 40°, 140°]$, and for each value of θ, set 4 different values for $L_c : [0.2L, 0.4L, 0.6L, 0.8L]$.

For each case, the time-step is 4.95 days. The duration of the assimilation window, $[0, T_{\text{obs}}]$ varies from 1603 to 2207 days. For this experiment, we use the future discounted production V (Equation (4.25))as the Quantity-of-Interest. The prediction window $[T_{\text{obs}}, T]$ ranges an extra 1747 to 2618 days after T_{obs}.

Results. Characterizing posterior uncertainty for each independent (θ, L_c) would not only be computationally arduous, but also intractable to report. Instead, we begin by comparing the MAP estimate of the log-transmissibilities $\boldsymbol{m}_{\text{MAP}}$ with the chosen ground-truth value $\boldsymbol{m}_{\text{true}}$. If the relative error between $\boldsymbol{m}_{\text{MAP}}$ and $\boldsymbol{m}_{\text{true}}$ exhibits distinct trends, we can reduce the computational expense by performing MCMC only on the representative θ, L_c combination.

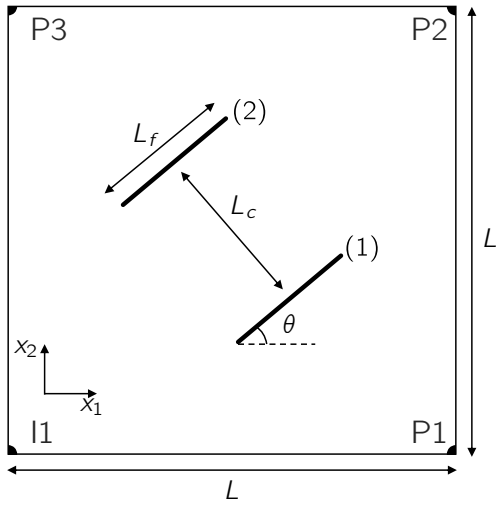

Figure 4.3: *To study the effect of relative fault placement, we parameterize fault placement using two variables: the angle both faults make with the x_1-axis θ, and the distance between the faults L_c.*

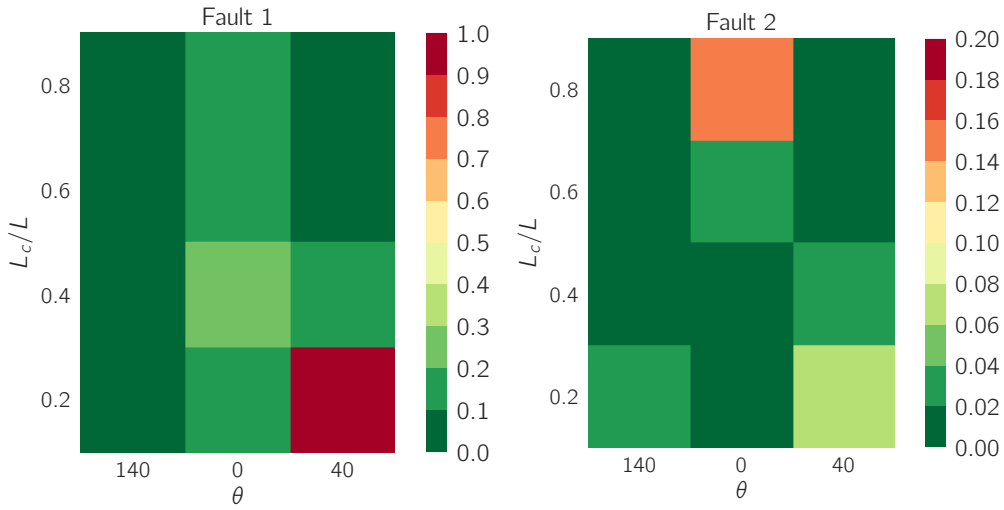

Figure 4.4: *Relative error between the ground-truth and MAP estimates of the fault transmissibilities at varying L_c (distance between the faults) and θ (angle with the x_1 axis), using the template reservoir shown in Figure 4.3.*

Figure 4.4 reports the relative error between the MAP estimate of the fault transmissibility and its true value for each θ, L_c combination, revealing that:

1. When $\theta = 40°$ and L_c is large, and when $\theta = 140°$, irrespective of L_c, $\boldsymbol{m}_{\text{MAP}}$ is very close to $\boldsymbol{m}_{\text{true}}$.

2. When $\theta = 40°$ the error is worst when L_c is smallest.

3. Finally, in all cases except $\theta = 0, c = 0.8L$, at least one of the faults is recovered to within 10%. When $\theta = 0$ and $L_c = 0.8L$, the error in fault 1 is 10.3%, and that in fault 2 is 15.1%.

We postulate that the small difference between $\boldsymbol{m}_{\text{MAP}}$ and $\boldsymbol{m}_{\text{true}}$ when $\theta = 140°$ is because the flow is forced to meet the faults head-on, leading to a more sensitive dependence of the observations on the fault transmissibilities. Although the flow doesn't meet the faults head-on when $\theta = 40°$ and L_c is large, we attribute the small difference between $\boldsymbol{m}_{\text{MAP}}$ and $\boldsymbol{m}_{\text{true}}$ in this case to the proximity between the faults and the observation locations. Owing to the closeness between $\boldsymbol{m}_{\text{MAP}}$ and $\boldsymbol{m}_{\text{true}}$ in these cases, we expect posterior uncertainties to be small as well. As a representative scenario for these small-uncertainty cases, we choose $\theta = 140°$ and $L_c = 0.8L$ for MCMC.

We also postulate that the converse is true. That is, when the faults don't significantly obstruct the flow, and when they're far from the observation locations, the difference between $\boldsymbol{m}_{\text{MAP}}$ and $\boldsymbol{m}_{\text{true}}$ as well as posterior uncertainties should be large. We choose two cases, $\theta = 0, c = 0.8L$ and $\theta = 40, c = 0.2L$, for MCMC to represent this trend. To represent uncertainties between these two extremes, we also perform MCMC for $\theta = 0°$ and $L_c = 0.4L$. In summary, we perform MCMC using the following scenarios: $(\theta, L_c) = (140°, 0.8L)$ $(0°, 0.4L)$ $(0°, 0.8L)$ $(40°, 0.2L)$. Here, we only focus on interpreting the uncertainties obtained from MCMC – a detailed description of our MCMC workflow is given in Section C.2.

Figure 4.6 summarizes all uncertainties – prior, posterior, and approximate posterior (using Laplace's method) – in the fault permeabilities[2] for the chosen (θ, L_c) scenarios. We also report these uncertainties propagated to the discounted future oil production[3]. Unsurprisingly, when $\theta = 140$ and $L_c = 0.8L$, the posterior distribution for the fault permeabilities is extremely peaked and centered around $\boldsymbol{m}_{\text{true}}$, suggesting that the uncertainties in the log-transmissibilities are extremely small. This high confidence in the log-transmissibilities carries over to the Quantity of Interest. The uncertainties in both the log-transmissibilities as well as the QoI are well captured by the Laplace distribution.

On the contrary, when $\theta = 0, c = 0.8L$ and $\theta = 40, c = 0.2L$, the uncertainties in both the log-transmissibilities as well as the QoI are much larger. Of note, however, is that the nature of uncertainties is quite different, both in the transmissibilities and the QoI. Here, the Laplace distribution doesn't approximate the posterior distribution as accurately. Notably, it fails to capture the thicker tails of the true posterior for fault 2 when $\theta = 40°, c = 0.2L$, and both faults when $\theta = 0, c = 0.8L$. This poor approximation also propagates to the future discounted oil production.

[2]Recall that we plot uncertainties in the fault log-permeabilities (more precisely, $\log K_f/K$) instead of the log-transmissibilities m for easier interpretation. The two are equivalent up to a constant.

[3]These are the so-called predictive distributions.

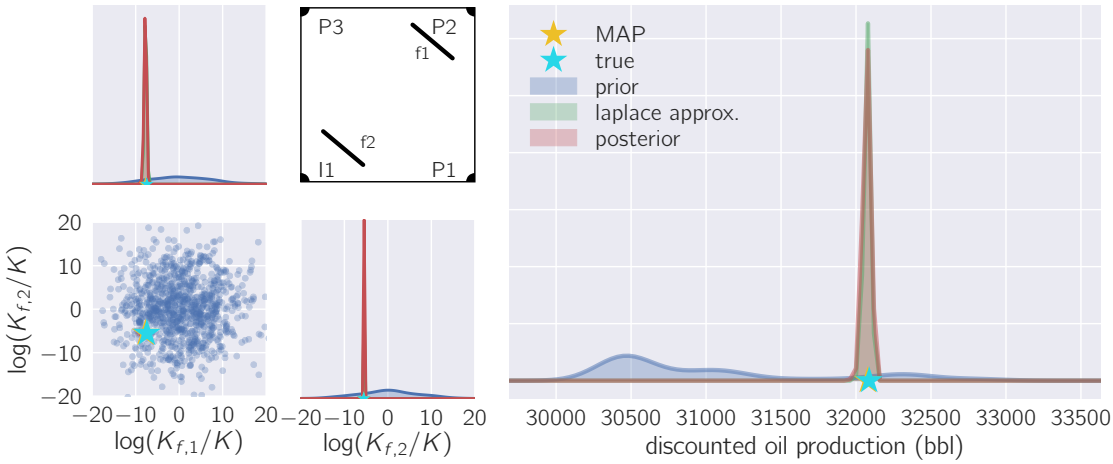

(a) $\theta = 140°, c = 0.8L$

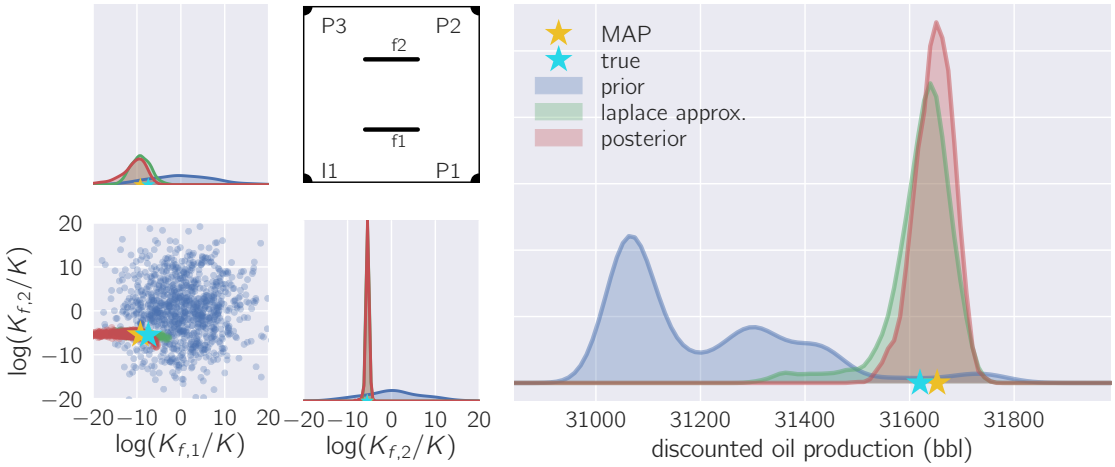

(b) $\theta = 0°, c = 0.4L$

Figure 4.6

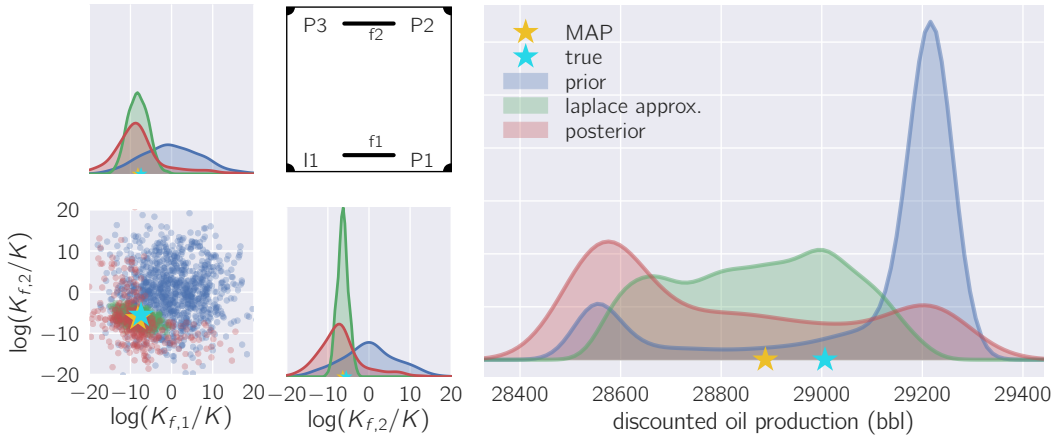

(a) $\theta = 0°, c = 0.8L$

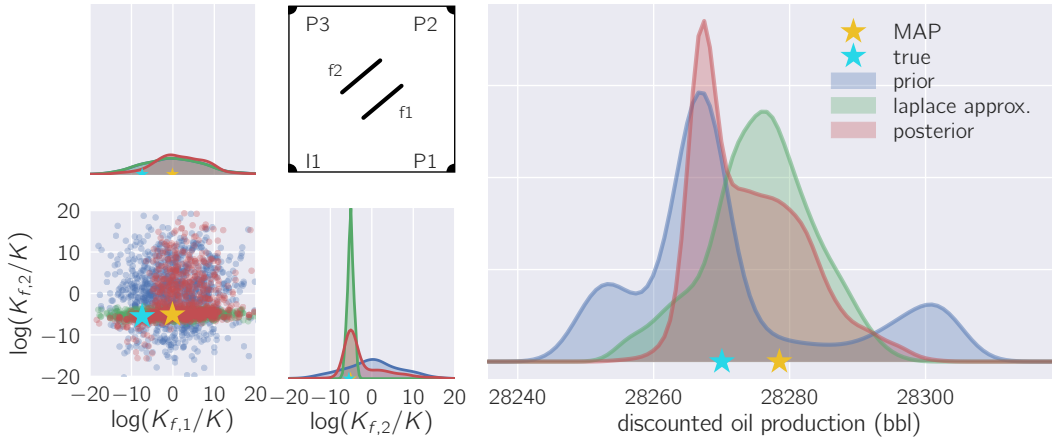

(b) $\theta = 40°, c = 0.2L$

Figure 4.6: *Uncertainties for various cases in the geometry experiment. The left-half of each subplot shows prior, posterior, and approximate (using Laplace's method) posterior uncertainties in the fault* log-permeabilities*, as well as the fault arrangement for the corresponding scenario. The right-half shows the these uncertainties propagated to the discounted future oil production. We show 1000 samples from the prior and the Laplace approximation in each scenario. The posterior samples are generated using the pCN MCMC algorithm. The number of* effective *samples generated in each case varies, depending on the autocorrelation within the Markov Chain. We obtained (and show here) 221, 1507, 391, and 950 effective samples for* $(140°, 0.8L)$, $(0°, 0.4L)$, $(0°, 0.8L)$, $(40°, 0.2L)$ *respectively. For a complete description of our MCMC workflow, see Section C.2. In* (a), *the ground-truth and MAP estimates of the fault transmissibilities and the QoI are nearly identical, hence the marker corresponding to the MAP estimate appears invisible.*

θ	L_c/L	$D_{\mathrm{KL}}(\pi^{\natural}_{\mathrm{post}}\|\|\pi^{\natural}_{\mathrm{prior}})$	$D_{\mathrm{KL}}(\pi^{\natural}_{\mathrm{post}}\|\|\pi^{\natural}_{\mathrm{laplace}})$
140°	0.8	4.25	0.02
0°	0.4	3.63	0.15
0°	0.8	0.94	1.50
40°	0.2	0.62	0.25

Table 4.3: *The Kullback-Leibler divergence between the various predictive distributions. The predictive Laplace approximation is closest to the true posterior predictive distribution when $\theta = 140°, c = 0.8L$. The KL divergences are obtained using a Monte-Carlo procedure, which is detailed in Section C.2.*

Finally, when $\theta = 0°$ and $L_c = 0.4L$, the uncertainties, in both the fault log-transmissibilities and the QoI, are indeed moderate – neither are they as peaked as the $\theta = 140°$ and $L_c = 0.8L$ case, nor are they as expansive as when $\theta = 0°, c = 0.8L$ or $\theta = 40°, c = 0.2L$. While not as accurate as the $\theta = 140, c = 0.8L$ scenario, the Laplace approximation estimates the posterior uncertainty reasonably well.

To quantify how close the Laplace approximation is to the posterior distribution, we report the Kullback-Leibler (KL) divergence between *i*) the posterior-predictive distribution $\pi^{\natural}_{\mathrm{post}}$, and the prior-predictive distribution $\pi^{\natural}_{\mathrm{prior}}$, and *ii*) $\pi^{\natural}_{\mathrm{post}}$ and the predictive distribution corresponding to the Laplace approximation $\pi^{\natural}_{\mathrm{laplace}}$ in Table 4.3. The Kullback-Leibler, although not a true metric, is a measure of the distance between two probability distributions:

$$D_{\mathrm{KL}}(\pi_1||\pi_2) = \int \pi_1(\boldsymbol{m}) \log \frac{\pi_1(\boldsymbol{m})}{\pi_2(\boldsymbol{m})} \mathrm{d}\boldsymbol{m} \tag{4.28}$$

The results in Table 4.3 confirm our intuition that $\pi^{\natural}_{\mathrm{laplace}}$, the predictive distribution corresponding to π_{laplace}, approximates the posterior-predictive distribution best when faults permeabilities have been inferred with least uncertainty, and becomes a progressively poorer approximation as the posterior uncertainties in the fault become larger.

Conclusions From this numerical experiment, we conclude that:

1. Uncertainties are the smallest when faults directly obstruct the flow (such as the $\theta = 140^\circ$ case), or when faults are really close to the observation locations (such as $\theta = 40^\circ$ when L_c/L is large). In such cases, the Laplace approximation of the posterior captures the uncertainties in the log-transmissibilities and the QoI well.

2. On the other hand, uncertainties, both in the transmissibility and the future discounted oil production, are the highest when faults don't obstruct the flow as much and when they're far from the observation locations. In such cases, the Laplace approximation of the posterior can fail to capture uncertainties in both the transmissibility and the QoI.

4.5.2 Identifying fault locations

Purpose To study:

- if production data can simultaneously reveal fault locations as well as transmissibilities,
- the nature of uncertainties that result, in the transmissibilities themselves, as well as the relative excess oil production Q_{excess}.

Setup In this experiment, we consider a reservoir which, in addition to the properties outlined at the beginning of this section, possesses:

- two distinct permeability zones – a high permeability channel ($K_{\text{high}} = 10$ D) running through a low permeability ($K_{\text{low}} = 0.1$ D) background, and,
- an injection well operating at constant pressure $p_{\text{bh}} = 1.2 \times 10^7$ Pa, and a production well operating at a constant rate, $Q = 0.01$ m^3/s (assuming a nominal reservoir height of 1m), both located within the high permeability channel.

Moreover, we presume that the reservoir contains two *major* faults whose locations are known precisely. The presence of several *minor* faults is suspected, but their locations and number are unknown. Such a situation can arise, for instance, when seismic data can only resolve a few large faults within the reservoir. Finally, the transmissibility of none of faults, either major or minor, is known.

We synthesize ground-truth reservoirs using two minor faults in addition to the two major faults. Further, we create independent scenarios by varying the true locations of the minor faults relative to the major ones. Schematics for the ground-truth reservoirs are shown in Figures 4.7a to 4.7c. The locations of the major faults are identical in each scenario, but the minor faults are separated from each other by a small, medium, and long distance, respectively.

The reservoir we use for inference, depicted in Figure 4.7d, differs significantly from the ground-truth setups. As the locations of the major faults are known precisely, they are placed at the same location as the ground-truth setup. However, to account for the unknown number and location of the minor faults, we postulate that the channel is interspersed with numerous smaller faults. Here, we've considered 14 smaller faults distributed evenly between the injection well and the production well, leading to a total of 16 faults in the inversion template reservoir. Additionally, to make the problem truly challenging, we've created a slight offset between the true locations of the minor faults and the ones in our template inversion reservoir. When we infer fault transmissibilities from pressure data, we infer the transmissibilities of *all* 16 faults in the reservoir. Our aim is to investigate if production data can reveal where the smaller faults are actually located. Before we hypothesize how this might happen, we distinguish between two kinds of faults in our template reservoir:

- Type 1: These are faults in the template reservoir located closest to where faults are truly present. For instance, in the large separation setup, these are faults 3, 4, 13, and 14 in Figure 4.7d. Note that this setup includes both major and minor faults.

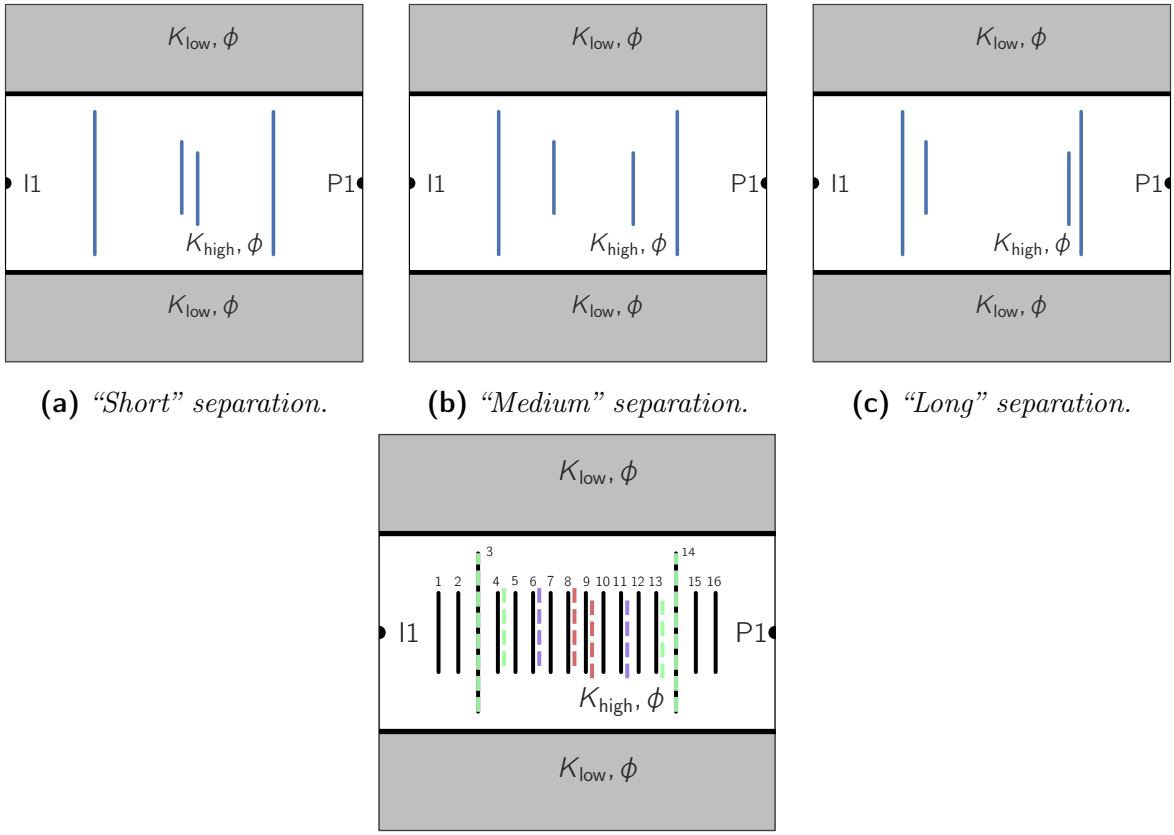

(a) *"Short" separation.*

(b) *"Medium" separation.*

(c) *"Long" separation.*

(d) *Reservoir used for inversion. The faults actually included in the inversion reservoir are shown in black, while the dashed colored lines show the ground-truth fault locations for each scenario.*

Figure 4.7: *Schematics showing the ground-truth (Figures 4.7a to 4.7c) reservoirs, and the inversion template (Figure 4.7d). We generate data using the ground-truth reservoir, but infer fault transmissibilities using the inference template. The inference template contains 16 faults - 2 major and 14 minor. The locations of the major faults correspond exactly between the ground-truth reservoirs and the inference template. However, there are more minor faults in the inference template. In addition, the minor faults are actually slightly offset from their template counterparts.*

- Type II: These faults are extraneous. Again for the large separation case, this type includes faults 1, 2, 5, 6, 7, 8 9, 10, 11, 12, 15, 16.

For production data to be considered discriminative of the location *and* transmissibilities of all faults, the following conditions must be met simultaneously:

- The transmissibility uncertainties in Type 1 faults should cluster around the corresponding ground-truth values, i.e., the transmissibilities that generated the production data.
- For Type II faults, the uncertainty in the transmissibility should indicate the absence of the faults by clustering around m_0, the value at which background and fault permeabilities are equal.

With this experiment, our goal is to investigate the extent to which these conditions are met.

We note that we use the same inversion template across three ground-truth scenarios, as the true locations of the smaller faults are unknown. In this experiment, the time step for the forward simulation is 0.05 days. The assimilation windows are 24.6, 30.75, and 25.85 days respectively, while the the prediction window lasts another 11.1, 14.8, and 10.6 days respectively. The major and minor faults are 150 m and 50 m long, respectively, while the high permeability channel is 250 m long.

Results. Prior and approximate posterior marginals (using the Laplace approximation) are shown in the left-side of Figure 4.11 for each fault, along with the ground truth and MAP estimates. Unfortunately, for this experiment, MCMC failed to yield enough effective samples from the true posterior distribution. The chains were too correlated to be yield enough effective samples – generating even a few hundred effective samples for each scenario would've required several months of computation time. We conjecture that this is because

the posterior is significantly non-Gaussian and possesses rapidly changing local relationships between the variables.

The Laplace approximation from different scenarios displays several illuminating trends. These are:

- The MAP estimates of the major faults are close to their true counterparts. In addition, the Laplace approximation suggests high confidence in the MAP estimates.
- The MAP estimate hints at the presence of more minor faults than are actually present in each scenario. Further, the Laplace uncertainties for the minor faults can be misleading. In several cases, Laplace uncertainties suggest the presence of a fault where there is none, while in others they indicate the absence of a fault where one is actually present.
- There are occasions where the MAP estimate does correctly indicate the absence of a fault. However, the Laplace uncertainties for such faults are simply equal to the prior uncertainties, suggesting no confidence in the inferred values.
- In several cases, the true value of the fault transmissibility is outside the support of the Laplace distribution. We conjecture that the true posterior for such faults actually has thicker tails that encompass the true fault transmissibilities.

The QoI we study in this experiment is the relative increase in the future discounted production of the reservoir after drilling an infill well. We assume that the infill well is drilled at the end of the assimilation window, i.e., $t = T_{\text{obs}}$ at at some location $\boldsymbol{x} = \boldsymbol{x}_{\text{infill}}$ that is separate for each scenario. For each scenario, we select $\boldsymbol{x}_{\text{infill}}$ as follows. Using the MAP estimate of the transmissibility, we find the water saturation field at $t = T_{\text{obs}}$ and identify where pockets of unswept oil are being created. Then, we place the infill well at the (approximate) center of each pocket and compute the relative increase in the future discounted production, again

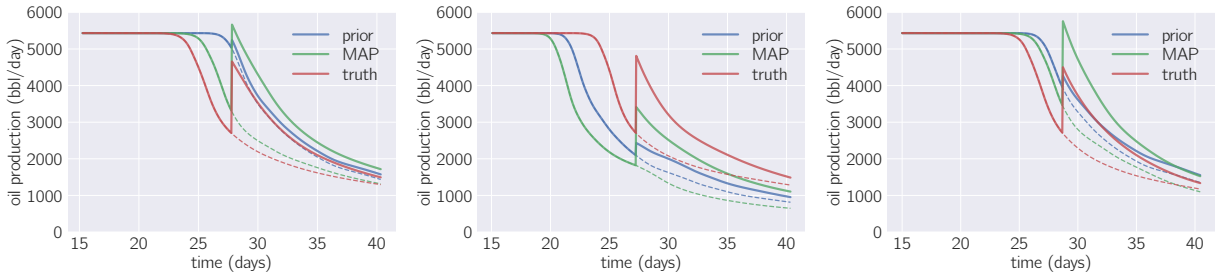

(a) *"Short"* **(b)** *"Medium"* **(c)** *"Long"*

Figure 4.8: *A comparison of the production curves at the prior mean ($\boldsymbol{m}_0$), ground-truth ($\boldsymbol{m}_{\text{true}}$), and MAP estimate ($\boldsymbol{m}_{\text{MAP}}$) of the fault transmissibilities.*

using the MAP estimate of the fault transmissibilities. Finally, we select that location which leads to the greatest relative increase. The locations we finally selected were: $(0.68L, 0.5L)$, $(0.8L, 0.5L)$, and $(0.54L, 0.5L)$ for the "short", "medium", and "long" cases respectively.

The prior- and posterior-predictive distributions for this QoI are shown in the right side of Figure 4.11. Although the MAP and the true QOI values are quite close, the support of the prior distribution under-predicts the relative increase, while the Laplace distribution over-predicts it. We also compare the production curves from the prior mean, the MAP estimate, and the ground truth in Figure 4.8. As we observed in Figure 4.11, the prior significantly under-predicts the increase in oil production with and without the infill well. In Figure 4.9, we compare the saturation field at $t = T_{\text{obs}}$ and $t = T$ at the ground-truth and MAP estimate of the fault transmissibilities. Although the MAP estimate of the fault transmissibilities predicted the presence of more faults than actually present, the final saturation fields are quite similar.

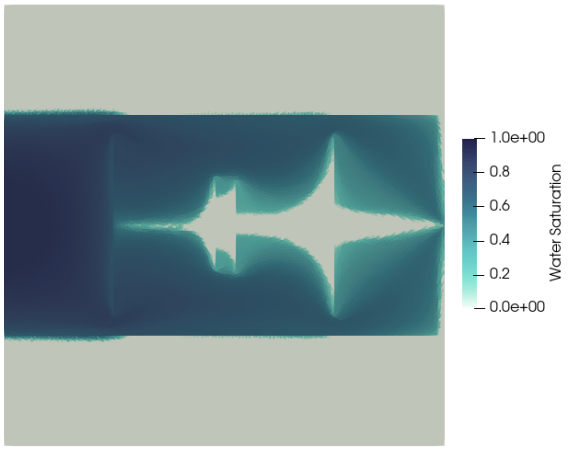

(a) *Ground-truth water saturation field at* $t = T_{\text{obs}}$.

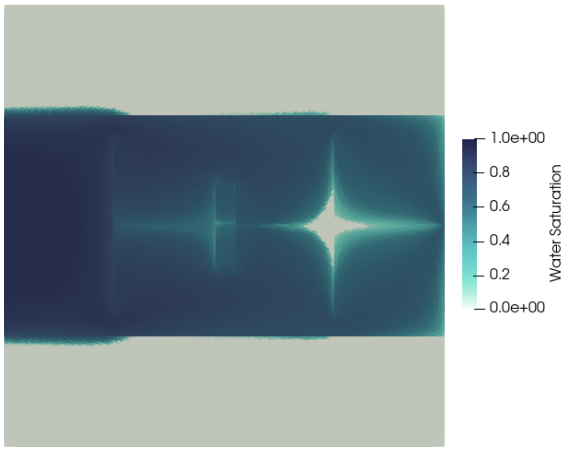

(b) *Ground-truth water saturation field at* $t = T$. *An infill well is present at* $(0.68L, 0.5L)$ *and active since* $t = T_{\text{obs}}$.

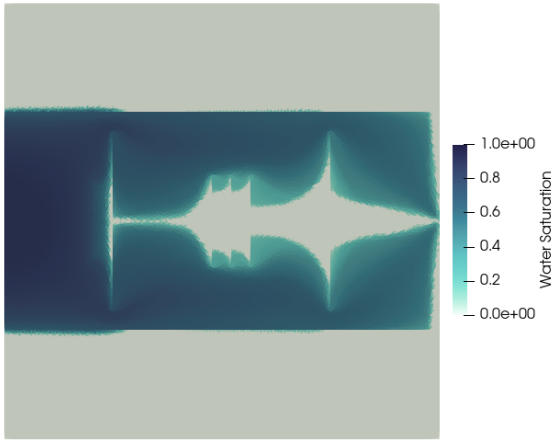

(c) *Water saturation estimated using* $\boldsymbol{m}_{\text{MAP}}$ *field at* $t = T_{\text{obs}}$.

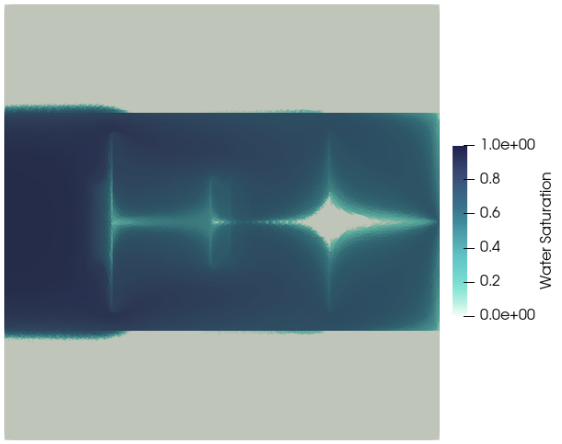

(d) *Water saturation estimated using* $\boldsymbol{m}_{\text{MAP}}$ *field at* $t = T$. *An infill well is present at* $(0.68L, 0.5L)$ *and active since* $t = T_{\text{obs}}$

Figure 4.9: *A comparison of the water saturation fields at* $t = T_{\text{obs}}$ *and* $t = T$ *for the "short" separation scenario. Although the MAP estimate predicts the presence of more faults than are actually present, the final estimates of the saturation fields is quite close to the true value. Here, we've used a mesh that's approximately* $4\times$ *finer than the one we use for inference.*

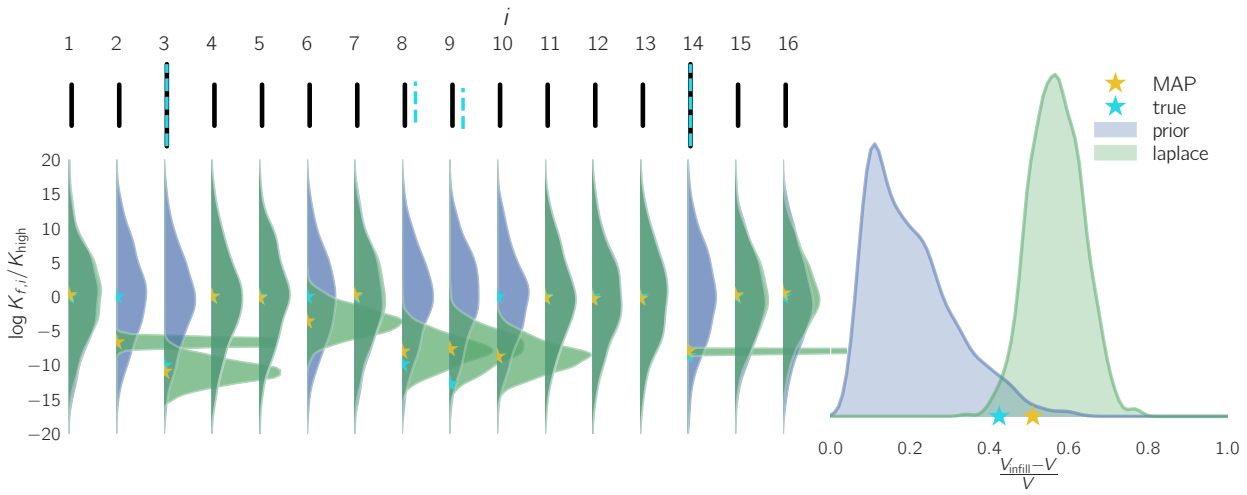

(a) *"Short" separation.*

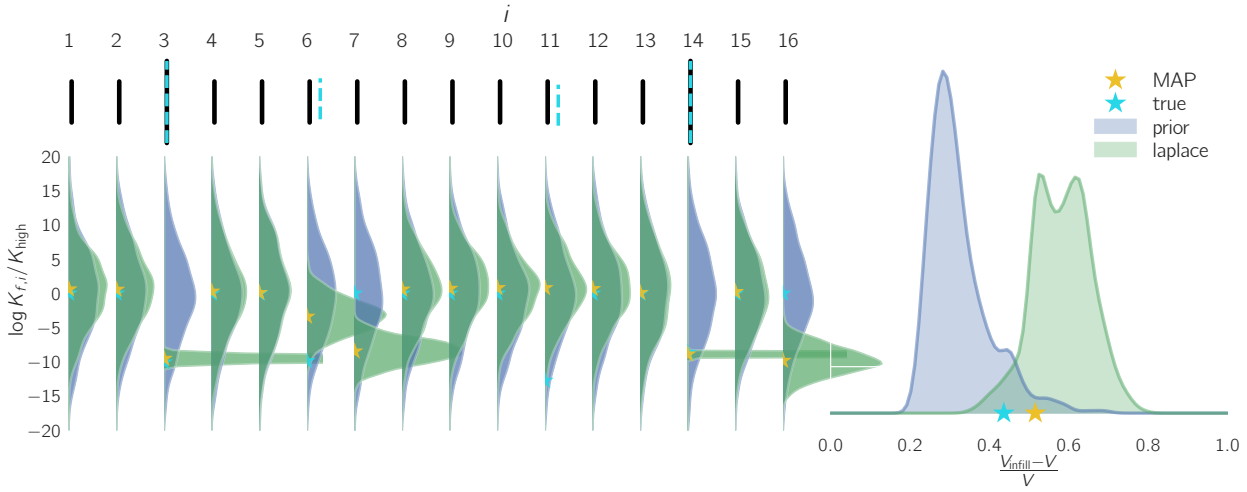

(b) *"Medium" separation.*

Figure 4.11

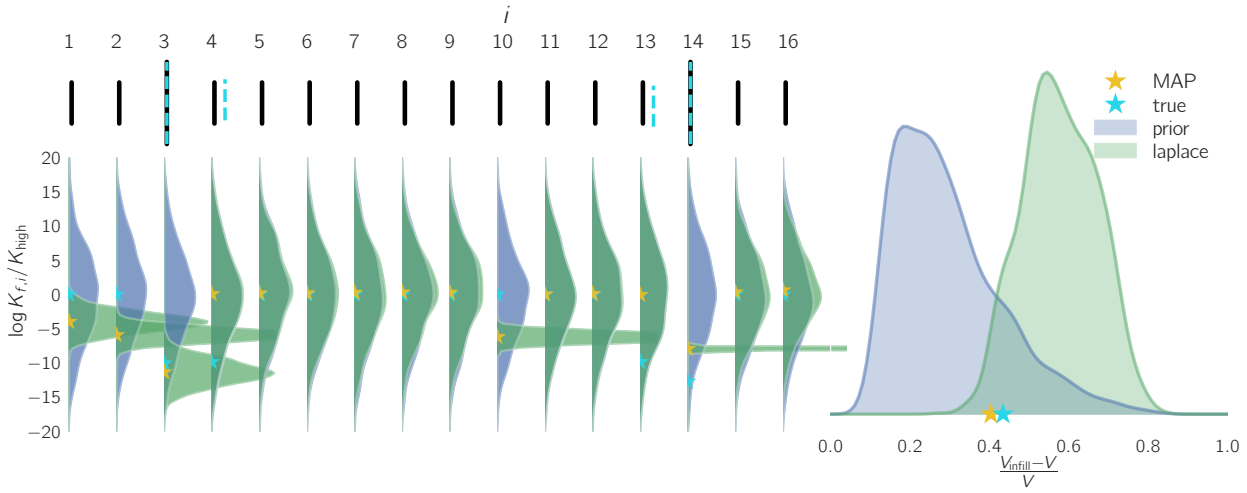

(a) *"Long" separation.*

Figure 4.11: *Prior and approximate (using Laplace's method) posterior uncertainties in the fault log-permeabilities (left), as well as the relative production increase (right) for each scenario. Here, we've used 1500 independent samples from the prior and the approximate posterior to estimate the probability distributions using Kernel Density Estimation. The Laplace distribution for the major faults is highly concentrated in each scenario and has been truncated for clarity.*

Conclusions From the Laplace approximation of the posterior, we conclude that:

- The major faults can be inferred from production data with high confidence.
- The production data does not seem to be discriminative of the location, number, or transmissibilities of the minor faults.

However, these conclusions need to be verified against uncertainties from the true posterior. We leave this as future work.

4.6 Conclusions

In this chapter, we described a Bayesian approach to infer fault transmissibilities from pressure observations recorded at the wells. Our approach employed synthetic two-dimensional reservoirs consisting of two compressible fluid phases and a reduced model to describe fault behavior. In addition, we explored how the resulting posterior distribution varied under different reservoir conditions.

In our first experiment, we varied the relative arrangement of the faults within the reservoir. Here, we observed that posterior uncertainties are the smallest when faults directly obstruct the flow, or when faults are really close to the observation locations. Moreover, in such cases the Laplace approximation of the posterior captures the uncertainties in the log-transmissibilities and the QoI accurately. On the contrary, uncertainties, are the highest when faults don't obstruct the flow as much and when they're far from the observation locations. Here, the Laplace approximation of the posterior can fail to capture the heavy tailed behavior of the posterior distribution.

In our second experiment, we investigated whether production data had enough information to inform both the location and transmissibilities of the faults. Although we were unable to explore the posterior distribution using MCMC for this experiment, we obtained interesting results using the Laplace approximation of the posterior. We found that while the production data could discern the transmissibilities of the major faults accurately, it couldn't identify the location or the transmissibilities of the minor faults with any appreciable degree of confidence. The support of the Laplace distribution also varied significantly between the major and minor faults, hinting that the shape of the posterior distribution is too challenging for the pCN algorithm. In our future work, we wish to address this shortcoming. A major challenge here will be designing an MCMC algorithm that can navigate the rapidly changing local relationships in the posterior. Recent work on MCMC algorithms that leverage gradients [43] and non-linear transport maps [64] provides a promising avenue to overcome this challenge.

Chapter 5

Conclusions and Future Work

5.1 Summary of Conclusions

Rare-events probability estimation. We proposed two importance sampling algorithms, BIMC and its sequel A-BIMC, that leverage derivatives of the forward map f to efficiently compute rare-event probabilities. The key insight used to construct the importance sampling density in BIMC is that the ideal importance sampling density can be mollified into the posterior distribution of a fictitious Bayesian inverse problem. Theoretical analysis established that BIMC is optimal in the setting where the input-output map is affine and the nominal density is Gaussian. Our numerical experiments support this conclusion and demonstrate that when input-output map is nearly affine, BIMC is nearly 10 to 50 times cheaper than a Monte Carlo approach. These experiments also revealed several drawbacks in BIMC, which we attempted to address in A-BIMC.

A-BIMC proceeds in two stages. The first stage constructs a rough approximation of the ideal importance sampling distribution by exploring, on a global scale, the regions that trigger the rare-event. The second stage refines the rough approximation yielded by the first Via numerical experiments, we demonstrated that A-BIMC leads to orders-of-magnitude speedup over a simple Monte Carlo method. We also established that A-BIMC is independent of the rarity level of the problem. Finally, we demonstrated that A-BIMC does break down as the ambient dimensionality of the problem increases. This breakdown is due to MPMC, the algorithm employed to refine the Gaussian mixture distribution yielded by the first stage.

Inferring fault transmissibilities. We described a Bayesian approach to infer fault transmissibilities from pressure observations recorded at the wells. Our approach employed synthetic two-dimensional reservoirs consisting of two compressible fluid phases and a reduced model to describe fault behavior. In addition, we explored how the resulting posterior distribution varied under different reservoir conditions. In our first experiment, we varied the relative arrangement of the faults within the reservoir. Here, we observed that posterior uncertainties are the smallest when faults directly obstruct the flow, or when faults are really close to the observation locations. We found that the converse is also true - uncertainties were highest when faults don't obstruct the flow as much and when they're far from the observation locations. In our second experiment, we investigated whether production data had enough information to inform both the location and transmissibilities of the faults. Although we were unable to explore the posterior distribution using MCMC for this experiment, we obtained interesting results using the Laplace approximation of the posterior. We found that while the production data could discern the transmissibilities of the major faults accurately, it couldn't identify the location or the transmissibilities of the minor faults with any appreciable degree of confidence.

5.2 Future Work

In Chapter 3, we outlined a general dimension reduction strategy for rare-event importance sampling. The key observation here was that the breakdown of IS schemes with increasing ambient dimension can be arrested by employing those algorithms only in the subspace in which the ideal importance sampling density differs from the nominal distribution. However, designing algorithms to discover the subspace in question still remains an open research challenge. In the future, we aim to apply techniques developed for dimension reduction in Bayesian inverse problems [24, 96] to reduce the dimension of the rare-event probability estimation problem.

We were unable to efficiently explore the posterior distribution using MCMC for the unknown fault location experiment in Chapter 4. In our future work, we wish to address this shortcoming. A major challenge here will be designing an MCMC algorithm that can navigate the rapidly changing local relationships in the posterior. Recent work on MCMC algorithms that leverage gradients [43] and non-linear transport maps [64] provides a promising avenue to overcome this challenge.

Appendices

Appendix A

This appendix provides details of the forward maps used in Chapter 2.

A.1 Implementation details

A.1.1 The affine case

We construct a affine map from $\mathbb{R}^m$ to $\mathbb{R}$. The map is defined as

$$f(\boldsymbol{m}) = \boldsymbol{o}^T \mathbf{A} \boldsymbol{m}, \tag{A.1}$$

where, $\boldsymbol{o} = \left(\frac{1}{m}, \frac{1}{m}, \ldots, \frac{1}{m}\right)^T \in \mathbb{R}^m$ is an observation operator and

$$\mathbf{A} = \begin{pmatrix} 1 & 0 & 0 & \cdots & 0 \\ 0 & \frac{1}{2} & 0 & \cdots & 0 \\ 0 & 0 & \frac{1}{3} & & \vdots \\ \vdots & \vdots & & \ddots & 0 \\ 0 & 0 & \cdots & 0 & \frac{1}{m} \end{pmatrix}. \tag{A.2}$$

A.1.1.1 Implementation

We assume $p(\boldsymbol{m})$ is a Gaussian distribution with mean $\boldsymbol{m}_0$ and covariance $\boldsymbol{\Sigma}_0$, where $\boldsymbol{m}_0 = (1, 1, \ldots, 1)^T \in \mathbb{R}^m$ and $\boldsymbol{\Sigma_0} = 0.1\mathbf{I} \in \mathbb{R}^{m \times m}$. Here, $\mathbf{I}$ is the m dimensional identity matrix. We chose $\mathbb{Y} = [1.2803, 1.4571]$ when $m = 2$ and $\mathbb{Y} = [6.2 \times 10^{-2}, 6.3 \times 10^{-3}]$ when $m = 100$. The MAP point was computed using MATLAB's `fminunc` routine.

A.1.2 Synthetic non-linear case

For quick testing, we construct the following non-linear problem from $\mathbb{R}^m$ to $\mathbb{R}$:

$$f(\boldsymbol{m}) = \boldsymbol{o}^T \boldsymbol{u}, \text{ where,} \tag{A.3}$$

$$\left(\mathbf{S} + \varepsilon \boldsymbol{m}\boldsymbol{m}^T\right) \boldsymbol{u} = \boldsymbol{b}. \tag{A.4}$$

A.1.2.1 Implementation

Again, $\boldsymbol{o} \in \mathbb{R}^m$ is an observation operator. For this problem, we chose $\boldsymbol{o} = [1, 0, \ldots, 0]^T$. $\mathbf{S}$ is a randomly chosen symmetric positive definite matrix, while $\boldsymbol{b}$ is a randomly chosen vector whose entries are distributed according to the standard normal distribution. We set $\varepsilon = 0.01\|\mathbf{S}\|_2$. The nominal probability density in this case is $p(\boldsymbol{m})$ is a Gaussian with mean $\boldsymbol{m}_0 = (1, 1, \ldots, 1)^T$ and covariance $\boldsymbol{\Sigma_0} = 0.01\mathbf{I}$. The target interval $\mathbb{Y}$ is chosen to be $[1.24, 1.25]$ when $m = 10$ and $[0.919, 0.923]$ when $m = 2$. MATLAB's `fminunc` routine was used for optimization again.

A.1.3 Single step reaction

The single step reaction is described by the following ODE:

$$\begin{aligned} &\frac{\mathrm{d}u}{\mathrm{d}t} = \frac{S^*(u)}{\tau_{\mathrm{R}}}, \quad 0 < t < t_f, \\ &S^*(u) = Bu(1-u)\exp\left(\frac{-T_{\mathrm{Act}}}{T_{\mathrm{u}} + (T_{\mathrm{b}} - T_{\mathrm{u}})u}\right), \end{aligned} \tag{A.5}$$

and we define $x = u(0)$ and $f(x) = u(t_f)$.

This equation uses the Arrhenius equation to describe the rate of a chemical reaction in terms of a progress variable u. The progress variable is routinely employed in the analyses of turbulent flames and is 0 in regions of pure reactants and 1 in pure products [69].

Here, τ_{R} is the time scale of the reaction and $S^*(u)$ is the normalized source term. The numerical constant in $S^*(u)$, B, ensures that it integrates to unity, T_{Act} is the activation temperature, T_{u} is the temperature of the unburned reactants and T_{b} the temperature of the burnt products.

Since u is always bounded between 0 and 1, the differential operator defined in eq. (A.5) is a map from $[0, 1]$ to $[0, 1]$.

A.1.3.1 Implementation

For our numerical experiments, we set, $T_{\mathrm{u}} = 300$ K, $T_{\mathrm{b}} = 2100$ K, $T_{\mathrm{Act}} = 30{,}000$ K, $B = 6.11 \times 10^7$, $\tau_{\mathrm{R}} = 1$s.

Further, we choose $\mathbb{Y} = [0.7, 0.8]$ and $p(x) = \mathcal{N}(0.5, 0.01)$. We used MATLAB's `fmincon` routine to perform constrained optimization in order to compute the MAP point.

A.1.4 Hydrogen Autoignition

We observe the heat released, Q, during autoignition of a hydrogen-air mixture in an adiabatic, constant pressure, fixed mass reactor. To describe the chemistry, we use a reduced mechanism that involves 5 elementary reactions among 8 chemical species - $\mathrm{H_2}, \mathrm{O_2}, \mathrm{N_2}, \mathrm{HO_2}, \mathrm{H}, \mathrm{O}, \mathrm{OH}, \mathrm{H_2O}$ [94]. We assume-

- reactants are ideal gases,
- there are no spatial gradients of temperature or species concentrations,
- the volume of the reactor can change to keep the pressure constant,
- only $\mathrm{H_2}, \mathrm{O_2}$, and $\mathrm{N_2}$ are present in the reactor initially.

Then specifying the pressure (P), temperature (T), and equivalence ratio (ϕ, defined as $\frac{[H_2]}{2[O_2]}$) is sufficient to completely define the initial state of the system. It is this triad that we define as our parameter vector, $\boldsymbol{m} = (\phi, T, P)^T$. As stated earlier, the observable is the total heat released Q.

A.1.4.1 Implementation

We assume $p(\boldsymbol{m})$ is a Gaussian with mean $\boldsymbol{m}_0$ and covariance Σ_0, where,

$$\begin{aligned} \boldsymbol{m}_0 &= \begin{bmatrix} 1 \\ 1500 \\ 1.01325 \end{bmatrix}, \\ \Sigma &= \begin{bmatrix} 0.01 & 0 & 0 \\ 0 & 15.0 & 0 \\ 0 & 0 & 0.00101 \end{bmatrix}. \end{aligned} \tag{A.6}$$

In addition, we select $\mathbb{Y} = [21000, 22000]$. The initial volume of the reactor is set to $V_0 = 1\text{m}^3$. We use MATLAB's inbuilt `fminunc` algorithm to perform the non-linear optimization.

A.1.4.2 Summary of equations

Table A.1: *Reduced chemistry for hydrogen autoignition. Reaction rate constant* $k = AT^b e^{-E/RT}$. *Units are mol, cm, s, K, kJ. Chaperone efficiencies are* 2.5 *for* H_2, 16.0 *for* H_2O *and* 1.0 *for all other species. Troe falloff with* $F_{cent} = 0.5$ *is assumed for reaction 5.*

No.	Reaction		A	b	E
1	$H_2 + O_2 \longrightarrow H + HO_2$		2.69×10^{12}	0.36	231.86
2	$H + O_2 \longrightarrow OH + O$		3.52×10^{16}	-0.7	71.4
3	$O + H_2 \longrightarrow H + OH$		5.06×10^{4}	2.7	26.3
4	$OH + H_2 \longrightarrow H + H_2O$		1.17×10^{9}	1.3	15.2
5	$H + O_2 + M \longrightarrow HO_2 + M$	k_0	5.75×10^{19}	-1.4	0.0
		k_∞	4.65×10^{12}	0.4	0.0

Williams ([94]) identified a set of 5 elementary steps to study autoiginition of hydrogen-air mixtures. These elementary steps are given in table A.1.

The net rates of production of each species, $\dot{S}_i$, are given below:

$$\begin{aligned}
\dot{S}_{\mathrm{H_2}} &= -\dot{\omega}_1 - \dot{\omega}_3 - \dot{\omega}_4, \\
\dot{S}_{\mathrm{O_2}} &= -\dot{\omega}_1 - \dot{\omega}_2 - \dot{\omega}_5, \\
\dot{S}_{\mathrm{O}} &= \dot{\omega}_2 - \dot{\omega}_3, \\
\dot{S}_{\mathrm{H}} &= \dot{\omega}_1 - \dot{\omega}_2 + \dot{\omega}_3 + \dot{\omega}_4 - \dot{\omega}_5, \\
\dot{S}_{\mathrm{OH}} &= \dot{\omega}_2 + \dot{\omega}_3 - \dot{\omega}_4, \\
\dot{S}_{\mathrm{HO_2}} &= \dot{\omega}_1 + \dot{\omega}_5, \\
\dot{S}_{\mathrm{H_2O}} &= \dot{\omega}_4 \\
\dot{S}_{\mathrm{N_2}} &= 0,
\end{aligned} \tag{A.7}$$

where ω_i is the rate of the ith reaction in table A.1:

$$\begin{aligned}
\dot{\omega}_1 &= k_{f,1}[H_2][O_2] \\
\dot{\omega}_2 &= k_{f,2}[H][O_2] \\
\dot{\omega}_3 &= k_{f,3}[O][H_2] \\
\dot{\omega}_4 &= k_{f,4}[OH][H_2] \\
\dot{\omega}_5 &= k_{f,5}[H][O_2].
\end{aligned} \tag{A.8}$$

Here,

$$k_{f,i} = A^{(i)} T^{b^{(i)}} e^{-E^{(i)}/RT},\ i = 1 \ldots 4, \tag{A.9}$$

R, the universal gas constant has the value 8.314 J/K/mol. $A^{(i)}$, $b^{(i)}$ and $E^{(i)}$ are as specified in table A.1. $k_{f,5}$ is calculated using the Lindemann form as:

$$
\begin{aligned}
&P_r = \frac{k_0[M]}{k_\infty},\\
&[M] = 2.5[H_2] + [O_2] + [H] + [O] + [OH] + [HO_2] + 16[H_2O] + [N_2],\\
&k_{f,5} = k_\infty\Big(\frac{P_r}{1+P_r}\Big),\\
&k_0 = A^{(0)}T^{b^{(0)}}e^{-E^{(0)}/RT},\\
&k_\infty = A^{(\infty)}T^{b^{(\infty)}}e^{-E^{(\infty)}/RT},
\end{aligned}
\tag{A.10}
$$

with the Arrhenius parameters as in table A.1.

The molar enthalpies ($\bar{h}$) and specific heats ($\bar{c}_p$) for each species are given by:

$$
\begin{aligned}
\frac{\bar{c}_p(T)}{R} &= a_0 + a_1T + a_2T^2 + a_3T^3 + a_4T^4,\\
\frac{\bar{h}(T)}{RT} &= a_0 + \frac{a_1}{2}T + \frac{a_2}{3}T^2 + \frac{a_3}{4}T^3 + \frac{a_4}{5}T^4 + \frac{a_5}{T}.
\end{aligned}
\tag{A.11}
$$

where the coefficients $a_0 \dots a_5$ are tabulated in ref. [84] for each species.

The rate of heat release per unit volume is:

$$
\Delta\dot{q} = -\bar{h}_{\mathrm{H_2}}\dot{S}_{\mathrm{H_2}} - \bar{h}_{\mathrm{O_2}}\dot{S}_{\mathrm{O_2}} - \bar{h}_{\mathrm{H}}\dot{S}_{\mathrm{H}} - \bar{h}_{\mathrm{O}}\dot{S}_{\mathrm{O}} - \bar{h}_{\mathrm{OH}}\dot{S}_{\mathrm{OH}} \tag{A.12}
$$

$$
- \bar{h}_{\mathrm{HO_2}}\dot{S}_{\mathrm{HO_2}} - \bar{h}_{\mathrm{H_2O}}\dot{S}_{\mathrm{H_2O}} - \bar{h}_{\mathrm{N_2}}\dot{S}_{\mathrm{N_2}}. \tag{A.13}
$$

The following ODEs describe the chemistry inside a constant pressure adiabatic reactor:

$$
\begin{aligned}
&\frac{\mathrm{d}T}{\mathrm{d}t} = \frac{\Delta\dot{q}}{\beta},\\
&\frac{\mathrm{d}[H_2]}{\mathrm{d}t} = \dot{S}_{\mathrm{H_2}} - \alpha[H_2],\\
&\frac{\mathrm{d}[O_2]}{\mathrm{d}t} = \dot{S}_{\mathrm{O_2}} - \alpha[O_2],\\
&\frac{\mathrm{d}[H]}{\mathrm{d}t} = \dot{S}_{\mathrm{H}} - \alpha[H],\\
&\frac{\mathrm{d}[O]}{\mathrm{d}t} = \dot{S}_{\mathrm{O}} - \alpha[O],\\
&\frac{\mathrm{d}[OH]}{\mathrm{d}t} = \dot{S}_{\mathrm{OH}} - \alpha[OH],\\
&\frac{\mathrm{d}[HO_2]}{\mathrm{d}t} = \dot{S}_{\mathrm{HO_2}} - \alpha[HO_2],\\
&\frac{\mathrm{d}[H_2O]}{\mathrm{d}t} = \dot{S}_{\mathrm{H_2O}} - \alpha[H_2O],\\
&\frac{\mathrm{d}[N_2]}{\mathrm{d}t} = \dot{S}_{\mathrm{N_2}} - \alpha[N_2],\\
&\frac{1}{V}\frac{\mathrm{d}V}{\mathrm{d}t} = \alpha,\\
&\alpha = \left(\frac{\dot{S}_{\mathrm{H_2}} + \dot{S}_{\mathrm{O_2}} + \dot{S}_{\mathrm{H}} + \dot{S}_{\mathrm{O}} + \dot{S}_{\mathrm{OH}} + \dot{S}_{\mathrm{HO_2}} + \dot{S}_{\mathrm{H_2O}} + \dot{S}_{\mathrm{N_2}}}{[H_2] + [O_2] + [H] + [O] + [OH] + [HO_2] + [H_2O] + [N_2]} + \frac{1}{T}\frac{\mathrm{d}T}{\mathrm{d}t}\right),\\
&\beta = [H_2]\bar{c}_{p,\mathrm{H_2}} + [O_2]\bar{c}_{p,\mathrm{O_2}} + [H]\bar{c}_{p,\mathrm{H}} + [O]\bar{c}_{p,\mathrm{O}} + [OH]\bar{c}_{p,\mathrm{OH}}\\
&+ [HO_2]\bar{c}_{p,\mathrm{HO_2}} + [H_2O]\bar{c}_{p,\mathrm{H_2O}} + [N_2]\bar{c}_{p,\mathrm{N_2}},
\end{aligned}
$$

The net heat released is

$$
Q = \int_0^{t_f} \Delta\dot{q}V(t)\mathrm{d}t. \tag{A.14}
$$

A.1.5 The Lorenz system

The Lorenz system is defined by the following ordinary differential equations:

$$\begin{aligned}\frac{\mathrm{d}u_1(t)}{\mathrm{d}t} &= s(u_2 - u_1), \quad 0 < t < t_f,\\ \frac{\mathrm{d}u_2(t)}{\mathrm{d}t} &= u_1(r - u_3) - u_2,\\ \frac{\mathrm{d}u_3(t)}{\mathrm{d}t} &= u_2 u_2 - b u_3,\end{aligned} \tag{A.15}$$

The parameter vector is the initial condition of the system, $\boldsymbol{m} = \boldsymbol{u}(0)$ while the observable is $u_1(t_f)$.

We set $s = 10$, $r = 28$, $b = 8/3$ and observe u_1 after two time horizons, $t_f = 0.1$s and $t_f = 5$s. The nominal density $p(\boldsymbol{m})$ is selected to be a Gaussian with mean $\boldsymbol{m}_0$ and covariance $\boldsymbol{\Sigma}_0$ where,

$$\begin{aligned}\boldsymbol{m}_0 &= \begin{bmatrix} 1.508870 \\ -1.531271 \\ 25.46091 \end{bmatrix}, \text{ and,}\\ \boldsymbol{\Sigma}_0 &= \begin{bmatrix} 0.01508870 & 0 & 0 \\ 0 & 0.01531271 & 0 \\ 0 & 0 & 0.02546091 \end{bmatrix}.\end{aligned} \tag{A.16}$$

The target intervals are chosen to be $\mathbb{Y} = [-5, -4]$ when $t_f = 0.1$s and $\mathbb{Y} = [-0.22, -0.21]$ when $t_f = 5$s.

A.1.5.1 Implementation

This system is chaotic with maximal Lyapunov exponent $\lambda \approx 0.906$. We perform the optimization with MATLAB's inbuilt `fminunc` algorithm using analytically derived gradients.

A.1.6 Elliptic PDE

In this experiment, we invert for the log permeability field, g in the following elliptic PDE:

$$\begin{aligned} -\nabla \cdot (e^g \nabla u) &= h \text{ in } \Omega, \\ u &= u_D \text{ on } \partial\Omega_D, \\ e^g \nabla u \cdot \boldsymbol{n} &= u_N \text{ on } \partial\Omega_N, \end{aligned} \tag{A.17}$$

where $\Omega \subset \mathbb{R}^2$ is an open domain with boundary $\partial\Omega = \partial\Omega_D \cup \partial\Omega_N$, $\partial\Omega_D \cap \partial\Omega_N = \emptyset$. $\partial\Omega_D$ and $\partial\Omega_N$ denote Dirichlet and Neumann type boundaries with boundary values u_D and u_N respectively. $\boldsymbol{n}$ is a unit vector normal to $\partial\Omega$ in the outward direction and $h \in L^2(\Omega)$ is the source term.

We assume Ω is a unit square, there is no source term, the left and right walls are no-flux boundaries, and the top and bottom walls are Dirichlet boundaries. That is,

$$\begin{aligned} \Omega &= [0,1] \times [0,1], \\ h &= 0, \\ \partial\Omega_D &= (0,1) \times \{1\} \cup (0,1) \times \{0\}, \\ \partial\Omega_N &= \{0,1\} \times (0,1), \\ u_N &= 0, \\ u_D &= \begin{cases} 1, & \boldsymbol{x} \in (0,1) \times \{1\} \\ 0, & \boldsymbol{x} \in (0,1) \times \{0\} \end{cases}. \end{aligned} \tag{A.18}$$

This is an instance of Bayesian inference in infinite dimensions. The problem can be reduced to finite dimensions by using, for instance, a finite element discretization. The inference is then performed for the vector of coefficients of the finite element basis functions chosen. Here, we use first order Lagrange basis functions with 4225 degrees of freedom. Thus, the

parameter vector then is the vector of coefficients $\boldsymbol{m} = (g_1, g_2, \ldots, g_m) \in \mathbb{R}^m, m = 4225$. We define the parameter-to-observable map as the fluid velocity at a particular location in the domain Ω, $f(\boldsymbol{m}) = u(0.1, 0.5)$.

To solve the inverse problem, we use `hIPPYlib` [89, 90]. `hIPPYlib` is a scalable software framework to solve large scale PDE constrained inverse problems. It relies on `FEniCS` for the discretization and solution of the PDE and `PETSc` for efficient implementation of linear algebra routines. `hIPPYlib` provides state-of-the-art algorithms for PDE constrained optimization, including an implementation of the Inexact Newton-CG algorithm for computing the MAP point as well as randomized algorithms for constructing a low rank approximation of the Hessian at the MAP point. For full details, we refer the reader to [89, 90]. We would like to remark here that this inverse problem appears as a model problem in [90] and has been slightly modified for our experiments. For completeness, we reproduce relevant details from here.

While constructing $p(\boldsymbol{m})$, it was assumed that the true log-permeability at 5 locations in $\Omega = [0,1] \times [0,1]\,, \boldsymbol{\omega}_1 = (0.1, 0.1), \boldsymbol{\omega}_2 = (0.1, 0.9), \boldsymbol{\omega}_3 = (0.5, 0.5), \boldsymbol{\omega}_4 = (0.9, 0.1), \boldsymbol{\omega}_5 = (0.9, 0.9)$, is known. Let the true log-permeability at these points be $x^1_{\text{true}}, x^2_{\text{true}}, \ldots, x^5_{\text{true}}$. In addition, the following mollifier functions were defined

$$\delta_i(\boldsymbol{\omega}) = \exp\left(-\frac{\gamma^2}{\delta^2}\|\boldsymbol{\omega} - \boldsymbol{\omega}_i\|_{\boldsymbol{\Theta}^{-1}}\right). \tag{A.19}$$

where $\boldsymbol{\Theta}$ is an anisotropic symmetric positive definite tensor of the form

$$\boldsymbol{\Theta} = \begin{pmatrix} \theta_1 \sin^2\alpha & (\theta_1 - \theta_2)\sin\alpha\cos\alpha \\ (\theta_1 - \theta_2)\sin\alpha\cos\alpha & \theta_2\cos^2\alpha \end{pmatrix}. \tag{A.20}$$

The various parameters were set to $\gamma = 0.1, \delta = 0.5, \alpha = \pi/4, \theta_1 = 2, \theta_2 = 0.5$. The covariance of $p(\boldsymbol{m})$ was finally defined as $\boldsymbol{\Sigma}_0 = \mathcal{A}^{-2}$, where,

$$\mathcal{A} = \tilde{\mathcal{A}} + p\sum_{i=1}^{5}\delta_i\mathbf{I}, \tag{A.21}$$

$$= \tilde{\mathcal{A}} + p\mathcal{M}. \tag{A.22}$$

where $\tilde{A}$ is a differential operator of the form $\gamma\nabla\cdot(\theta\nabla)+\delta\mathbf{I}$ and p is a penalization parameter, which was set to $p = 10$.

The mean of the nominal PDF $p(\boldsymbol{m})$, $\boldsymbol{m}_0$, was set to be the solution of the following regularized least squares problem

$$\boldsymbol{m}_0 = \arg\min_{\boldsymbol{m}} = \frac{1}{2}\langle\boldsymbol{m},\boldsymbol{m}\rangle_{\tilde{\mathcal{A}}} + \frac{p}{2}\langle\boldsymbol{m}_{\text{true}}-\boldsymbol{m},\boldsymbol{m}_{\text{true}}-\boldsymbol{m}\rangle_{\mathcal{M}}. \tag{A.23}$$

The nominal distribution $p(\boldsymbol{m})$ is then defined to be $\mathcal{N}(\boldsymbol{m}_0,\boldsymbol{\Sigma}_0)$ and $\mathbb{Y} = [0.6, 0.7]$.

A.1.7 Periodic map

In this case the input-output map is defined to be:

$$f(\boldsymbol{m}) = \sin(m_1)\cos(m_2). \tag{A.24}$$

A.1.8 Implementation

Again, $p(\boldsymbol{m})$ is assumed to be a Gaussian distribution with mean $\boldsymbol{m}_0$ and covariance $\boldsymbol{\Sigma}_0$, where $\boldsymbol{m}_0 = (1,1)^T$ and $\boldsymbol{\Sigma_0} = \mathbf{I}$. We chose $\mathbb{Y} = [0.4, 0.6]$. The MAP point was computed using MATLAB's `fminunc` routine.

Appendix B

This appendix contains supporting theory for Chapter 3.

B.1 Kullback-Leibler divergence between linearized pushforwards

Recall that when a new component, say $q_k = \mathcal{N}(\boldsymbol{m}_k, \mathbf{H}_{\mathrm{GN}}^{-1})$, is added to the IS mixture in Stage-1, its covariance $\mathbf{H}_{\mathrm{GN}}^{-1}$ is dependent on σ^2:

$$\mathbf{H}_{\mathrm{GN}}^{-1} = \boldsymbol{\Sigma}_0 - \frac{1}{\sigma^2 + \nabla f(\boldsymbol{m}_k)^T \boldsymbol{\Sigma}_0 \nabla f(\boldsymbol{m}_k)} \left(\boldsymbol{\Sigma}_0 \nabla f(\boldsymbol{m}_k)\right) \left(\boldsymbol{\Sigma}_0 \nabla f(\boldsymbol{m}_k)\right)^T. \tag{B.1}$$

For each $\boldsymbol{m}_k$, A-BIMC finds a suitable value of σ^2 by

1. linearizing $f(\boldsymbol{m})$ around $\boldsymbol{m}_k$ to obtain $f^{\mathrm{lin}}(\boldsymbol{m}) = \nabla f(\boldsymbol{m}_k)^T(\boldsymbol{m} - \boldsymbol{m}_k) + f(\boldsymbol{m}_k)$
2. computing the push-forward densities of q_k and q^* under f^{lin}, denoted $q_{k,\natural}$ and $q_\natural^*$.
3. setting $\sigma = \sigma^*$ in Equation (B.1), where $\sigma^* = \arg\min D_{\mathrm{KL}}(q_\natural^* || q_{k,\natural})$

In this section, we derive expressions for $D_{\mathrm{KL}}(q_\natural^* || q_{k,\natural})$ and σ^*. To begin with, notice that the univariate densities $q_\natural^*$ and $q_{k,\natural}$ have the following functional form:

$$q_\natural^*(z) = \frac{\mathbf{1}_{\mathbb{Y}}(z)}{\mu} \mathcal{N}\left(z; f^{\mathrm{lin}}(\boldsymbol{m}_0), \nabla f(\boldsymbol{m}_k)^T \boldsymbol{\Sigma}_0 \nabla f(\boldsymbol{m}_k)\right)$$
$$q_{k,\natural}(z) = \mathcal{N}\left(z; f(\boldsymbol{m}_k), \frac{\sigma^2 \nabla f(\boldsymbol{m}_k)^T \boldsymbol{\Sigma}_0 \nabla f(\boldsymbol{m}_k)}{\sigma^2 + \nabla f(\boldsymbol{m}_k)^T \boldsymbol{\Sigma}_0 \nabla f(\boldsymbol{m}_k)}\right).$$

Hence, the push-forward of q^*, $q^*_\natural$, is the Normal distribution $\mathcal{N}\left(f^{\text{lin}}(\boldsymbol{m}_0), \nabla f(\boldsymbol{m}_k)^T \boldsymbol{\Sigma}_0 \nabla f(\boldsymbol{m}_k)\right)$ truncated over the interval $\mathbb{Y}$. Further, $\mathcal{N}\left(f^{\text{lin}}(\boldsymbol{m}_0), \nabla f(\boldsymbol{m}_k)^T \boldsymbol{\Sigma}_0 \nabla f(\boldsymbol{m}_k)\right)$ is nothing but the push-forward of p under f^{lin}. Denoting this push-forward by $p_\natural$, $q^*_\natural$ can be expressed more succinctly as $q^*_\natural(z) = \mathbf{1}_{\mathbb{Y}}(z) p_\natural(z)/\mu$.

Symbol	Meaning
$\boldsymbol{v}_k$	$\nabla f(\boldsymbol{m}_k)$
ρ	$\sigma/\sqrt{\sigma^2 + \nabla f(\boldsymbol{m}_k)^T \boldsymbol{\Sigma}_0 \nabla f(\boldsymbol{m}_k)}$
ν_T	mean of $q^*_\sharp$
γ_T^2	variance of $q^*_\sharp$

Table B.1: *Symbols used in Section B.1*

For the remainder of this section, we shall use the symbols defined in Table B.1. From the definition of K-L divergence, we have,

$$\begin{aligned} D_{\text{KL}}(q^*_\natural || q_{k,\natural}) &= \int_{\mathbb{R}} \frac{\mathbf{1}_{\mathbb{Y}}(z)}{\mu} \log \frac{\mathbf{1}_{\mathbb{Y}}(z)}{\mu} \frac{p_\sharp(z)}{q_{k,\sharp}(z)} \mathrm{d}z \\ &= \frac{1}{\mu} \int_{\mathbb{Y}} p_\natural(z) \log \frac{p_\natural(z)}{q_{k,\natural}(z)} \mathrm{d}z - \log \mu. \end{aligned} \tag{B.2}$$

Now, it can be shown that

$$\log \frac{p_\natural(z)}{q_{k,\natural}(z)} = \log \rho + \frac{1}{2\rho^2 \boldsymbol{v}_k^T \boldsymbol{\Sigma}_0 \boldsymbol{v}_k} \left(z - f(\boldsymbol{m}_k)\right)^2 - \frac{1}{2\boldsymbol{v}_k^T \boldsymbol{\Sigma}_0 \boldsymbol{v}_k} \left(z - f^{\text{lin}}(\boldsymbol{m}_0)\right)^2 \tag{B.3}$$

Plugging Equation (B.3) into Equation (B.2) and using the definition of $q^*_\sharp$, we obtain

$$\begin{aligned} D_{\text{KL}}(q^*_\natural || q_{k,\natural}) = &\log \rho - \log \mu \\ &+ \frac{1}{2\rho^2 \boldsymbol{v}_k^T \boldsymbol{\Sigma}_0 \boldsymbol{v}_k} \mathbb{E}_{q^*_\natural} \left[\left(z - f(\boldsymbol{m}_k)\right)^2\right] \\ &- \frac{1}{2\boldsymbol{v}_k^T \boldsymbol{\Sigma}_0 \boldsymbol{v}_k} \mathbb{E}_{q^*_\natural} \left[\left(z - f^{\text{lin}}(\boldsymbol{m}_0)\right)^2\right] \end{aligned} \tag{B.4}$$

The expectations with respect to $q_\sharp^*$ in Equation (B.4) can be related to the mean ν_T and variance γ_T^2 of $q_\sharp^*$. This leads to the following expression for the KL divergence between the push-forwards

$$\begin{aligned} D_{\mathrm{KL}}(q_\natural^* || q_{k,\natural}) = &\log \rho - \log \mu + \frac{\gamma_T^2}{2\sigma^2} \\ &+ \frac{1}{2\rho^2 \boldsymbol{v}_k^T \boldsymbol{\Sigma}_0 \boldsymbol{v}_k} \left[\nu_T - f(\boldsymbol{m}_k)\right]^2 \\ &- \frac{1}{2\boldsymbol{v}_k^T \boldsymbol{\Sigma}_0 \boldsymbol{v}_k} \left[\nu_T - f^{\mathrm{lin}}(\boldsymbol{m}_0)\right]^2 \end{aligned} \tag{B.5}$$

The value of σ that minimizes this equation is:

$$\sigma^* = \frac{\boldsymbol{v}_k^T \boldsymbol{\Sigma}_0 \boldsymbol{v}_k \left(\gamma_T^2 + (\nu_T - f(\boldsymbol{m}_k))^2\right)}{\boldsymbol{v}_k^T \boldsymbol{\Sigma}_0 \boldsymbol{v}_k - \gamma_T^2 - (\nu_T - f(\boldsymbol{m}_k))^2} \tag{B.6}$$

B.2 Relationship between e_{RMS} and ESS

This section establishes that the sample estimate of the relative RMSE, $\tilde{e}_{\mathrm{RMS}}^N$, and the Effective Sample Size are closely related, and in fact, are different ways of expressing the mismatch between the ideal importance sampling density q^* and the importance sampling density Q.

Let $\boldsymbol{X}_1, \ldots, \boldsymbol{X}_N \overset{\text{i.i.d.}}{\sim} Q(\boldsymbol{m})$ be i.i.d. samples from Q. Start by defining the normalized IS weights as follows:

$$\bar{w}_i = \frac{\mathbf{1}_{\mathbb{Y}}(f(\boldsymbol{X}_i)) p(\boldsymbol{X}_i)/q(\boldsymbol{X}_i)}{\sum_j \mathbf{1}_{\mathbb{Y}}(f(\boldsymbol{X}_j)) p(\boldsymbol{X}_j)/q(\boldsymbol{X}_j)}$$

Noticing that the denominator $\sum_j \mathbf{1}_{\mathbb{Y}}(f(\boldsymbol{X}_j)) p(\boldsymbol{X}_j)/q(\boldsymbol{X}_j)$ is nothing but $N\tilde{\mu}^N$, we have,

$$\bar{w}_i = \frac{\mathbf{1}_{\mathbb{Y}}(f(\boldsymbol{X}_i))p(\boldsymbol{X}_i)/q(\boldsymbol{X}_i)}{N\tilde{\mu}^N}.$$

We use the function-specific ESS introduced in [63]:

$$\text{ESS} = \frac{1}{\sum_i \bar{w}_i^2} = \frac{(N\tilde{\mu}^N)^2}{\sum_i \mathbf{1}_{\mathbb{Y}}(f(\boldsymbol{X}_i))p^2(\boldsymbol{X}_i)/q^2(\boldsymbol{X}_i)},$$

and define the normalized-ESS as ESS/N:

$$\frac{\text{ESS}}{N} = \frac{(\tilde{\mu}^N)^2}{\frac{1}{N}\sum_i \mathbf{1}_{\mathbb{Y}}(f(\boldsymbol{X}_i))p^2(\boldsymbol{X}_i)/q^2(\boldsymbol{X}_i)}$$

Recall from Equation (2.2) that the relative Root Mean Square Error is defined as:

$$e_{\text{RMS}} = \sqrt{\frac{\mathbb{V}_q\left[\mathbf{1}_{\mathbb{Y}}(f(\boldsymbol{m})p(\boldsymbol{m})/q(\boldsymbol{m}))\right]}{\mu^2 N}}$$

Approximating $\mathbb{V}_q\left[\mathbf{1}_{\mathbb{Y}}(f(\boldsymbol{m})p(\boldsymbol{m})/q(\boldsymbol{m}))\right]$ and μ via samples leads to the following estimate for the relative RMSE:

$$\begin{aligned}\tilde{e}^N_{\text{RMS}} &= \sqrt{\frac{1}{N}\left(\frac{\sum_i \mathbf{1}_{\mathbb{Y}}(f(\boldsymbol{X}_i))p(\boldsymbol{X}_i)^2/q(\boldsymbol{X}_i)^2}{N(\tilde{\mu}^N)^2} - 1\right)} \\ &= \sqrt{\frac{1}{N}\left(\frac{N}{\text{ESS}} - 1\right)}\end{aligned}$$

Alternatively,

$$\frac{\text{ESS}}{N} = \frac{1}{N(\tilde{e}^N_{\text{RMS}})^2 + 1} \tag{B.7}$$

The reason why ESS and e^N_{RMS} are directly related is that they're both dependent on the χ^2-divergence between q^* and Q. The χ^2-divergence between two probability distributions, like the Kullback-Leibler divergence, is a measure of the distance between two probability distributions. For instance, the χ^2-divergence between q^* and Q is defined as:

$$D_{\chi^2} = \int \left(\frac{q^*(\boldsymbol{m})}{Q(\boldsymbol{m})} - 1 \right)^2 Q(\boldsymbol{m}) \mathrm{d}\boldsymbol{m}$$

And once again, a sample estimate of D_{χ^2}, denoted $\tilde{D}_{\chi^2}$ can be computed as:

$$\tilde{D}_{\chi^2} = \frac{1}{(\tilde{\mu}^N)^2} \left(\frac{1}{N} \sum_i \mathbf{1}_{\mathbb{Y}}(f(\boldsymbol{X}_i)) p(\boldsymbol{X}_i)^2 / q(\boldsymbol{X}_i)^2 - 1 \right)$$

Straightforward manipulations lead to:

$$\begin{aligned} \tilde{e}^N_{\text{RMS}} &= \sqrt{\frac{\tilde{D}_{\chi^2}}{N}} \\ \frac{\text{ESS}}{N} &= \frac{1}{\tilde{D}_{\chi^2} + 1} \end{aligned}$$

Hence, e^N_{RMS} and the normalized-ESS are just different ways of expressing the mismatch between q^* and Q, as measured by the χ^2-divergence. As a result, one does not contain more information over the other. Note that the existence of such a relationship isn't totally unexpected, and has in fact been established elsewhere for other settings in which importance sampling is employed. In [2], a similar relationship is derived, but for the autonormalized IS estimator. Again in [78], a very similar relationship is derived, but under the assumption that importance sampling is being employed to approximate some intractable target distribution. As a result, their derivation is agnostic of the function being integrated. Ignoring

the integrand, which would translate to the indicator function $\mathbf{1}_{\mathbb{Y}}(f(\boldsymbol{m}))$, in the rare-event setting will not yield meaningful relationships. Indeed, it is due to the highly non-linear nature of the indicator function that rare-event probability estimation is so notoriously difficult. Here, we've shown that this relationship exists in the the rare-event setting as well, but between the relative RMSE, and the rare-event (or function-) specific ESS defined in [63].

Appendix C

This appendix contains omitted theoretical details and a description of our MCMC workflow from Chapter 4.

C.1 Derivation of the governing equations

We begin by expanding each term in the LHS of Equation (4.1):

$$\frac{\partial \phi \rho_\alpha S_\alpha}{\partial t} = \rho_\alpha S_\alpha \frac{\partial \phi}{\partial t} + \phi \rho_\alpha S_\alpha \frac{\partial \rho_\alpha}{\partial t} + \phi \rho_\alpha \frac{\partial S_\alpha}{\partial t} \tag{C.1}$$

$$= \phi \rho_\alpha S_\alpha c_r \frac{\partial p}{\partial t} + \phi \rho_\alpha S_\alpha c_\alpha \frac{\partial p}{\partial t} + \phi \rho_\alpha \frac{\partial S_\alpha}{\partial t}, \quad \text{and,} \tag{C.2}$$

$$\nabla \cdot (\rho_\alpha \boldsymbol{v}_\alpha) = \rho_\alpha \nabla \cdot \boldsymbol{v}_\alpha + \boldsymbol{v}_\alpha \cdot (c_\alpha \rho_\alpha \nabla p), \tag{C.3}$$

where we've used chain rule and the definition of ϕ and c_α. This leads to:

$$\phi \rho_\alpha (S_\alpha c_r + S_\alpha c_\alpha) \frac{\partial p}{\partial t} + \phi \rho_\alpha \frac{\partial S_\alpha}{\partial t} + \rho_\alpha \nabla \cdot \boldsymbol{v}_\alpha + \rho_\alpha c_\alpha \boldsymbol{v}_\alpha \cdot \nabla p = \rho_\alpha q_\alpha \tag{C.4}$$

Now, dividing Equation (C.4) by ρ_α for each phase and adding the resulting equations together yields:

$$\phi (c_r + S_w c_w + S_n c_n) \frac{\partial p}{\partial t} + \nabla \cdot \boldsymbol{v} + (c_w \boldsymbol{v}_w + c_n \boldsymbol{v}_n) \cdot \nabla p = q_w + q_n \tag{C.5}$$

Using Darcy's law (Equation (4.2)) for each phase, and the definition of total velocity, $\boldsymbol{v} = \boldsymbol{v}_w + \boldsymbol{v}_o$, we finally get:

$$\phi\left(c_r + (1 - S_w)c_n + S_w c_w\right)\frac{\partial p}{\partial t} + \nabla \cdot \boldsymbol{v} - \left[c_w \lambda_w + c_n \lambda_o\right]\frac{\boldsymbol{v} \cdot \boldsymbol{v}}{\left(\lambda_w + \lambda_o\right)^2 K} = q_w + q_n \tag{C.6}$$

C.2 MCMC Workflow

We briefly describe our MCMC workflow in this section. For each scenario in Section 4.5.1, we generate a single MCMC chain starting at the MAP estimate of the transmissibilities $\boldsymbol{m}_{\text{MAP}}$ using the pCN algorithm. The pCN algorithm requires a user-specified parameter, $\beta \in [0, 1]$, which controls the spatial scale at which the Markov chain explores the posterior. We select β so that the acceptance ratio remains between 20% to 40% in each scenario.

The MCMC chain contains correlated samples from the posterior. We use the notion of an Effective Sample Size (ESS, denoted n_{ESS}) to estimate the number of independent samples obtained from the posterior distribution. The ESS is inextricably linked to the quantity whose statistics are desired, hence, we use the discounted oil production V, which, recall, depends implicitly on the fault transmissibilities $\boldsymbol{m}$. The ESS is defined as:

$$n_{\text{ESS}} = \frac{N}{1 + 2\sum_{l=1}^{\infty} \rho_l[V]}, \tag{C.7}$$

where N is the total number of samples in the Markov chain, ρ_l is the lag-l autocorrelation in V:

$$\rho_l[V] = \frac{\mathbb{E}\left[\left[V[\boldsymbol{m}_{n+l}] - \mathbb{E}_{\pi_{\text{post}}}[V]\right]\left[V[\boldsymbol{m}_l] - \mathbb{E}_{\pi_{\text{post}}}[V]\right]\right]}{\mathbb{V}_{\pi_{\text{post}}}[V]}. \tag{C.8}$$

In practice, the ESS is computed empirically – the expectations in Equation (C.8) are approximated using samples from the Markov chain. Furthermore, the summation in the denominator of Equation (C.7) is truncated at some maximum lag k. To determine the

cutoff lag k, we follow one of the recommendations in [38], truncating the autocorrelation when the sum of neighboring pairs, $\rho_{2l} + \rho_{2l+1}$, becomes negative.

A related measure of the independence between Markov chain iterates is its relaxation time, defined as $\tau_R = n_{\text{ESS}}^{-1}$. This is the time required by the Markov chain to produce an independent sample from the posterior. In our plots, we plot every τ_R sample from the Markov chain, both for the fault log-permeabilities (which, up to a constant, is the fault log-transmissibility), as well as the QoI.

Our estimates of the KL divergence in Table 4.3 are computed using a simple Monte Carlo method. We use the kernel density estimate of the posterior-predictive distribution $\pi_{\text{post}}^{\natural}$ to generate independent samples $v_1, \ldots, v_N$. Then, then the Monte Carlo estimate of the KL divergence between $\pi_{\text{post}}^{\natural}$ and, say, $\pi_{\text{laplace}}^{\natural}$ is:

$$\hat{D}_{\text{KL}}(\pi_{\text{post}}^{\natural} || \pi_{\text{laplace}}^{\natural}) = \frac{1}{N} \sum_{i=1}^{N} \log \frac{\pi_{\text{post}}^{\natural}(v_i)}{\pi_{\text{laplace}}^{\natural}(v_i)} \tag{C.9}$$

For the estimates in Table 4.3, we used $N = 10^4$.

Bibliography

[1] Sigurd I Aanonsen, Geir Nævdal, Dean S Oliver, Albert C Reynolds, Brice Vallès, et al. The ensemble Kalman filter in reservoir engineering - a review. *SPE Journal*, 14(03):393–412, 2009.

[2] S. Agapiou, O. Papaspiliopoulos, D. Sanz-Alonso, and A. M. Stuart. Importance sampling: Intrinsic dimension and computational cost. *Statist. Sci.*, 32(3):405–431, 08 2017.

[3] B Agarwal, H Hermansen, JE Sylte, LK Thomas, et al. Reservoir characterization of Ekofisk field: a giant, fractured chalk reservoir in the Norwegian North sea - history match. In *SPE Reservoir Simulation Symposium*. Society of Petroleum Engineers, 1999.

[4] Elyes Ahmed, Jerome Jaffre, and Jean E. Roberts. A reduced fracture model for two-phase flow with different rock types. *Mathematics and Computers in Simulation*, 137:49 – 70, 2017. MAMERN VI-2015: 6th International Conference on Approximation Methods and Numerical Modeling in Environment and Natural Resources.

[5] Volkan Akçelik, George Biros, Omar Ghattas, Judith Hill, David Keyes, and Bart van Bloemen Waanders. Parallel algorithms for PDE-constrained optimization. In *Parallel Processing for Scientific Computing*, pages 291–322. SIAM, 2006.

[6] Martin S. Alnæs, Jan Blechta, Johan Hake, August Johansson, Benjamin Kehlet, Anders Logg, Chris Richardson, Johannes Ring, Marie E. Rognes, and Garth N. Wells. The FEniCS Project Version 1.5. *Archive of Numerical Software*, 3(100), 2015.

[7] Philippe Angot, Franck Boyer, and Florence Hubert. Asymptotic and numerical modelling of flows in fractured porous media. *ESAIM: Mathematical Modelling and Numerical Analysis*, 43(2):239–275, 2009.

[8] Todd Arbogast. Analysis of the simulation of single phase flow through a naturally fractured reservoir. *SIAM Journal on Numerical Analysis*, 26(1):12–29, 1989.

[9] Siu-Kui Au and James L. Beck. Estimation of small failure probabilities in high dimensions by subset simulation. *Probabilistic Engineering Mechanics*, 16(4):263 – 277, 2001.

[10] S.K. Au and J.L. Beck. A new adaptive importance sampling scheme for reliability calculations. *Structural Safety*, 21(2):135 – 158, 1999.

[11] S.K. Au, C. Papadimitriou, and J.L. Beck. Reliability of uncertain dynamical systems with multiple design points. *Structural Safety*, 21(2):113 – 133, 1999.

[12] Satish Balay, Shrirang Abhyankar, Mark F. Adams, Jed Brown, Peter Brune, Kris Buschelman, Lisandro Dalcin, Alp Dener, Victor Eijkhout, William D. Gropp, Dmitry Karpeyev, Dinesh Kaushik, Matthew G. Knepley, Dave A. May, Lois Curfman McInnes, Richard Tran Mills, Todd Munson, Karl Rupp, Patrick Sanan, Barry F. Smith, Stefano Zampini, Hong Zhang, and Hong Zhang. PETSc users manual. Technical Report ANL-95/11 - Revision 3.12, Argonne National Laboratory, 2019.

[13] Grigory I Barenblatt, Iu P Zheltov, and IN Kochina. Basic concepts in the theory of seepage of homogeneous liquids in fissured rocks [strata]. *Journal of Applied Mathematics and Mechanics*, 24(5):1286–1303, 1960.

[14] J. Breidt, T. Butler, and D. Estep. A Measure-Theoretic Computational Method for Inverse Sensitivity Problems I: Method and Analysis. *SIAM Journal on Numerical Analysis*, 49(5):1836–1859, 2011.

[15] Christian G. Bucher. Adaptive sampling - an iterative fast monte carlo procedure. *Structural Safety*, 5(2):119 – 126, 1988.

[16] Tan Bui-Thanh, Omar Ghattas, James Martin, and Georg Stadler. A computational framework for infinite-dimensional Bayesian inverse problems Part I: The linearized case, with application to global seismic inversion. *SIAM Journal on Scientific Computing*, 35(6):A2494–A2523, 2013.

[17] T. Butler, D. Estep, and J. Sandelin. A Computational Measure Theoretic Approach to Inverse Sensitivity Problems II: A Posteriori Error Analysis. *SIAM Journal on Numerical Analysis*, 50(1):22–45, 2012.

[18] Olivier Cappé, Randal Douc, Arnaud Guillin, Jean-Michel Marin, and Christian P. Robert. Adaptive importance sampling in general mixture classes. *Statistics and Computing*, 18(4):447–459, Dec 2008.

[19] Sourav Chatterjee and Persi Diaconis. The sample size required in importance sampling. *Ann. Appl. Probab.*, 28(2):1099–1135, 04 2018.

[20] Yan Chen and Dean S Oliver. Ensemble randomized maximum likelihood method as an iterative ensemble smoother. *Mathematical Geosciences*, 44(1):1–26, 2012.

[21] Yan Chen, Dean S Oliver, et al. Ensemble-based closed-loop optimization applied to Brugge field. *SPE Reservoir Evaluation & Engineering*, 13(01):56–71, 2010.

[22] Zhangxin Chen, Guanren Huan, and Yuanle Ma. *Computational methods for multiphase flows in porous media*, volume 2. SIAM, 2006.

[23] K Andrew Cliffe, Mike B Giles, Robert Scheichl, and Aretha L Teckentrup. Multilevel Monte Carlo methods and applications to elliptic PDEs with random coefficients. *Computing and Visualization in Science*, 14(1):3, 2011.

[24] Paul G Constantine. *Active subspaces: Emerging ideas for dimension reduction in parameter studies*, volume 2. SIAM, 2015.

[25] Simon L Cotter, Gareth O Roberts, Andrew M Stuart, and David White. MCMC methods for functions: modifying old algorithms to make them faster. *Statistical Science*, pages 424–446, 2013.

[26] Tiangang Cui, James Martin, Youssef M Marzouk, Antti Solonen, and Alessio Spantini. Likelihood-informed dimension reduction for nonlinear inverse problems. *Inverse Problems*, 30(11):114015, 2014.

[27] Pieter-Tjerk De Boer, Dirk P Kroese, Shie Mannor, and Reuven Y Rubinstein. A tutorial on the cross-entropy method. *Annals of Operations Research*, 134(1):19–67, 2005.

[28] A. P. Dempster, N. M. Laird, and D. B. Rubin. Maximum Likelihood from Incomplete Data via the EM Algorithm. *Journal of the Royal Statistical Society. Series B (Methodological)*, 39(1):1–38, 1977.

[29] Yalchin Efendiev, Thomas Hou, and Wuan Luo. Preconditioning markov chain monte carlo simulations using coarse-scale models. *SIAM Journal on Scientific Computing*, 28(2):776–803, 2006.

[30] Clement Etienam, Intesar Mahmood, Rossmary Villegas, et al. History matching of Reservoirs by Updating Fault Properties Using 4D Seismic Results and Ensemble Kalman Filter. In *SPE Europec featured at 79th EAGE Conference and Exhibition*. Society of Petroleum Engineers, 2017.

[31] Clement Etienam, Intesar Mahmood, Rossmary Villegas, et al. The effect of including History matching of Reservoirs by Updating Fault Properties Using 4D Seismic Results and Ensemble Kalman Filter. 2017.

[32] Geir Evensen, Joakim Hove, Hilde Meisingset, Edel Reiso, Knut Sponheim Seim, Øystein Espelid, et al. Using the EnKF for assisted history matching of a North Sea reservoir model. In *SPE reservoir simulation symposium*. Society of Petroleum Engineers, 2007.

[33] Matteo Fasiolo, Flávio Eler de Melo, and Simon Maskell. Langevin incremental mixture importance sampling. *Statistics and Computing*, 28(3):549–561, 2018.

[34] Luca Formaggia, Alessio Fumagalli, Anna Scotti, and Paolo Ruffo. A reduced model for Darcy's problem in networks of fractures. *ESAIM: Mathematical Modelling and Numerical Analysis*, 48(4):1089–1116, 2014.

[35] Najla Frih, Vincent Martin, Jean Elizabeth Roberts, and Ali Saâda. Modeling fractures as interfaces with nonmatching grids. *Computational Geosciences*, 16(4):1043–1060, 2012.

[36] Alessio Fumagalli and Anna Scotti. A numerical method for two-phase flow in fractured porous media with non-matching grids. *Advances in Water Resources*, 62:454–464, 2013.

[37] Christophe Geuzaine and Jean-François Remacle. Gmsh: A 3-D finite element mesh generator with built-in pre-and post-processing facilities. *International Journal for Numerical Methods in Engineering*, 79(11):1309–1331, 2009.

[38] Charles J Geyer. Practical Markov Chain Monte Carlo. *Statistical Science*, pages 473–483, 1992.

[39] Mark Girolami and Ben Calderhead. Riemann manifold langevin and hamiltonian monte carlo methods. *Journal of the Royal Statistical Society: Series B (Statistical Methodology)*, 73(2):123–214, 2011.

[40] Yaqing Gu, Dean S Oliver, et al. An iterative ensemble Kalman filter for multiphase fluid flow data assimilation. *SPE Journal*, 12(04):438–446, 2007.

[41] M. Gunzburger. *Perspectives in Flow Control and Optimization*. Society for Industrial and Applied Mathematics, 2002.

[42] J. R. Hershey and P. A. Olsen. Approximating the Kullback Leibler Divergence Between Gaussian Mixture Models. In *2007 IEEE International Conference on Acoustics, Speech and Signal Processing - ICASSP '07*, volume 4, pages IV–317–IV–320, April 2007.

[43] Matthew D Hoffman and Andrew Gelman. The No-U-Turn sampler: adaptively setting path lengths in Hamiltonian Monte Carlo. *Journal of Machine Learning Research*, 15(1):1593–1623, 2014.

[44] Hussein Hoteit and Abbas Firoozabadi. Multicomponent fluid flow by discontinuous Galerkin and mixed methods in unfractured and fractured media. *Water Resources Research*, 41(11), 2005.

[45] Hussein Hoteit and Abbas Firoozabadi. An efficient numerical model for incompressible two-phase flow in fractured media. *Advances in Water Resources*, 31(6):891–905, 2008.

[46] Tobin Isaac, Noemi Petra, Georg Stadler, and Omar Ghattas. Scalable and efficient algorithms for the propagation of uncertainty from data through inference to prediction for large-scale problems, with application to flow of the Antarctic ice sheet. *Journal of Computational Physics*, 296:348–368, 2015.

[47] Herman Kahn and Andy W Marshall. Methods of reducing sample size in Monte Carlo computations. *Journal of the Operations Research Society of America*, 1(5):263–278, 1953.

[48] LS Katafygiotis and KM Zuev. Estimation of small failure probabilities in high dimensions by adaptive linked importance sampling. *COMPDYN 2007*, 2007.

[49] Boris Kramer, Alexandre Noll Marques, Benjamin Peherstorfer, Umberto Villa, and Karen Willcox. Multifidelity probability estimation via fusion of estimators. Technical Report ACDL TR-2017-3, Massachusetts Institute of Technology, 2017.

[50] Pierre Simon Laplace. Memoir on the probability of the causes of events. *Statist. Sci.*, 1(3):364–378, 08 1986.

[51] Knut-Andreas Lie. *An introduction to reservoir simulation using MATLAB/GNU Octave: User guide for the MATLAB Reservoir Simulation Toolbox (MRST)*. Cambridge University Press, 2019.

[52] Chad Lieberman and Karen Willcox. Goal-Oriented Inference: Approach, Linear Theory, and Application to Advection Diffusion. *SIAM Review*, 55(3):493–519, 2013.

[53] Chad Lieberman and Karen Willcox. Nonlinear goal-oriented Bayesian inference: Application to carbon capture and storage. *SIAM Journal on Scientific Computing*, 36(3):B427–B449, 2014.

[54] Edward N Lorenz. Deterministic nonperiodic flow. *Journal of the Atmospheric Sciences*, 20(2):130–141, 1963.

[55] James Martin, Lucas C Wilcox, Carsten Burstedde, and Omar Ghattas. A stochastic Newton MCMC method for large-scale statistical inverse problems with application to seismic inversion. *SIAM Journal on Scientific Computing*, 34(3):A1460–A1487, 2012.

[56] Vincent Martin, Jérôme Jaffré, and Jean E Roberts. Modeling fractures and barriers as interfaces for flow in porous media. *SIAM Journal on Scientific Computing*, 26(5):1667–1691, 2005.

[57] R.E. Melchers. Importance sampling in structural systems. *Structural Safety*, 6(1):3 – 10, 1989.

[58] Kevin P. Murphy. *Machine learning a probabilistic perspective / Kevin P. Murphy.* Adaptive computation and machine learning series. MIT Press, Cambridge, MA.

[59] Jorge Nocedal and Stephen Wright. *Numerical optimization.* Springer Science & Business Media, 2006.

[60] Tinsley Oden, Robert Moser, and Omar Ghattas. Computer Predictions with Quantified Uncertainty, Part I. *SIAM News*, 43(9), 2010.

[61] Dean S Oliver and Yan Chen. Recent progress on reservoir history matching: a review. *Computational Geosciences*, 15(1):185–221, 2011.

[62] Dean S Oliver, Luciane B Cunha, and Albert C Reynolds. Markov chain Monte Carlo methods for conditioning a permeability field to pressure data. *Mathematical geology*, 29(1):61–91, 1997.

[63] Art B. Owen. *Monte Carlo theory, methods and examples.* 2013.

[64] Matthew D Parno and Youssef M Marzouk. Transport map accelerated Markov chain Monte Carlo. *SIAM/ASA Journal on Uncertainty Quantification*, 6(2):645–682, 2018.

[65] B. Peherstorfer, B. Kramer, and K. Willcox. Multifidelity preconditioning of the cross-entropy method for rare event simulation and failure probability estimation. *SIAM/ASA Journal on Uncertainty Quantification*, 2018.

[66] Benjamin Peherstorfer, Tiangang Cui, Youssef Marzouk, and Karen Willcox. Multifidelity importance sampling. *Computer Methods in Applied Mechanics and Engineering*, 300:490 – 509, 2016.

[67] Noemi Petra, James Martin, Georg Stadler, and Omar Ghattas. A computational framework for infinite-dimensional Bayesian inverse problems, Part II: Stochastic Newton MCMC with application to ice sheet flow inverse problems. *SIAM Journal on Scientific Computing*, 36(4):A1525–A1555, 2014.

[68] Frank J Pinski, Gideon Simpson, Andrew M Stuart, and Hendrik Weber. Algorithms for Kullback–Leibler approximation of probability measures in infinite dimensions. *SIAM Journal on Scientific Computing*, 37(6):A2733–A2757, 2015.

[69] S. B. Pope and M. S. Anand. Flamelet and distributed combustion in premixed turbulent flames. In *Symposium (International) on Combustion*, volume 20, pages 403–410. Elsevier, 1985.

[70] Rüdiger Rackwitz. Reliability analysis - a review and some perspectives. *Structural Safety*, 23(4):365 – 395, 2001.

[71] Adrian E Raftery and Le Bao. Estimating and projecting trends in HIV/AIDS generalized epidemics using incremental mixture importance sampling. *Biometrics*, 66(4):1162–1173, 2010.

[72] Volker Reichenberger, Hartmut Jakobs, Peter Bastian, and Rainer Helmig. A mixed-dimensional finite volume method for two-phase flow in fractured porous media. *Advances in water resources*, 29(7):1020–1036, 2006.

[73] Christian Robert and George Casella. *Monte Carlo statistical methods*. Springer Science & Business Media, 2013.

[74] Christian P. Robert and George Casella. *Monte Carlo Integration*, pages 79–122. Springer New York, New York, NY, 2004.

[75] Gareth O Roberts, Richard L Tweedie, et al. Exponential convergence of Langevin distributions and their discrete approximations. *Bernoulli*, 2(4):341–363, 1996.

[76] CE Romero and JN Carter. Using genetic algorithms for reservoir characterisation. *Journal of Petroleum Science and engineering*, 31(2-4):113–123, 2001.

[77] Gerardo Rubino and Bruno Tuffin. *Rare event simulation using Monte Carlo methods*. John Wiley & Sons, 2009.

[78] D. Sanz-Alonso. Importance sampling and necessary sample size: An information theory approach. *SIAM/ASA Journal on Uncertainty Quantification*, 6(2):867–879, 2018.

[79] Claudia Schillings, Björn Sprungk, and Philipp Wacker. On the Convergence of the Laplace Approximation and Noise-Level-Robustness of Laplace-based Monte Carlo Methods for Bayesian Inverse Problems. *arXiv preprint arXiv:1901.03958*, 2019.

[80] G.I. Schuëller and R. Stix. A critical appraisal of methods to determine failure probabilities. *Structural Safety*, 4(4):293 – 309, 1987.

[81] RW Schulze-Riegert, O Haase, A Nekrassov, et al. Combined global and local optimization techniques applied to history matching. In *SPE Reservoir Simulation Symposium*. Society of Petroleum Engineers, 2003.

[82] Alexandra Seiler, Geir Evensen, Jan-Arild Skjervheim, Joakim Hove, Jon Gustav Vabo, et al. Advanced reservoir management workflow using an EnKF based assisted history matching method. In *SPE Reservoir Simulation Symposium*. Society of Petroleum Engineers, 2009.

[83] Alexandra Seiler, Jan C Rivenæs, Sigurd Ivar Aanonsen, and Geir Evensen. Structural uncertainty modelling and updating by production data integration. In *SPE/EAGE*

Reservoir Characterization & Simulation Conference, pages cp–170. European Association of Geoscientists & Engineers, 2009.

[84] Gregory P. Smith, David M. Golden, Michael Frenklach, Nigel W. Moriarty, Boris Eiteneer, Mikhail Goldenberg, C. Thomas Bowman, Ronald K. Hanson, Soonho Song, Jr. William C. Gardiner, Vitali V. Lissianski, and Zhiwei Qin. `http://www.me.berkeley.edu/gri_mech/`.

[85] Alessio Spantini, Tiangang Cui, Karen Willcox, Luis Tenorio, and Youssef Marzouk. Goal-oriented optimal approximations of Bayesian linear inverse problems. *SIAM Journal on Scientific Computing*, 39(5):S167–S196, 2017.

[86] Alessio Spantini, Antti Solonen, Tiangang Cui, James Martin, Luis Tenorio, and Youssef Marzouk. Optimal low-rank approximations of Bayesian linear inverse problems. *SIAM Journal on Scientific Computing*, 37(6):A2451–A2487, 2015.

[87] Xavier Tunc, Isabelle Faille, Thierry Gallouët, Marie Christine Cacas, and Pascal Havé. A model for conductive faults with non-matching grids. *Computational Geosciences*, 16(2):277–296, 2012.

[88] Roman Vershynin. *High-dimensional probability: An introduction with applications in data science*. Cambridge University Press, 2018.

[89] Umberto Villa, Noemi Petra, and Omar Ghattas. hIPPYlib: An extensible software framework for large-scale inverse problems. *Journal of Open Source Software*, 3(30):940, 2018.

[90] Umberto Villa, Noemi Petra, and Omar Ghattas. hIPPYlib: An Extensible Software Framework for Large-Scale Inverse Problems Governed by PDEs; Part I: Deterministic Inversion and Linearized Bayesian Inference. *arXiv e-prints*, 2019.

[91] Siddhant Wahal and George Biros. BIMC: The Bayesian Inverse Monte Carlo method for goal-oriented uncertainty quantification. Part I. *arXiv preprint arXiv:1911.00619*, 2019.

[92] Siddhant Wahal and George Biros. BIMC: The Bayesian Inverse Monte Carlo method for goal-oriented uncertainty quantification. Part II. *arXiv preprint arXiv:1911.01268*, 2019.

[93] JE Warren, P J Root, et al. The behavior of naturally fractured reservoirs. *Society of Petroleum Engineers Journal*, 3(03):245–255, 1963.

[94] Forman A. Williams. Detailed and reduced chemistry for hydrogen autoignition. *Journal of Loss prevention in the Process Industries*, 21(2):131–135, 2008.

[95] Roderick Wong. *Asymptotic approximations of integrals*, volume 34. SIAM, 2001.

[96] Olivier Zahm, Tiangang Cui, Kody Law, Alessio Spantini, and Youssef Marzouk. Certified dimension reduction in nonlinear bayesian inverse problems. *arXiv preprint arXiv:1807.03712*, 2018.

[97] Chen Zhangxin and Zhang Youqian. Well flow models for various numerical methods. *International Journal of Numerical Analysis & Modeling*, 6(3):375 – 388, 2009.

[98] James V. Zidek and Constance van Eeden. *Uncertainty, entropy, variance and the effect of partial information*, volume Volume 42 of *Lecture Notes–Monograph Series*, pages 155–167. Institute of Mathematical Statistics, Beachwood, OH, 2003.